# PLANAR SYSTEMS FOR APPLICATIONS IN CATALYSIS AND PHOTOCATALYSIS
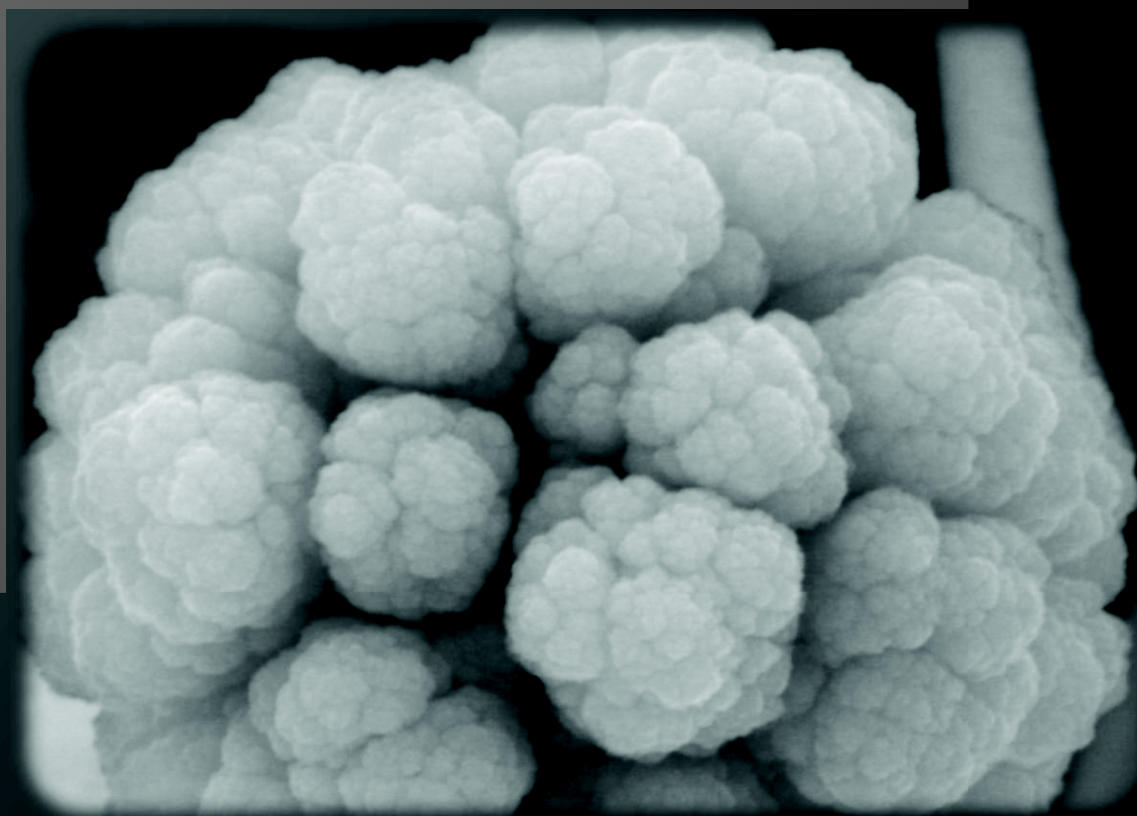
## ANNA NEMÉNYI

### PhD thesis

# UNIVERSITÀ DEGLI STUDI DELL'INSUBRIA

Dipartimento di Scienza ed Alta Tecnologia

Corso di Dottorato in Scienze Chimiche – XXVII Ciclo

*Department of Science and High Technology*

*PhD Course in Chemical Sciences - XXVII Cycle*

# PLANAR SYSTEMS FOR APPLICATIONS IN CATALYSIS AND PHOTOCATALYSIS

Supervisor: **Prof. SANDRO RECCHIA**

PhD Thesis of:

**ANNA NEMENYI**

# Acknowledgements

First of all, I want to thank my advisor Prof. Sandro Recchia for his supervision and kind help during the different stages of my PhD work. I would like to thank also Dr. Marcello Marelli for his helpful suggestions during my research.

Thanks to Dr. Valentina Colombo and Dr. Angelo Maspero for helping me in MOF synthesis. Many thanks also to Prof. Norberto Masciocchi, Dr. Antonella Guagliardi for their availability and fruitful discussion on XRD technique, and Dr. Federica Bertolotti for XRD measurements and data analysis.

I would like also to thank to Dr. Francesco Malara and Dr. Beniamino Iandolo from University of Milan and from Chalmers University of Goteborg for photocurrent measurements on $WO_3$ samples.

I would like to thank the whole research group, past and present, for all of their support and pleasant and just enough fun time spent together: Dr. Damiano Monticelli, Salvatore Caprara, Prof. Andrea Pozzi, Dr. Gabriele Carugati, Rossella Perna, Dr. Cristina Corti, Dr. Barbara Giussani, Dr. Sara Durini.

Last but not least, my deepest thank goes to my own family, my husband and two daughters-angels, Nora and Chiara, who inspired me to push forward in this challenging experience and showed an incredible and out of normal patience during the last phase of the manuscript preparation.

# Contents

## Chapter 1 Metal organic frameworks: synthesis and evaluation of their potential application as heterogeneous catalysts

## Chapter 2 Applications of a true scanning reactor to planar catalysts with variable surface composition

## Chapter 3 Planar systems for applications in catalysis and photocatalysis

## Chapter 4 Anodic stripping tin titration: a method for the voltammetric determination of platinum at trace levels

# Abstract

The doctoral research period was devoted to the development of new ideas in the field of catalysis involving: i) the investigations of possible application of metal organic framework compounds, as their chemical versatility and tailorability make them the most investigated areas of modern coordination chemistry (Chapter 1); ii) the realization of novel apparatus for chemical vapor deposition of semiconducting tungsten oxide films in light of its recent interest for photoelectrochemical water splitting (Chapter 3).

Chapter 1. The Inorganic Section of the Department has been conducting basic research to find new strategies for designing and synthesizing novel metal organic framework materials (MOF). A series of pyrazolate-based MOF compounds were synthesized that may bring promising properties for specific applications. The overall aim of the research presented in this thesis was to investigate their possible applications in heterogeneous gas phase catalysis. As a catalytic test reaction, the catalytic epoxidation of propene was studied. Experiments were performed on a specifically manufactured prototype reactor coupled with mass spectrometric detection. The purpose of this work was also to explore the internal surface sites in the copper-based MOF. To this aim, coordination site accessibility was tested by DRIFT (Diffuse Reflectance Infrared Fourier Transformed Spectroscopy) measurements with CO as probe molecule.

Findings showed that the selected Cu-based MOF ($Cu_3(BTP)_2$) is not suitable for heterogeneous catalysis applications, at least above 220 °C in air. Indeed, XRPD and TGA measurements clearly showed that the copper based metal organic framework does not exhibit sufficient thermal stability in oxidative atmosphere. Moreover, independently from the adopted temperature, DRIFTS measurements proved that $Cu_3(BTP)_2$ does not even possess readily accessible coordination sites, given the scarce adsorption of CO molecules.

Chapter 3. This thesis concerns experimental studies of nanocrystalline tungsten trioxide thin films. Firstly, a new CVD reactor device was developed - transforming a Scanning Planar Catalytic Reactor instrument - for high resolution and steering CVD deposition of tungsten oxide on different substrates. The features of this instrument were tested by

performing $WO_3$ film depositions. Secondly, structural, optical and morphological properties of composite films were characterized using XRD, UV-Vis and SEM/EDX techniques. Texture analysis based on spherical harmonics had aimed at understanding the behavior of CVD process and how the substrates affect orientation of crystalline $WO_3$ films.

Finally, photoelectrochemical properties of $WO_3$ films on appropriate supports were explored in order to contribute to the recent intense research of visible-light effective photoelectrodes for water splitting using new composite materials. It was observed that only crystalline $WO_3$ films have a positive effect in terms of photocurrent. Considering that high temperature treatments are necessary to transform amorphous to crystalline $WO_3$, the utilization of ITO as the substrate is completely ruled out. The results obtained for $WO_3$/hematite systems clearly show that tungsten oxide has a positive effect on the photocurrent properties of hematite. This evidence may be tentatively ascribed to the decrease of surface recombination processes on hematite, due to the presence of the $WO_3$ coverage.

This thesis consists also of two research articles, which are referred to in Chapter 2 and 4.

Chapter 2. The presented paper is submitted to Applied Catalysis A journal. It describes a true scanning reactor for continuous screening of catalytic activities of planar catalysts, from which the CVD apparatus (Chapter 3) concept grew out.

Chapter 4. The presented published paper is not relevant to this PhD research; it is reported because of the author's contribution in catalyst preparation, voltammetric measurements and in writing of the manuscript during the doctoral research period.

# List of abbreviations

| | |
|---|---|
| ALD | Atomic layer deposition |
| APCVD | Atmosphere-pressure CVD |
| BET | Brunauer–Emmett–Teller |
| CB | Conduction band |
| CE | Counter electrode |
| CSD | Cambridge structural database |
| CUS | Coordinatively unsaturated sites |
| CVD | Chemical vapour deposition |
| DMF | Dimethylformamide |
| DMSO | Dimethyl sulfoxide |
| DRIFT | Diffuse reflectance infrared Fourier transformed spectroscopy |
| EDX / EDS | Energy dispersive X-ray spectroscopy |
| FTO | Fluorine doped tin-oxide |
| ITO | Tin doped indium oxide |
| LPCVD | Low-pressure CVD |
| MOCVD | Metal-organic CVD |
| MOF | Metal organic framework |
| NHE | Normal hydrogen electrode |
| PECVD | Plasma-enhanced CVD |
| PMMA | Poly(methyl methacrylate) |
| POM | Polyoxometalates |
| PSM | Postsynthetic modification |
| PVD | Physical vapor deposition |
| QMS | Quadrupole mass spectrometer |
| RE | Reference electrode |
| RHE | Reversible hydrogen electrode |
| SBU | Secondary building unit |
| SCE | Saturated calomel reference electrode |
| SEM | Scanning electron microscopy |
| STA | Simultaneous thermal analysis |
| TG/DSC | Thermogravimetry/Differential scanning calorimetry |
| TGA | Thermogravimetric analysis |
| TLC | Thin-layer chromatography |
| TXRPD | Variable-temperature X-ray powder diffraction |
| UV | Ultraviolet |
| VB | Valence band |
| Vis | Visible |
| WE | Working electrode |
| XRD | X-ray diffraction |
| XRPD | X-ray powder diffraction |

# List of Figures

Chapter 1

## Chapter 3

# List of Tables

## Chapter 1

## Chapter 3

# List of Publications

Anna Nemenyi participated in paper 1 in catalyst preparation, voltammetric measurements and in writing of the manuscript. In paper 2 she contributed in figures preparation and manuscript writing. She was the main author in paper 3 (in preparation). The articles are reprinted with kind permission of the publishers.

1. B. Giussani, S. Roncoroni, **A. Nemenyi**, V. Dal Santo, D. Monticelli, S. Recchia. Anodic stripping tin titration: A method for the voltammetric determination of platinum at trace levels. Analytical Chemistry 86 (13), 6654-6659 (2014)

2. M. Marelli, **A. Nemenyi**, V. Dal Santo, R. Psaro, L.Ostinelli, D.Monticelli, C. Dossi, S.Recchia. Applications of a true scanning reactor to planar catalysts with variable surface composition. Applied catalysis A, submitted

3. **A. Nemenyi**, M. Marelli, V. Dal Santo, R. Psaro, D. Monticelli, C. Dossi., S. Recchia. Chemical vapor deposition of $WO_3$ films over planar systems: an alternative scanning approach, in preparation

### Communications

EFCATS Summer School and 1st Italian-Spanish School on Catalysis (11-15 September 2012) Spatially resolved catalytic tests on planar systems: preliminary results on the development of a scanning reactor for planar catalysts. **A. Nemenyi**, M. Marelli, L. Ostinelli, V. Dal Santo, R. Psaro, C. Dossi, S. Recchia (poster)

FIRB – General Meeting 2014, Milano (Italy), 24-25 February 2014. *Oxides at the nanoscale: multifunctionality and applications*. Applications of scanning reactor to planar catalysts studies and preparation (oral presentation)

**Work done in collaboration with others**

All of the work presented in this thesis was carried out by the author apart from the following exceptions:

The ITO/hematite substrates described in Chapter 3 were fabricated at Chalmers University, Göteborg, Sweden. The photocurrent measurements of the composite ITO/hematite/WO$_3$ samples were carried out by Dr. Beniamino Iandolo (Chalmers University).

The FTO/hematite substrates described in Chapter 3 were fabricated at CNR-ISTM of Milan, Italy, by Dr. Marcello Marelli. The photocurrent measurements of the composite FTO/hematite/WO$_3$ samples were carried out by Francesco Malara (CNR-ISTM).

XRD measurements and modeling were performed by Prof. Norberto Masciocchi, Dr. Federica Bertolotti and Dr. Antonella Guagliardi (University of Insubria).

# Chapter 1

## Metal organic frameworks: synthesis and evaluation of their potential application as heterogeneous catalysts

# 1. Metal Organic Frameworks

## 1.1 Introduction

Metal organic frameworks (MOFs) or, broadly speaking, coordination polymers have been known since 1965 [1], although this field was relaunched only at the end of the last century thanks to the pioneering works by Robson and co-workers, [2] Kitagawa et al. [3], Lee and Moore, [4] Férey et al. [5] and Yaghi and co-workers [6]. In particular, the latter authors used the term metal-organic framework for the first time, replacing the other terminologies as coordination networks, inorganic-organic coordination polymers, porous coordination polymers and many other similar denominations for porous crystalline compounds. MOFs can be defined as hybrid materials that are assembled by the connection of metal ions or clusters (inorganic secondary building unit, SBU) through organic bridging ligands by coordination bonds of moderate strength. Although they have been considered just for curiosity at first, in a short time MOFs became one of the most investigated areas of modern coordination chemistry. In the early stage researches were mostly focused on the discovery of new structures (see Figure 1.1). The number of possibilities of combining inorganic (metal ions or clusters) and seemingly limitless organic moieties is immense; in fact, more than 20,000 different MOFs have been reported and studied during the past decade [7].

Within such a relatively short time span, the field has rapidly evolved to a more mature phase in which several applications are being explored and the number of published papers concerning MOF synthesis, characterization and application is exponentially growing.
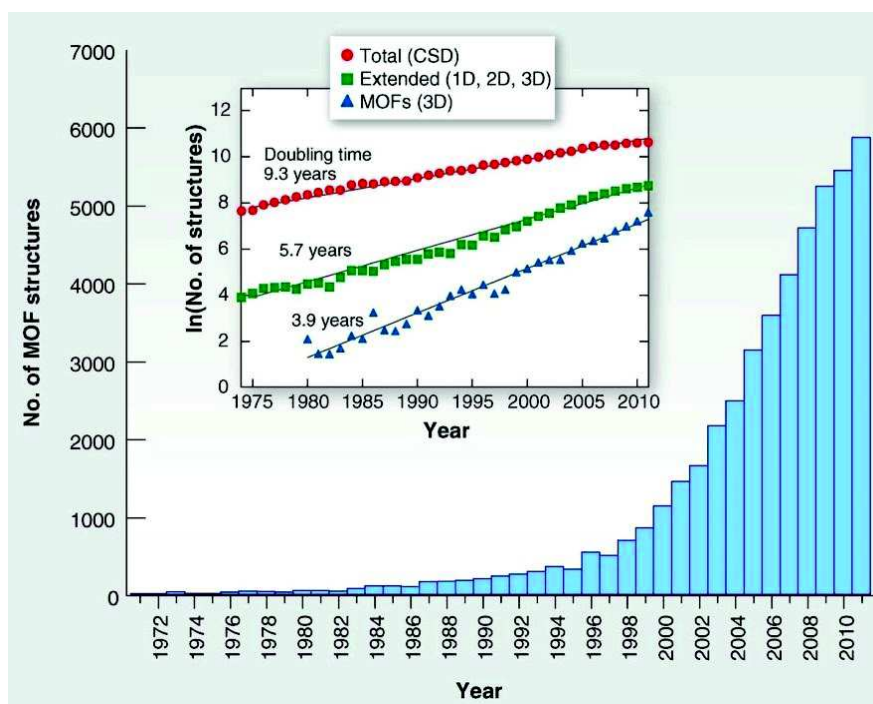
**Figure 1.1.** Metal-organic framework structures (1D, 2D, and 3D) reported in the Cambridge Structural Database (CSD) from 1971 to 2011 [7].

The reason for their success in the scientific community (solid state chemistry, physics, life sciences, etc.) is related to several unique and outstanding features of these materials: the self assembly of these components, typically in solution, creates 3D crystalline structure with rigid pores readily accessible and an impressive surface area. It is easy to imagine that the cavity size and shape can be tuned (and in some cases also predicted) by changing the dimension (expansion or shrinkage) of the organic linker such as amines, pyridines, carboxylates, sulfates, phosphates, etc.

Pioneering work on this topic was made by Yaghi and co-workers who made a large body of work on MOF-5 $[Zn_4O(tpa)_3]_n$ (tpa = terephthalic acid) (Figure 1.2) which became the framework that more than other ones helped the development of design and tunability of the pore size. This MOF is a 3D cubic-shaped framework in which the SBU units are tetrahedral $Zn_4O$ clusters, which bind six organic (benzenedicarboxylic acid) building blocks in an octahedral array.
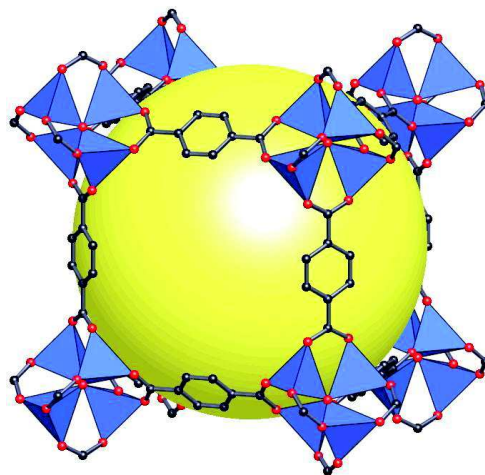
**Figure 1.2.** Single crystal x-ray structure of MOF-5 (Zn, blue polyhedral; O, red spheres; C, black spheres. The yellow sphere represent the largest sphere that can occupy the pore without touching the framework. H atoms are omitted for clarity).

Only three years later of the discovery of this material, in 2002, Yagi et al. [8] reported 16 new MOFs using the same metal cluster as inorganic fragment and systematically elongated bridging linkers (Figure 1.3). He demonstrated that the size and nature of the structure were varied without changing its underlying topology. The so called isoreticular MOFs have pore sizes from 3.8 to 29 Å.

Beside this outstanding research there are only few other examples [9,10] of isoreticular libraries: it is a great challenge to predict the structure of a new polymer as the synthesis conditions (temperature, pH, solvent, etc.) – as well as the building units - can influence the crystalline structure of the final product.
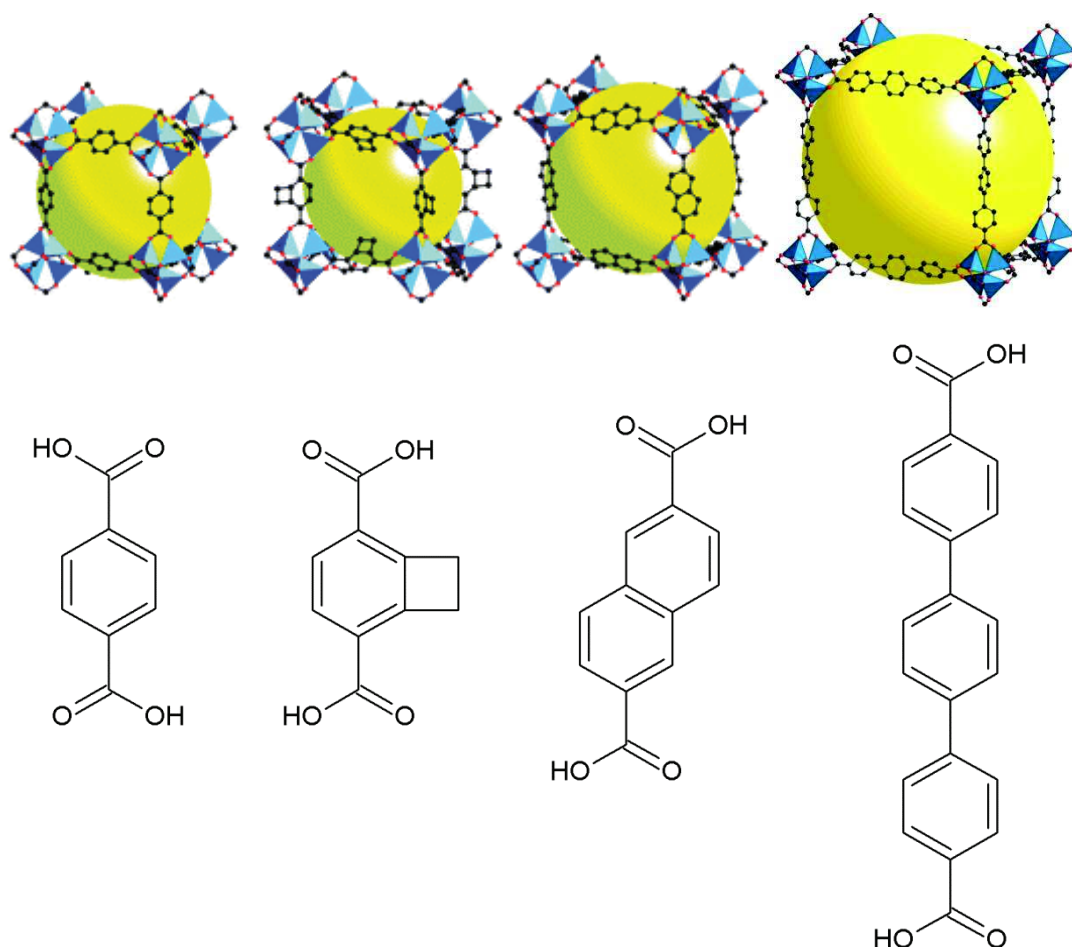
**Figure 1.3.** Demonstration of isoreticular chemistry: single crystal structures of some of the IRMOF series and the corresponding ligands. (IRMOF-n, n=1, 6, 8, 16; Zn, blue polyhedral; O, red spheres; C, black spheres. The yellow sphere represent the largest sphere that can occupy the pore without touching the framework. H atoms are omitted for clarity.)

In addition to the tunability of the pore size, the other key advantage of MOFs is the possibility to modify the structure and consequently the proprieties of the framework introducing specific substituents on the carbon chain. Indeed, MOFs should be more flexible when compared to other inorganic solids because they possess an organic component suitable for a wide range of chemical transformations. However, the preparation of highly functionalized MOFs has been largely limited by the commonly used solvothermal synthetic methods, as functional groups may be thermally labile, can coordinate the metal ions or exhibit low solubility. In any of these cases, the synthesis of

the MOFs will be complicated or completely failed. Fortunately, alternative methods are available for introducing functional groups into MOFs. Post-synthetic chemical modifications [11] can be performed on the fabricated materials eliminating the need to develop new conditions for MOF synthesis. Whereas MOFs are highly porous, the ability of reagents to access the interior of the solids suggests that functionalization can be achieved on both the interior and exterior of the material.

As mentioned above, the porosity and high internal surface area are the foremost attributes of MOFs that set them apart from other traditional porous materials. In order to understand their enormous potentiality it is worthwhile to compare with other, important classes of porous materials. Actually inorganic porous materials, namely aluminosilicate zeolites and mesoporous silica have already found broad application in various fields (petrochemistry, detergent industry, etc) therefore emphasizing similarities and differences between their properties can help us to appreciate the importance of MOF materials. Based on the porosity we can distinguish three categories of materials. Amorphous silica and aerogels which have pores larger than 50 nm are called macroporous solids, whereas mesoporous materials such as amorphous mesoporous silica have uniform and ordered pores between 2 and 50 nm. Zeolites are defined as microporous crystalline aluminosilicates with a three-dimensional framework structure containing pores of molecular dimensions (0.3–2 nm). In this context MOFs appear as a bridge between zeolite and mesoporous silica having crystalline structure and large pores at the nanometer scale. The important advantage of MOFs compared to the other classes of structures is their chemical versatility: while zeolites are similar open networks with microporous pores, they lack synthetic flexibility and structural tailorability. In fact the total number of zeolites is less than 300 [12], and the highest surface area to date is about 900 $m^2/g$, [10] whereas thousands of MOF structures were discovered during the last fifteen years with ever-growing surface area: the highest experimental Brunauer−Emmett−Teller (BET) surface area is related to NU-110E [13] with a value of 7140 $m^2/g$. Another remarkable example is MOF-399 which has the highest porosity (94%) and lowest density (0.126 $g/cm^3$) of any MOF reported to date [14].

The initial interest in searching outperforming MOF systems has been overcame by the necessity of finding materials useful for practical applications and it involves many disciplines, such as organic and inorganic chemistry, physics, environmental sciences, medicine, biology and industry as well. Although this research field is in its infancy, the related bibliography is vast and still enormously growing. MOFs can provide many solutions in gas adsorption and storage, gas- and liquid-phase membrane separations [15], drug delivery [16] and catalysis [17]. Magnetic [18], proton-conducting [19] and semiconductor [20] frameworks has also attracted the interest of research workers for advanced applications. Recent studies were conducted on MOF-based (opto)electronic devices [21] (LED materials, nonlinear optical devices), as well as on possible biological and medical applications [22]. A general overview on this topics may only be given, mentioning the most important issues and paying special attention to catalytic applications that is the goal of this first part of the thesis work.

## 1.2 Overview on applications

### 1.2.1 Gas adsorption / storage / separation

The decrease in fossil fuel reserves incites the scientific community to find an adequate energetic source and MOFs might be crucial in this regard for their capacity to adsorb large amounts of strategic gases such as $H_2$, $CH_4$, CO, $O_2$, $NO_x$, $C_2H_2$. In addition, there is a considerable worldwide interest to reduce greenhouse gas emissions like carbon dioxide, which is often assigned as being responsible for global warming.

The first success in this field is attributed to Kitagawa (1997) [23], and his proof-of-concept soon expanded into several other studies on gas storing MOF materials, characterized by high specific surface areas and large pore sizes. Special attention is given to increasing the storage capacity of fuel gases such as hydrogen and carbon monoxide. Even though the first study of hydrogen adsorption was reported for MOF-5 in 2003 [24], there are hydrogen adsorption data for hundreds of hybrid porous polymers [25]. MOFs also offer reversible carbon dioxide adsorption and are promising materials for the selective capture of carbon from the atmosphere and flue gas. In 2005, a detailed study of carbon dioxide adsorption in a series of MOFs at room temperature evidenced the potential of this

materials for possible industrial applications: MOF-177 proved to have outstanding uptake capacity of carbon dioxide that overcomes any known porous material under similar experimental conditions [26]. At present, the only use in the industry arises from a study of Yaghi and coworkers: the study of high-pressure methane adsorption in an extended metal-organic structure demonstrated an excellent uptake capacity and this technology is currently being trialed for natural gas storage in heavy duty vehicles by BASF [27].

Given that one of the most common uses of porous materials is in separation of mixtures of gases or liquids, it was expected that MOFs might play an important role also in separation of hydrocarbons, toxic molecules from water, $CO_2$ from $CH_4$ in natural gas, including purification of $O_2$ and $N_2$, just like removal of volatile organic compounds from gas mixtures [28]. Gas separation is closely related to adsorption; however it requires the selective adsorption of specific guest molecules from a mixture of compounds either in the liquid or gas phase and it is based on size, shape or chemical affinity of MOFs towards the mixture. Among the numerous studies, it is worth to mention the most important achievements. Weireld and coworkers investigated the removal of benzothiophene derivatives from isooctane solutions, reaching adsorption performances compatible to zeolite Na(Y) [29, 30]. A more extended study was performed by Yaghi and coworkers on the adsorption of various harmful gases, such as sulfur dioxide, ammonia, chlorine, tetrahydrothiophene, benzene, dichloromethane, and ethylene oxide [31]. The adsorption capacity of the examined MOFs were similar to that achieved with activated carbon (BLP carbon). A remarkable example of size selectivity is the work of J. Li et al. [32] who focused his research on separation of alkanes, which is a very important industrial process based on zeolite adsorbents. He proved that a well-chosen MOF pore size can separate normal C2, C3, and n-C4 olefins and alkanes from branched alkanes and normal hydrocarbons above C4.

## 1.2.2 Drug delivery

A very new but attractive field [33] for MOFs application was introduced by Horcajada et al. in 2006. They investigated the loading uptake and releasing time of ibuprofen (a nonsteroidal anti-inflammatory drug) employing some mesoporous MOFs with pore aperture up to 16 Å. A large portion of the recent researches is focused on the same

members of the MOF family (MIL compounds), because of its large pore aperture that is necessary for enclosing molecules such as cisplatin (cis-diamminedichloroplatinum(II), chemotherapy drug), AZT-TP (anti-HIV drug) and busulfan (anticancer drug) [34]. For this latter it was possible to achieve a loading 5-fold higher than currently available for drug delivery. These results underline the promise of MOFs in the field of drug delivery and indicate that MOFs are ready for biological testing.

### 1.2.3 Overview on catalysis

Heterogeneous catalysis was one of the earliest proposed [35] and also demonstrated [36] applications for porous crystalline MOF materials. Despite this, the scientific research was rather limited for a long and only recently wide-ranging experimental exploration has been undertaken. On the basis of an up to date research, [37] the situation has improved dramatically since 2009 (Figure 1.4).

In order to comprehend this trend, to understand the enormous potentiality but also weakness of MOFs as heterogeneous catalysts, it is suitable to emphasize its chemical versatility which is due to the nature of their hybrid (organic and inorganic) chemical composition and high and regular porosity. MOFs contain three well-differentiated parts where the active catalytic site can be allocated: the inorganic unit, the organic linker and the pore space.
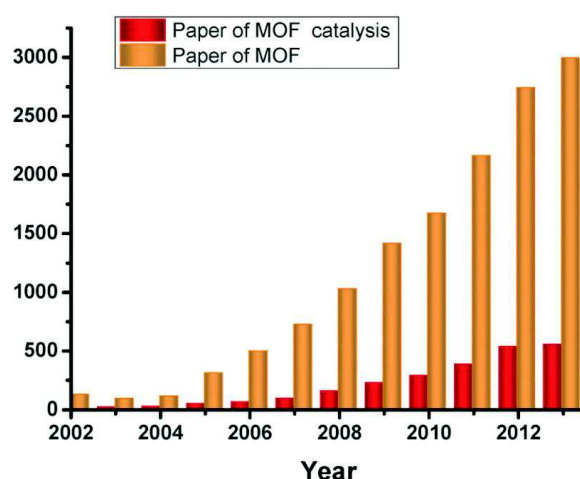


**Figure 1.4.** Development of MOF fields in comparison to the MOF catalysis in the last ten years (SciFinder until Jan 15, 2014).

Consequently there are different strategies for MOF-based catalysis. Firstly, *framework activity* may be used when the as-synthesized compound exhibit catalytic activity due to metallic component or due to the original organic building blocks. Secondly, as mentioned before, there is also the possibility to introduce additional functional groups into MOFs by *post-synthetic chemical modification (PSM)*. Finally, MOFs can act as templates for active molecules or nanoparticles (*encapsulation*) thanks to their rigid structure with high porosity. All these strategies are summarized in Figure 1.5 indicating also the subcategories of the possible modifications that will be described in the next paragraphs.
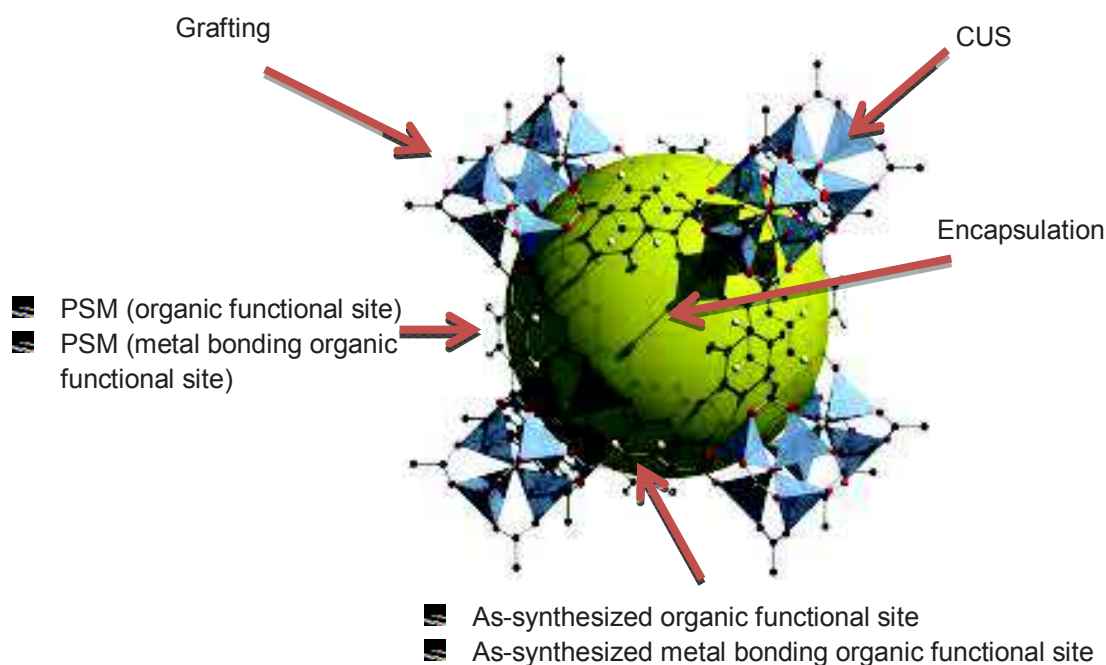


**Figure 1.5.** Different strategies for the inclusion of catalytic sites into a MOF structure.

*As-synthesized framework activity- on metal center*

A catalytic reaction can take place on the metal center of MOFs when the substrate can bind directly to the active site. To satisfy this condition it is necessary that the crystalline structure preserves its integrity after the expansion of the metal ion coordination sphere or the displacement of organic linkers. Highly flexible copper based coordination polymers were found by Tabares [38] [Cu(im)$_2$] (im = imidazolate) and recently by F. X. Corma and co workers [39] [Cu(2-pymo)$_2$] (2-pymo = 2-hydroxypyrimidinolate): these MOFs are able

to catalyze important reactions such as oxidation of activated alkanes. More frequently weakly bonded water or solvent molecules can complete the coordination of metal ion that can be removed by heating. The so-called coordinatively unsaturated metal sites (CUS) can strongly interact with organic molecules in catalysis without modifying the structural characteristics. This field is the most widely explored in MOF catalysis, involving a broad range of metal ions ($Cr^{3+}$, $Fe^{3+}$, $Al^{3+}$, $Sc^{3+}$, $V^{4+}$, $Mn^{2+}$, $Co^{2+}$, $Cu^{2+/1+}$, $Zn^{2+}$, $Ag^+$, $Mg^{2+}$, $Zr^{4+}$, $Pd^{2+}$, $Ce^{4+}$ and $Bi^{3+}$) for different types of organic reactions. Just mentioning the most common ones, alcohol and hydrocarbon oxidation, cyanosilylation of aldehydes as well as aldol condensation reactions were examined [37].

*As-synthesized framework activity- on organic ligand*

The vast assortment of organic species available for MOF synthesis could suggest an infinite variety of applications, however, only a few prototypic examples have been reported on guest-accessible catalytic organic functional groups. It can be explained with the self-assembly of the framework: the metal ion tends to coordinate the available free reactive functional sites blocking them on the rigid network. Crucial works of Kim [40], Kitagawa [41], and Gascon [42] must be mentioned on pyridyl, amide and amino functionalized as-synthesized MOFs. The basic properties of this materials were exploited for catalyzing transesterification or Knoevenagel condensation reactions. A special class of MOF materials are those that have pseudo-organic ligands such as metallosalens [43, 44] and metalloporphyrins [45,46]. In this case the catalytic active metal center is trapped on the crystalline framework and do not contribute to the network skeleton. This strategy offers interesting advantages because the large and rigid linkers ensure considerable channels (about 10-25 Å) and metal ion is easily accessible through the pores and can coordinate the substrate without straining the crystalline framework. An important advantage of this type of catalysis is that asymmetric or enantioselective reactions can be performed exploiting the chirality of the linkers. While the porphyrinic MOF catalytic chemistry is rather limited, the chiral Mn, Ru, Co and Ni, metallosalen based compounds are extensively studied for asymmetric epoxidation, cyclopropanation and hydrolytic kinetic resolution resulting in excellent selectivity.

*Post-synthetic chemical modification*

One of the key benefit of MOFs is the possibility to incorporate a wide range of functional groups in channel surfaces of the fabricated material providing complex functionalities. The limitation for post synthetic functionalization is only the fantasy of the researchers. The functional groups most frequently used are pyridyl, amide, amino, aldehyde and sulfoxy groups as well as pyrrolidine, bipyridyl, urea, catechol, N-heterocyclic carbine and binol groups [37]. This strategy can be firstly used to decorate the carbon chain ligands of coordination polymers with organocatalytic groups (providing hydrogen-bonding, acidic, or basic sites) that can directly promote, for example, aza-Michael reaction between aliphatic amines and alkenes or transesterifications. The second opportunity is to introduce new metal binding sites exploiting the anchoring properties of the post-synthetic organic functional groups. This kind of design has been demonstrated efficient for grafting to walls of the framework ions $Pd^{2+}$ [47], $Ti^{4+}$ [48], $Au^{3+}$ [49], $Cu^{2+}$ [50], $Fe^{3+}$ [50], $In^{3+}$ [51] ions providing additional reactivity.

Coordinatively unsaturated metal sites can also act as anchoring points for grafting of additional functionalities. After the removal of guest molecules, active organic groups can be tethered to the metal node. When ethylenediamine was grafted in the chromium center of MIL-101, the catalytic activity was confirmed by testing Knoevenagel condensation as a base-catalyzed model reaction [52]. Two sequential post-synthesis modifications were performed by Hupp et al. on the same MOF material. Catechol was firstly grafted to MIL-101 (Cr) through the unsaturated chromium (III) centers and in the second step $V^{5+}$ was immobilized to the chelating functional group. This vanadyl(monocathecolate)-decorated metal organic framework is proved to be active in the catalytic oxidation thioanisole [53].

*Encapsulation*

As mentioned before, the rigid, zeolite-like crystalline framework is suitable to host catalytically active moieties, such as metal complexes (polyoxometalates, metallo-porphyrins) clusters and nanoparticles without establishing chemical bonds. In this case the MOF serves only as physical space for the catalysis, the organic and inorganic building units not taking part of the catalytic reaction. Generally, metal nanoparticles are excellent catalysts for numerous reactions: it is not surprising that Cu, Ru, Pt, Au and Pd

[37] nanoparticle deposition in MOFs has been extensively studied. The cavities have the function to control the size of nanoparticles or to provide shape and size selectivity. A remarkable example is the catalytic hydrogenation of styrene, 1-octene, and cis–cyclooctene by Pd-loaded MOF-5 [54]. This reaction shows size selectivity because proceeds with higher conversion for styrene than for cis–cyclooctene which has larger kinetic diameter. MOFs with very large cavities can encapsulate also porphirins and polyoxometalates (POM). Aside from being a curiosity, catalytic experiments showed that the composite materials can display better performance and higher selectivity to the homogeneous POM catalysts [55].

This introduction aimed to highlight the chemical versatilities of the MOF-compounds and their possible application in different fields and it was probably for such properties that Catherine Pinel et al. (2009) stated in their review: "MOF materials are dream compounds for catalysis". In contrast to this emphasis, why MOFs did not find industrial applications on a larger production scale yet? What are the reasons justifying such scarce industrial use? What missed characteristics should be taken into account? These questions will be answered in the next section.


## 1.3 Drawbacks of MOFs
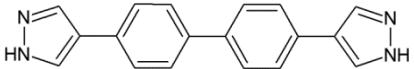
Most of the metal organic framework structures discovered up to date have three fundamental drawbacks that have impeded their wider utilization until now: the inconvenience of low stability against humidity, low resistance to harsh chemical environment and, above all, low thermal stability. In many cases, their crystalline structure are sensitive just by exposure to air and may become amorphous [56], and this is a critical drawback for practical applications. Furthermore, thermal treatment often compromises the properties of MOF materials; as a matter of fact, activation of this materials is often based on the removal of solvent and guest molecules from the pores but it may lead to irreversible collapse of the structure. Moreover, the complete decomposition of the framework is usually occurs below 300 °C and this is the reason why MOFs will probably never compete with zeolite materials which are thermally stable up to 500-800 °C. And last, we need to consider also the material preparation costs; starting materials for MOF

synthesis are often expensive or commercially not available and therefore there is the necessity to perform multi step synthesis.

## 1.4 Current research in the Inorganic group

It is evident that the search for new porous metal–organic frameworks that are stable in air, water, acidic and basic media, and even under extreme temperatures and pressures, is a key point in MOF research to extend their utility toward a variety of applications where other porous materials, such as zeolites, have been playing a major role.

The Inorganic Section of the Department has been conducting basic research to find new strategies to design and synthesize functional materials that could show different of even better chemical and thermal properties than the already existing ones [57]. Their investigation is based on the fact that carboxylate-based metal-organic frameworks – due to the strength of the O-M bond- may undergo hydrolysis and thermal decomposition while frameworks with N-donor organic linker usually exhibit higher stabilities. A series of linear and triangular pyrazolate-based ligands were synthesized with the aim of generating Co-, Ni-, Cu- and Zn-based MOF materials (Table 1.1). Accordingly, structural characterization by X-ray powder diffraction, and thermal behavior investigation by simultaneous TG/DSC analysis and thermodiffractometric studies were performed. The gas adsorption measurement on these novel coordination polymers revealed that they do not only enrich the MOF database, but also may bring promising properties for specific applications.

| Ligand abbreviation | Ligand structure | MOF |
|---|---|---|
| $H_2BDP$ |  | NiBDP<br>$Cu_2BDP$<br>ZnBDP |
| $H_2PBP$ |  | NiPBP |

| | | |
|---|---|---|
| H₂TET |  | NiTET |
| H₂BDP_NO₂ |  | NiBDP_NO₂ <br> ZnBDP_NO₂ |
| H₂BDP_NH₂ |  | NiBDP_NH₂ <br> ZnBDP_NH₂ |
| H₂BDP_OH |  | NiBDP_OH <br> ZnBDP_OH |
| H₂BDP_SO₃H |  | NiHBDP_SO₃ |
| H₃BTP |  | Ni₃(BTP)₂ <br> Cu₃(BTP)₂ <br> Zn₃(BTP)₂ <br> Co₃(BTP)₂ |
| H₂CPZ |  | NH₄[Cu₃(μ₃-OH)(μ₃-4-carboxypyrazolato)₃] |
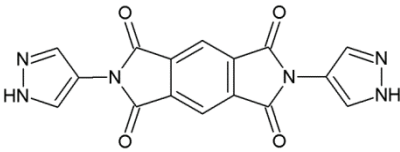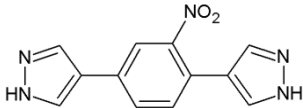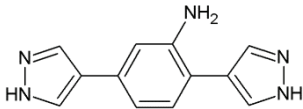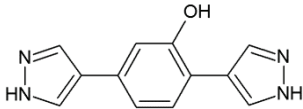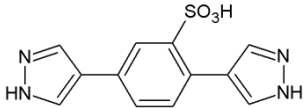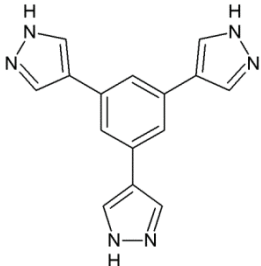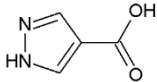
**Table 1.1.** Polytopic pyrazole-based ligand abbreviations, structures and corresponding metal organic frameworks synthesized in the PhD research of Dr. Colombo Valentina [57].

## 1.5 Outline of this research

The overall aim of the research presented in this thesis is to extend the aforementioned studies on novel, pyrazolate-based metal-organic frameworks. Given the encouraging results on the thermal stability of highly porous, 3-D polymers [58], their possible applications were hypothesized in heterogeneous gas phase catalysis. To reach this goal, three out of seventeen MOFs were selected because of their suitable properties for this kind of application. Since neither the crystalline MOF nor the organic building unit were commercially available, it was first necessary to synthesize the selected metal organic frameworks according to synthetic way shown by Dr. V. Colombo. For one of the organic ligands, modification of the procedure was performed because of the different starting material.

As a catalytic test reaction, a simple oxidation reaction, the catalytic epoxidation of propene was chosen. The experiments were performed on a specifically manufactured prototype reactor coupled with mass spectrometric detection.

The purpose of this work was also to explore the internal surface sites in MOFs. To this aim, coordination site accessibility was tested by DRIFT (Diffuse Reflectance Infrared Fourier Transformed Spectroscopy) measurements with CO as probe molecule.

# 2. Synthesis and characterization

## 2.1 Design of catalytic experiments

In every research project, in particular catalysis, planning is crucial. There are two main approaches for designing catalytic experiment involving different steps starting from application to synthesis or vice versa as illustrated in Figure 2.1. Usually the process starts with focusing on a specific reaction of interest, and on the basis of the catalytic reaction mechanism, the main characteristics of the catalyst need to be identified. The next step is to synthesize a set of candidate materials and to prove their performance for the selected chemical reaction (by trial and error approach).

**Catalytic reaction**

**Mechanism**

**Catalyst characteristics**

**Candidates**

**Synthesis**

**Catalytic experiments**

**(Synthesis)**

**Candidates**

**Catalyst characteristics**

**Mechanism**

**Catalytic reactions**

**Catalytic experiments**
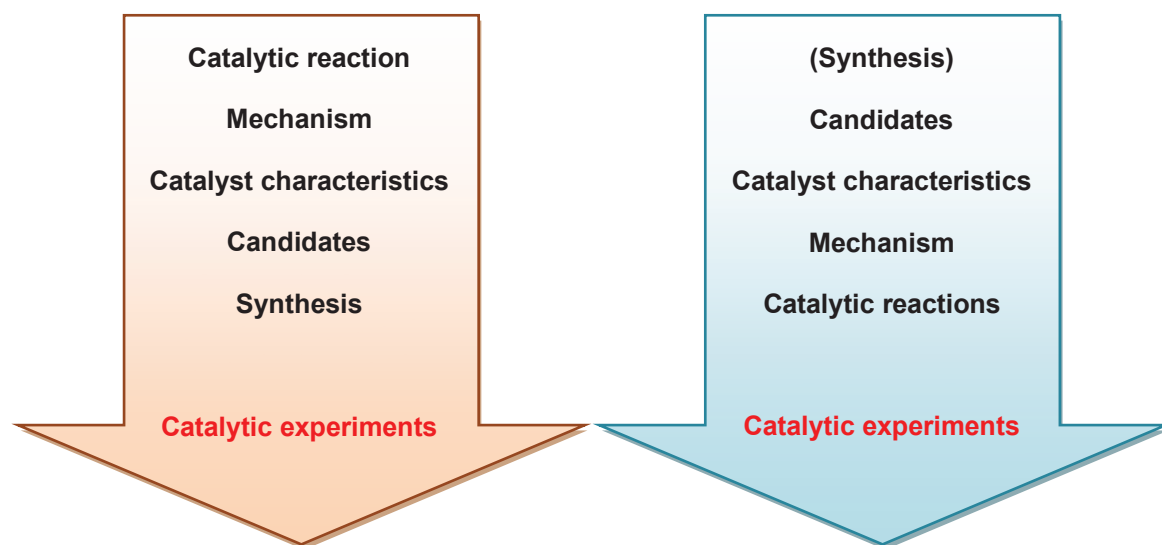
**Figure 2.1.** The two main strategies for designing catalytic experiments.

The second possibility is to move on the opposite way. The first step is to establish the possible candidates for catalytic use. The choice is often related to results of synthetic research on new compounds. On the basis of their physical and chemical properties, it is possible to suppose their role in a catalytic reaction mechanism, and select suitable reactions. Again, catalytic testing is carried out.

For MOF chemistry, the second approach is generally applied since the original aim of researchers was to synthesize and characterize new and interesting structures with the purpose of bringing into focus their major features. It is only at this point that possible catalyst candidates for appropriate reactions are identified. Requirements that need to be fulfilled for a substance to be regarded as a good catalyst are:

1. The framework must have chemical and thermal stability under the catalytic reaction conditions.
2. Pores and channels must be empty (of solvents or guest molecules) and large enough for the reagents and products of the catalytic reaction.
3. The catalytic site must be accessible for reactants.
4. The framework must maintain the crystalline structure and porosity during the catalytic process.

In addition, the catalytic performance is considered satisfactory if catalytic reactions proceed with a high turnover number (TON) and a high turnover frequency (TOF).

Originally, we focused our investigation on the potential catalytic activity of highly porous pyrazolate-based metal-organic frameworks that were the research theme of some PhD programs of our Department in recent years [57]. In order to select suitable MOFs among the numerous newly synthesized structures (Table 1.1), properties such as pore aperture and thermal stability were taken into account. On the basis of the above mentioned criteria, three MOFs appeared to exhibit the appropriate characteristics for heterogeneous catalysis: $Cu_3(BTP)_2$, NiBDP and ZnBDP.

## 2.2 MOFs of our interest

**Cu₃(BTP)₂** (H₃BTP = 1,3,5-tris(1H pyrazol-4-yl) benzene)**:** this compound crystallizes in the cubic space group *Pm 3m*. Each single organic ligand bonds three metals through the three pyrazolate groups leading to a rigid three-dimensional framework where each metal node has a square planar coordination geometry. Figure 2.2 shows the octahedral-shaped cavity that extends along the cell axes, originating channels with diameter of nearly 10 Å. The calculated density of this framework is 1.13 g cm$^{-3}$.
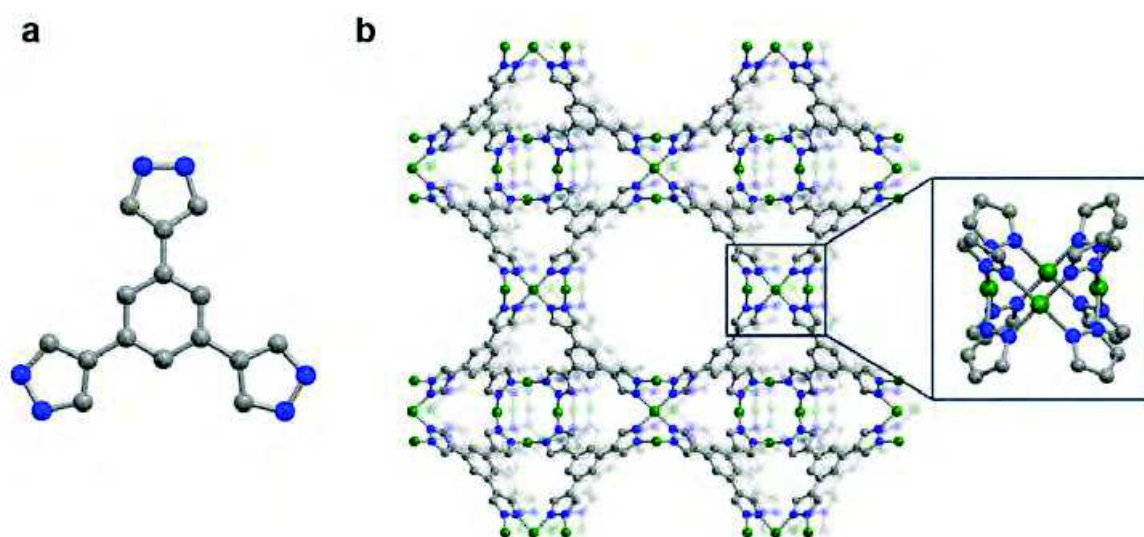


**Figure 2.2.** (a) Schematic drawing of the crystal structure of Cu₃(BTP)₂ (Carbon, grey; nitrogen, blue; copper, green.); (b) square planar stereochemistry at the Cu(II) ions. Hydrogen atoms have been omitted for clarity.

Of particular promise are frameworks with surfaces bearing exposed metal centers, since these can serve as a source of catalytic activity. This copper based compound represents a highly-stable metal-organic framework with accessible metal sites lining the pore surfaces. The exceptional thermal and chemical stability of the examined MOF was highlighted by simultaneous thermal analysis (STA) in N₂ stream, and powder X-ray diffraction analysis at varying temperature (TXRPD) carried out under air.

**NiBDP** (H$_2$BDP = 1,4-bis(1H-pyrazol-4-yl)benzene) is a 3-D network structure crystallized in orthorhombic Imma space group. The metal centers have square-planar geometry, coordinated by four nitrogen atoms of four different BDP ligands. As shown in Figure 2.3, the rhomboid-shaped cavity size is determined by BDP ligands, forming large, nearly 13.2 Å pore diameter and low framework density (0.86 g cm$^{-3}$). Particulary interesting, the estimated bulk density of NiBDP is only 0.86 g cm$^{-3}$. NiBDP possesses a large specific surface areas, the BET surface value is ca. 1600 m$^2$ g$^{-1}$.
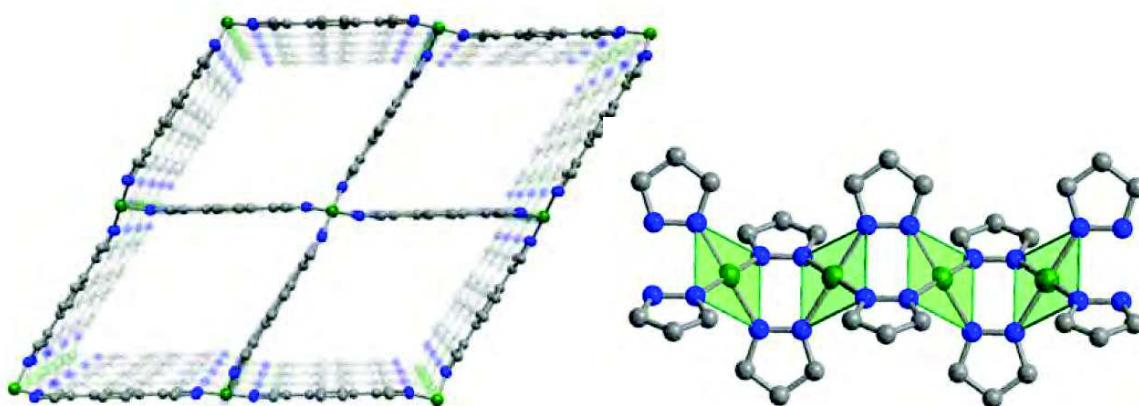


**Figure 2.3.** (Left): Schematic drawing of the crystal structure of NiBDP (Carbon, grey; nitrogen, blue; nickel, green) ; (Right): Square planar stereochemistry at the nickel(II) ions. Hydrogen atoms have been omitted for clarity.

The NiBDP framework exhibit quite high thermal stability; the thermal decomposition takes place at a temperatures of 450-460 °C. Gas adsorption studies (Ar, N$_2$ at 77 K and CH$_4$, CO$_2$ at 273 K) confirmed that this compound has highly accessible pores and therefore it suggests that NiBDP is a possible candidate as a heterogeneous catalyst.

**ZnBDP** (C$_{12}$H$_8$N$_4$Zn, H$_2$BDP = 1,4-bis(1H-pyrazol-4-yl)benzene) crystallizes in the tetragonal space group *P4$_2$ /mmc*. The metal centers are tetrahedrally coordinated (see Figure. 2.4). It can be appreciated in Figure 2.4 that the 3-D network is formed by connecting parallel chains providing square-type pores. Not surprisingly, the cavity size is similar to that of NiBDP (13.2 Å), considering the same organic linker was used. The calculated density is 0.71 g cm$^{-3}$.
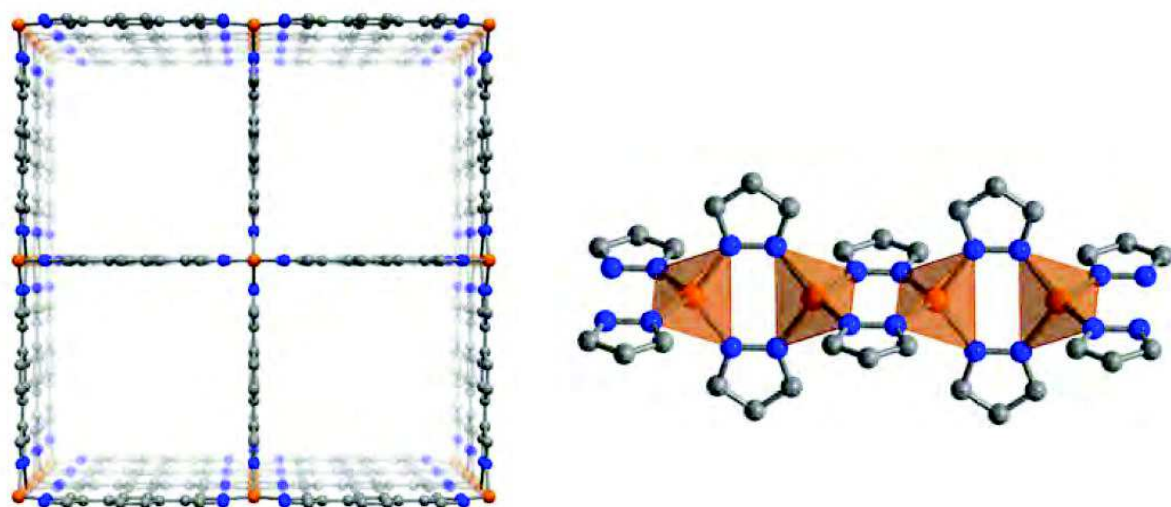
**Figure 2.4.** (Left): Schematic drawing of the crystal structure of ZnBDP (Carbon, grey; nitrogen, blue; zinc, orange.); (right): tetrahedral stereochemistry at the zinc(II) ions. Hydrogen atoms have been omitted for clarity.

With regards to the thermal stability and gas adsorption properties, ZnBDP was investigated under similar conditions as the Ni based polymer: crystallinity is lost starting from around 420 °C and it exhibits a large gas storage capacity (22.5 mmol g$^{-1}$ of $N_2$ and Ar at 77 K) which is indicative of a very high accessibility of its microporous structure.

## 2.3 Experimental

Polytopic pyrazolate ligands are not commercially available and must be synthesized from available starting materials. All chemicals were obtained commercially and used without further purification.

Critical importance during a multi step synthesis is to control the structure, purity and in some cases also the crystallinity of the intermediate compounds. For this purpose IR and NMR spectra were collected whenever possible. IR spectra (nujol mull) were recorded on a Shimadzu FT-IR prestige 21, NMR spectra (in DMSO-$d_6$,) were recorded at 298 K on a Bruker Avance 400 instrument internally referenced to the $SiMe_4$ signal. Diffraction data were collected with overnight scans, 3-35° 2θ range, on a Bruker AXS D8 Advance diffractometer, equipped with a linear position-sensitive Lynxeye detector, primary beam

Soller slits, and Ni-filtered Cu-Kα radiation (λ = 1.5418 Å). The generator was set at 40 kV, 40 mA.

The two most important properties of our MOF compounds were the crystallinity and the thermal stability. Accordingly, X-ray powder diffraction analysis (XRPD) and simultaneous TG/DSC analyses were carried out. For X-ray measurements, thoroughly evacuated samples were analyzed to obtain diffraction patterns comparable to those reported by Dr. V. Colombo [57]. As proved by their extensive study of this materials, solvents does not affect the main structural features but only the values of the unit cell parameters. Nevertheless, we dried the washed precipitate in vacuum at 150 °C for 4 h prior to XRPD analysis for simplicity. In all cases, the crystallinity was confirmed by checking the characteristic diffraction peaks of related reference materials.

The thermal stability of the MOF compound has been evaluated by means of simultaneous TG/DSC analyses on a Netzsch STA 409 PC Luxx both in inert ($N_2$) and oxidative (air) atmosphere at a heating rate of 10 K min$^{-1}$.

## 2.3.1 Synthesis of the organic ligands

*Synthesis of 1,3,5-tris(1H-pyrazol-4-yl)benzene (H₃BTP).*

Unfortunately, the 1,3,5-benzenetriacetic acid as starting material was not commercially available but could be easily prepared with a two-step conversion of the cheap and commercially available 1,3,5-tris(bromomethyl)benzene. Thus, a nucleophilic substitution of the bromide by the cyanide anion was performed suspending NaCN (4.2 g, 0.086 mol) in DMSO (32 mL) in a 200-mL one-necked round-bottomed flask equipped with a magnetic stirrer bar and very slowly adding dissolved 1,3,5-tris(bromomethyl)benzene (10.2 g 0.029 mol in 32 mL of DMSO. The solution was left to stir at 40 °C for 10 h after which the reaction mixture was poured into ice-water (20 mL). The white solid, 1,3,5-tris(cyanomethylmethyl)benzene was filtered off and dried under vacuum at room temperature. This cyanomethyl derivative (1.45 g, 7.43 mmol) was dissolved in a mixture of water (2.5 mL) and concentrated $H_2SO_4$ (2.2 mL) and was heated at reflux (140 °C) for

5 h. The solid was extracted with several portions of diethylether and recrystallized from acetic acid to afford 1,3,5-benzenetriacetic acid. Afterwards the VHA formylation was adopted: under inert atmosphere (N$_2$) the white 1,3,5-benzenetriacetic acid (1.5 g, 6 mmol) was added to the 0 °C mixture of POCl$_3$ (5 mL) and DMF (4 mL) in a 50 mL two-necked round-bottomed flask equipped with a magnetic stirrer bar, N$_2$ inlet and condenser. After being refluxed at 85 °C for 48 h and left at room temperature overnight, the reaction mixture was poured into ice (50 mL) and successively a saturated NaClO$_4$ aqueous solution (2.6 g) was added. The yellow tris(perchlorate) salt (1.5 g, 2 mmol) was subjected to heterocyclization with hydrazine monohydrate (320 μL, 10.37 mmol) in ethanol (1 mL). After heating at 90 °C for 4 h, the mixture was filtered and the light-yellow H$_3$BTP precipitate was washed with methanol (3 x 10 mL) and dried under vacuum.

### Synthesis of 1,4-Bis(pyr*azol-4-yl)benzene (H2BDP)

The synthesis of H$_2$BDP organic linker has been previously published by Maspero and co-workers [60] and consist in the heterocyclization of *p*-phenylenbis(malondialdehyde) or its synthetic equivalents with hydrazine. The ligand was prepared from commercially available *p*-phenylenediacetic acid, starting with the Vilsmeier-Haack-Arnold (VHA) formylation reaction. Under N$_2$ atmosphere, cold POCl$_3$ (22.3 mL, 0.23 mol) was added to ice-cooled anhydrous N,N-dimethylformamide (DMF, 95 mL, 1.22 mol) in a 200-mL two-necked round-bottomed flask equipped with a magnetic stirrer bar, N$_2$ inlet and condenser. Then *p*-phenylenediacetic acid (7.86 g, 0.04 mol) was added. After being refluxed for 7 h the reaction mixture was quenched by pouring it into ice (250 mL) and a saturated NaClO$_4$ aqueous solution (20 g) was added. The yellow residue was collected by filtration, washed with cold water to afford the 4,4'-bis-(1-dimethylamino-3-dime-thylimonio-prop-1-en-2-yl) biphenyl bis(perchlorate). This intermediate was supsended in EtOH (280 mL) and placed in a 500-mL round-bottomed flask under vigorous stirring, while 98 % hydrazine monohydrate (4 ml) was added dropwise. After being heating for 4 h at 90 °C, the pale-yellow solid was collected by filtration, washed with methanol (3 x 10 mL) and dried in vacuum at room temperature to afford pure H$_2$BDP powders.

## 2.3.2 Synthesis and characterization of the MOF compounds

*Synthesis of $Cu_3(BTP)_2 \cdot 8CH_3OH \cdot 10H_2O$*

$H_3BTP$ (0.15 g, 0.54 mmol) was dissolved in the solution of DMF (18.7 mL) and stirred at 60 °C in a Schlenk flask. Then $Cu(CH_3COO)_2 \cdot H_2O$ (0.1395 g, 0.7 mmol) was added and the mixture was heated under reflux at 150 °C for 8 h. Upon cooling, the brownish-grey $Cu_3(BTP)_2 \cdot 8CH_3OH \cdot 10H_2O$ precipitate was collected by filtering, washed with methanol and dried in vacuum. When necessary, the impure product was cleaned by washing in methanol (5 mL, at room temperature, for 2-3 h).

*Synthesis of NiBDP*

$H_2BDP$ (0.2 g, 0.95 mmol) was dissolved in DMF (20 mL) and stirred at room temperature in a Schlenk tube. Then $Ni(CH_3COO)_2 \cdot 4H_2O$ (0.235 g, 0.95 mmol) was added and heated to 150 °C and kept at this temperature for 5 h. The dark yellow/orange NiBDP precipitate was filtered off, washed with methanol and dried in vacuum. When necessary, the product was cleaned by washing the impure powder in DMF (5 mL, at 80 °C, for 4 h).

*Synthesis of ZnBDP*

$H_2BDP$ (0.2 g, 0.95 mmol) was dissolved in DMF (20 mL) and stirred at 60 °C in a Schlenk tube. Then $Zn(CH_3COO)_2 \cdot 2H_2O$ (0.208 g, 0.95 mmol) was added and the mixture was allowed to react for 5 h at reflux. The white ZnBDP solid was filtered off, washed with methanol and dried in vacuum. When necessary, the precipitate was washed in DMF (5 mL, at 80 °C, for 4 h).

*Thermal analysis of $Cu_3(BTP)_2$, NiBDP, ZnBDP*

As shown in Figure 2.5, 2.6 and 2.7, the samples undergo different weight loss events. The steps below 300 °C corresponds to the removal of solvent and guest molecules (methanol, DMF and water) while the steep weight loss at 350 °C for the Cu and Ni based MOF and at 460 °C for the Zn derivate is due to the decomposition of the framework. This

behaviour is in agreement with the evidence that pyrazolate bridged structures exhibit reasonably high thermal stability even in the presence of a reactive atmosphere.
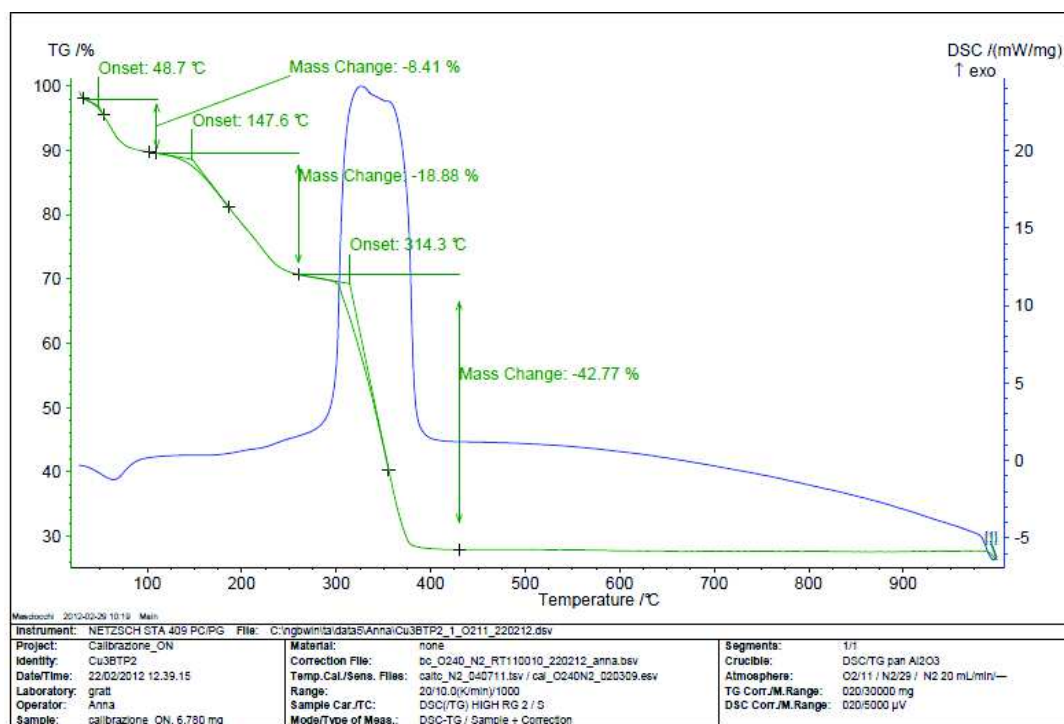


**Figure 2.5.** TGA data of $Cu_3(BTP)_2$ framework.
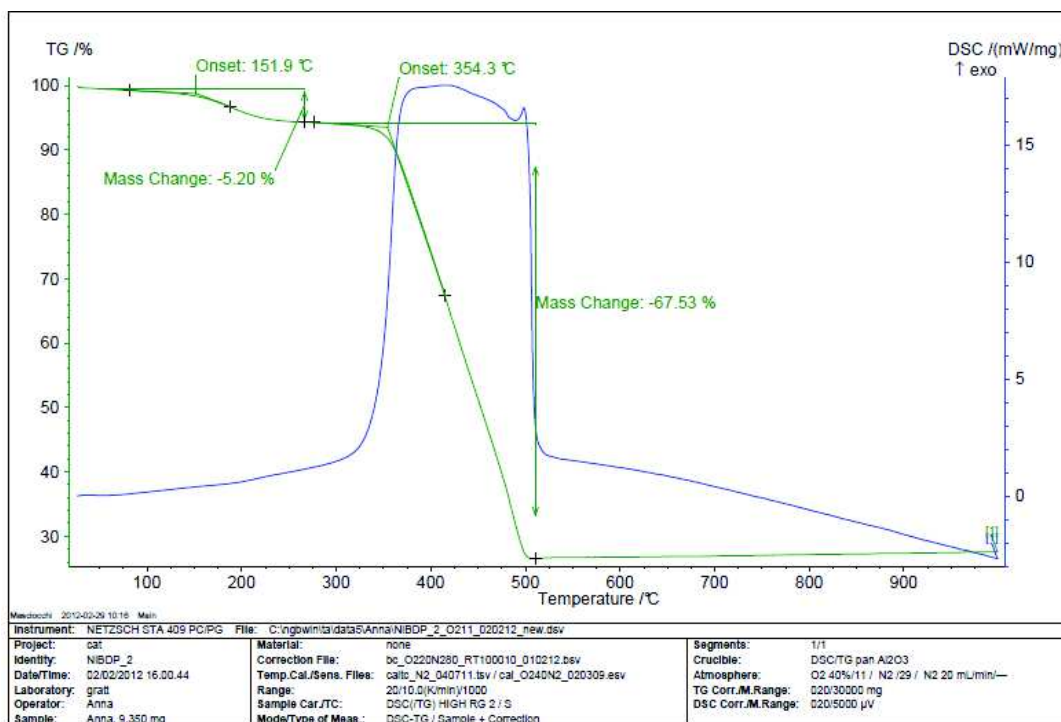
**Figure 2.6.** TGA data of NiBDP framework.
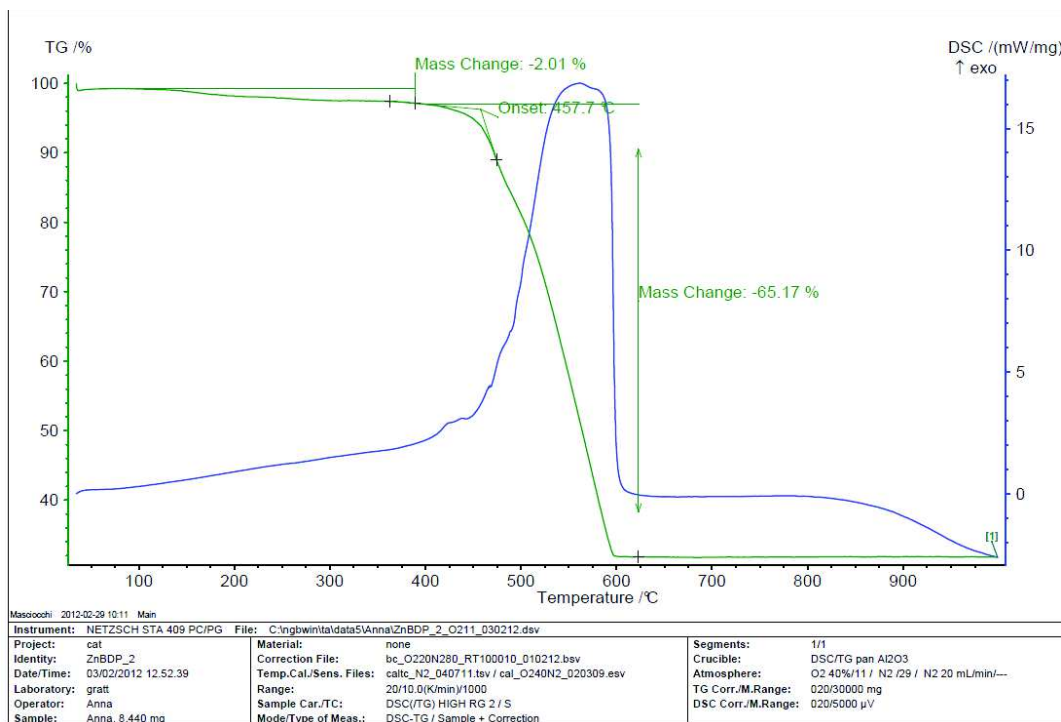


**Figure 2.7.** TGA data of ZnBDP framework.

# 3. Catalytic performance experiments

## 3.1 Introduction

Metal organic frameworks are interesting catalyst materials for heterogeneous gas phase reactions because of their porosity and high internal surface as described in paragraph 1. Obviously the limiting factor for the possible application is the accessible pore size and the nature of the catalytic center. Since our research was focused on a microporous, copper based coordination polymers, the simple oxidation reaction of propylene to propylene epoxide seemed to be adequate to test their catalytic activity. Firstly, this reaction involves small molecules as both reactants ($C_3H_6$, $O_2$) and product ($C_3H_6O$) can easily pass through the channels of the network. Secondly, this oxidation is well known to take place in the presence of metal (Ag, Ag-Au Cu) based catalysts [61, 62]. Moreover, the epoxidation of olefins (especially ethene and propene) is an extremely important class of catalytic reactions in the chemical industry because of their versatility as intermediates in both chemical technology and synthetic organic chemistry [63]. Propylene oxide is still industrially produced using two indirect processes: (i) the chlorohydrin process that produces environmentally unfriendly chlorinated organic byproducts as well as calcium chloride and (ii) the Halcon (hydroperoxide) process which produce equimolar amounts of coproducts, and requires high capital investment due to, among others, the high cost of hydrogen peroxide and the safety requirements associated with the use of concentrated $H_2O_2$-solutions [64]. Thus, a direct vapor phase selective oxidation of propylene to propylene oxide in the presence of molecular oxygen is still an up to date topic.

## 3.2 Experimental

The catalytic epoxidation of propene were performed on a properly designed apparatus. The schematic drawing of the experimental arrangement is reported in Figure 3.1. Tests were carried out at atmospheric pressure with a fixed-bed 5 mm i.d. quartz tubolar reactor. An appropriate amount of $Cu_3(BTP)_2$ was mixed with inert quartz sand in a 1:2 volume ratio and placed into the reactor tube. The catalyst bed height was about 0.5 cm (Figure

3.2). The reaction mixture consisted of a mixture of propene/oxygen/argon at 35.5, 3.5 and 14.7 ml/min flow rate, respectively and was generated by means of three calibrated mass flow controllers. Reactants and gaseous reaction products were analyzed by an online mass spectrometer (VG instruments, mod. VG2, 0–200 amu) controlling the argon, propene, oxygen, carbon dioxide propene-oxide channels. In addition, a downstream ice-cold trap was inserted in order to condense undesirable vapors. Experiments have been carried out with a 5-step temperature ramp as described below.
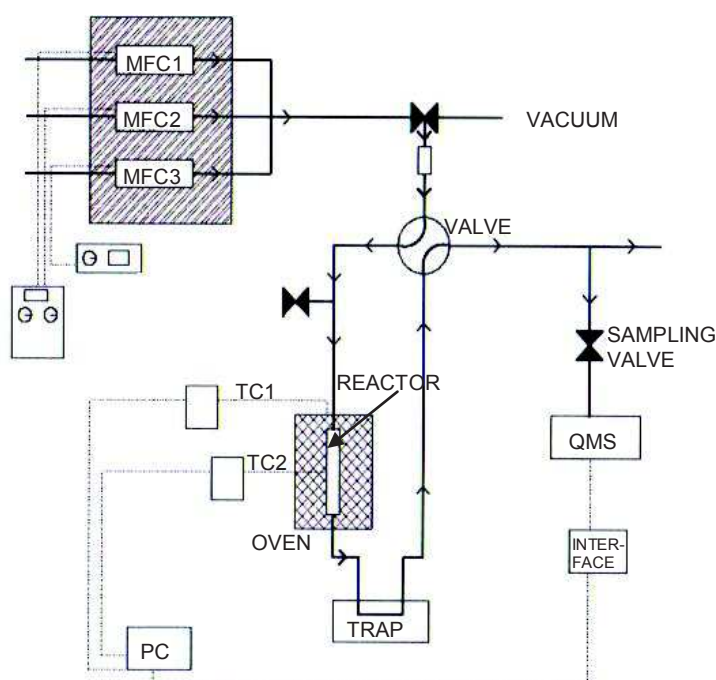


**Figure 3.1.** Scheme of the whole apparatus: MFC1-3 = mass flow controllers (5850 TR series Brooks); VALVE = 4-ways crossover valve, TC1 = chromel–alumel thermocouple connected to: on/off temperature controllers; TC2 = chromel–alumel thermocouple connected to programmable temperature controller and power supply.

- The oven temperature program was held at room temperature for 180 minutes to register the $CO/CO_2$ (for calibration of 28 and 44 amu signal), argon (20 amu) and propene (39, 41, 42 amu).

- After stabilization of MS signals, heating rate was set to 10 °C/min from RT to 100°C and held at 100 °C for 30 min.

- Heating from 100 to 150 °C at 10 °C/min rate and held for 30 min.

- Heating from 150 to 200 °C at 10 °C/min from and held for 30 min.

- Heating from 200 to 250 °C at 10 °C/min and held for 30 min.
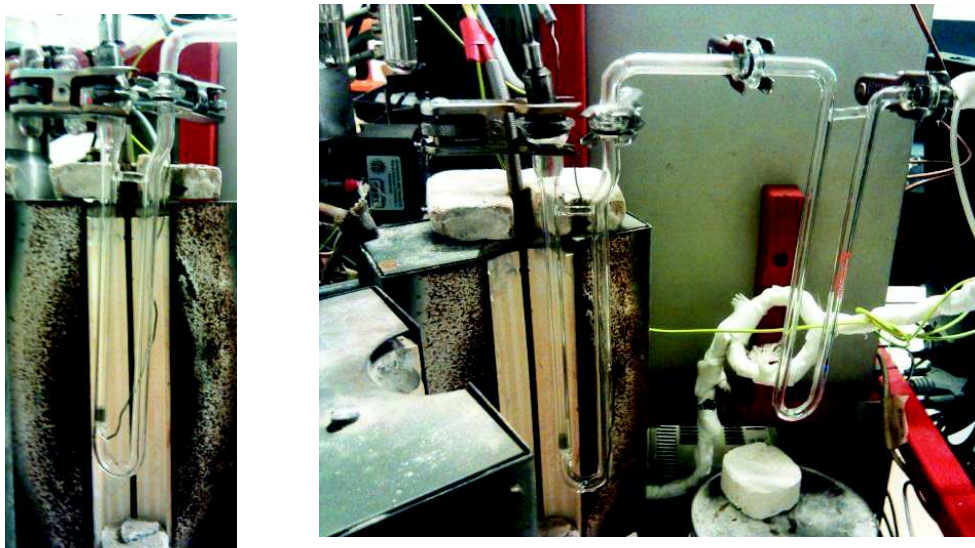


**Figure 3.2.** Picture of the quartz tubolar reactor (left), and of the configuration with oven and trap (right).

## 3.3 Results and discussion

The evident decrease of QMS signal of reagents along with the simultaneous increase of product's QMS signal prove that the catalytic reaction took place above 250 °C (Figure 3.3). The room temperature was maintained during the first part of the experiment (calibration of $CO/CO_2$ signals and the stabilization of the reaction mixture (Ar, $O_2$,

propene) signals) and only after more than 3 hours the temperature program could be started. The constant propylene and oxygen concentration in the temperature range of 25-250 °C points out that in these conditions the $Cu_3(BTP)_2$ MOF does not show catalytic activity toward the oxidation of propylene.
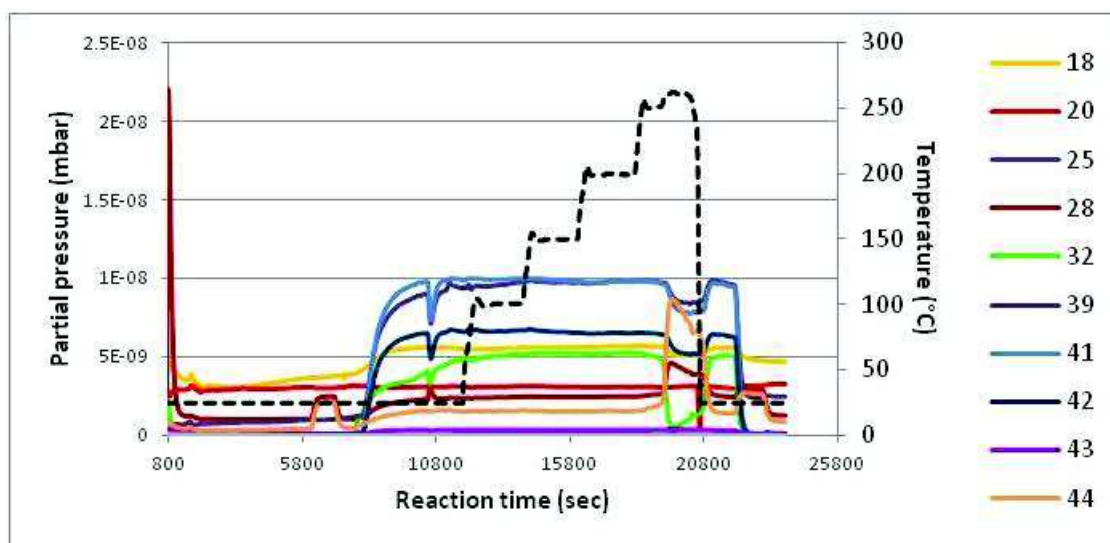


**Figure 3.3.** QMS signals of the reactants and products of the catalytic oxidation reaction (coloured lines) and the temperature program (black dotted line).
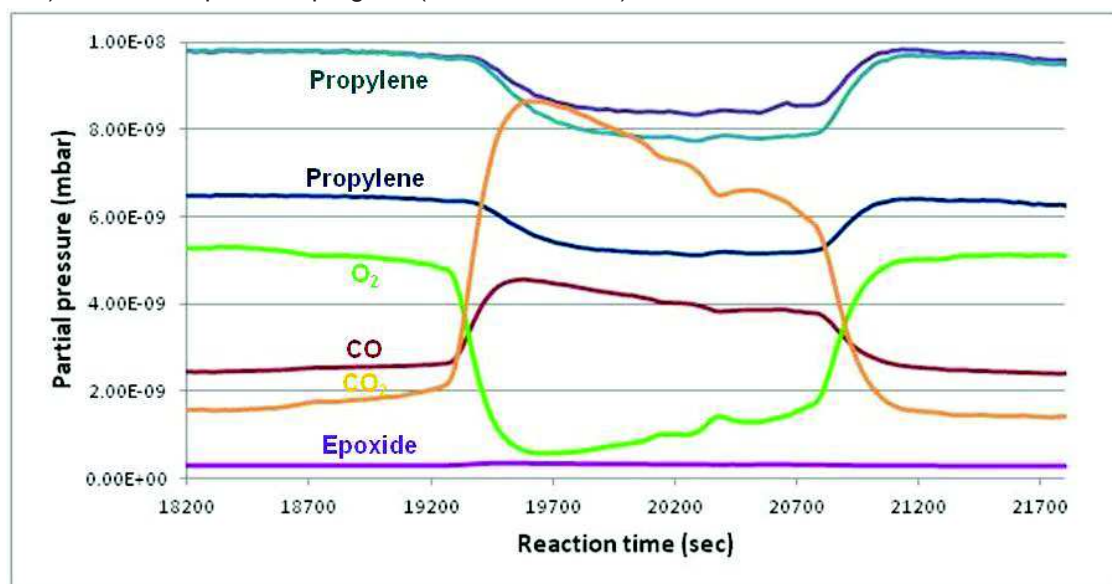


**Figure 3.4**. QMS signals of the reactants and products of the catalytic oxidation reaction at 250 °C.

31

At higher temperatures, as shown in more details on Figure 3.4, there are clear signs of reactions between propylene and oxygen: the selective oxidation reaction is confirmed by the significant concentration drop of reagents and the slight increase of propylene oxide signal. In contrast, a significant increase of $CO_2$ indicates a total combustion reaction. The exothermic nature of this process explains why the reactor temperature exceeded the designated threshold regulated by a precise temperature controller (Eurotherm 808). Further investigation were carried out to understand the reaction in more detail and also to better understand the role of the copper based MOF in this catalytic process.

*Post-catalytic analysis*

A small amount of the residual MOF was analyzed by X-ray power diffraction in order to understand the structural changes (Bruker AXS D8 Advance diffractometer; linear position-sensitive Lynxeye detector; primary beam Soller slits; Ni-filtered Cu-Kα radiation ($\lambda$ = 1.5418 Å)). The diffraction pattern is reported in Figure 3.5, and reveals that the crystalline MOF underwent combustion: moreover, the appearance of characteristic peaks at 35,4° 38,6° confirms the formation of copper oxide nanocrystals. This result seems to be in contrast with the thermal stability TGA, previously reported by Colombo [57] and with the earlier thermal stability studies (paragraph 2), which indicates a much lower than expected thermal stability.
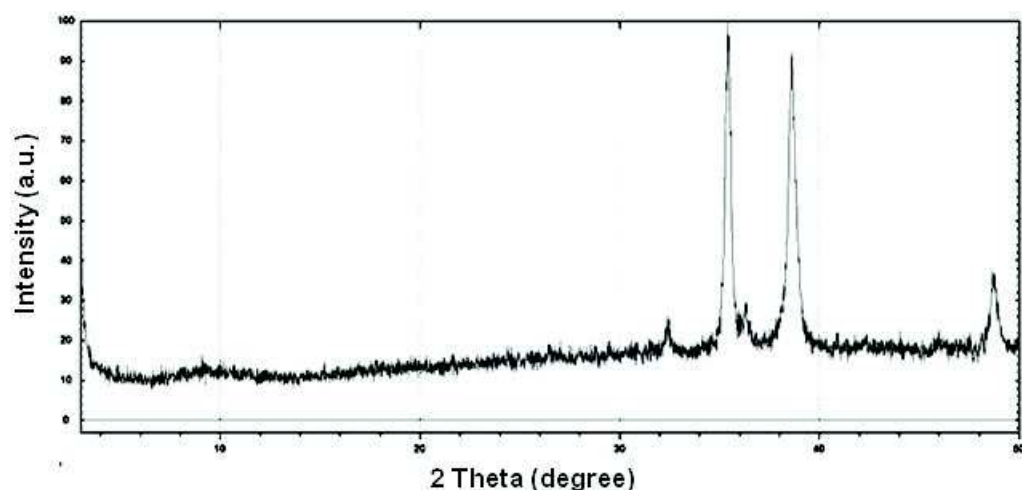


**Figure 3.5.** Powder X-ray diffraction pattern for the residual of $Cu_3(BTP)_2$ framework after catalytic experiments over 250 °C.

This discrepancy is only apparent and was rationalized as follows. The thermal stability of a MOF is frequently established by thermogravimetric or by thermodiffraction analysis and it is usually carried out in a flow of air or inert gas ($N_2$ or He) while raising progressively and rapidly (5-10°C/min) the temperature up to the complete destruction of the framework. However, these thermogravimetric data have to be carefully handled because structures that are stable under the limited time of TGA measurement at high temperatures, may undergo extensive damage if exposed to lower temperature for much longer times [65]. For this reason, we performed the TGA measurement under similar experimental conditions, changing only the temperature rate which was slower than the original one. Figure 3.6 shows the two TGA curves of $Cu_3(BTP)_2$ sample.
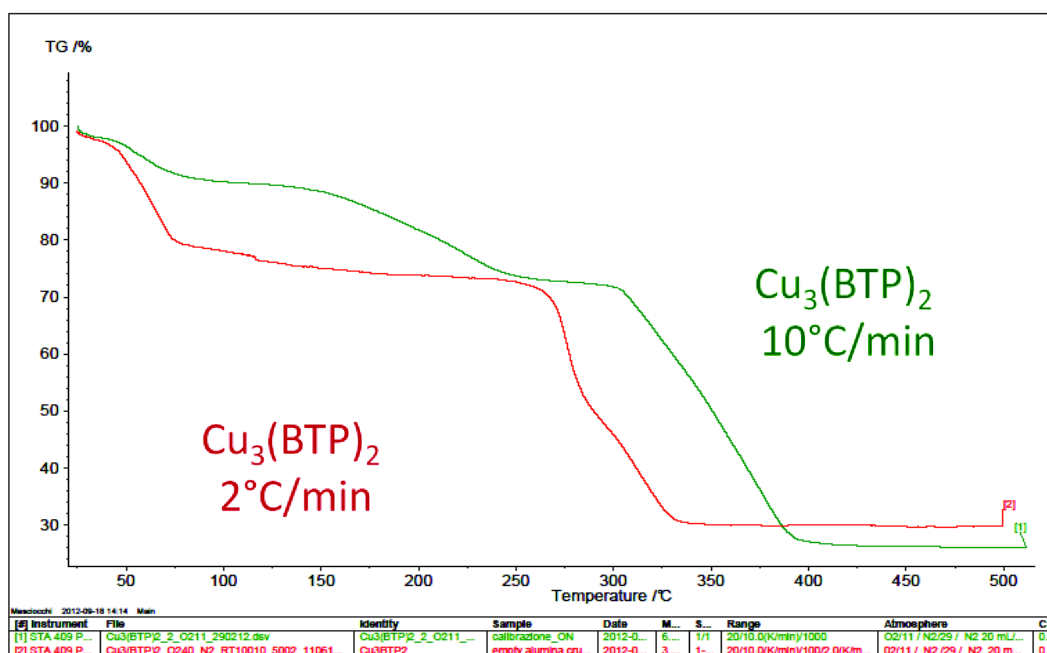


**Figure 3.6.** Comparison between the thermal gravimetric results of as-synthesized $Cu_3(BTP)_2$ obtained with different temperature programs.

This evidence perfectly matches the results emerged from catalytic tests and XRPD measurements, showing that this copper based metal organic framework does not exhibit sufficient thermal stability in oxidative environment.

# 4. CO adsorption on MOF

## 4.1 Introduction

As previously shown, the chosen MOF did not meet the requirements of the selected catalytic reaction, because of the lack of thermal stability at 250 °C.

Therefore, it is questionable to address where the reaction takes place: on the coordinatively unsatured copper centers, or on the CuO particles being formed during the thermal MOF decomposition.

It was then decided to test whether $Cu_3(BTP)_2$ possess readily accessible coordination sites, at temperatures where this MOF is surely and indefinitely stable. A powerful tool to study the accessibility and the nature of the copper sites is surely infrared spectroscopy coupled with the utilization of CO as probe molecule. In particular, Diffuse Reflectance Infrared Fourier Transformed Spectroscopy (DRIFTS) allows to record directly on powders the very intense IR signal of coordinated CO, whose position and stability is very sensitive to the nature of the adsorption sites. Accordingly, the accessibility of the coordination site of the $Cu_3(BTP)_2$ framework was tested in a prototype DRIFT flow reaction chamber developed previously in our laboratories [66].

## 4.2 Experimental

Before performing DRIFT measurements the copper-based compound was activated by heating at 200 °C for 24 h in vacuum to remove guest molecules such as $H_2O$ and solvents (DMF and methanol) from the pores. A small amount of $Cu_3(BTP)_2$ was loaded into the DRIFT cell in glove box and spectra were collected in vacuum, in He flow, in CO flow and under CO pressure. DRIFT spectra were recorded on a Digilab FTS-60 spectrometer equipped with KBr beam splitter and $N_2$ cooled linearized broadband MCT detector operating between 400 and 4000 $cm^{-1}$.

## 4.3 Results and discussion

As a general consideration, the intensities of the observed bands are very low, especially if we consider that the concentration of copper sites is quite high (~26 w/w%). This evidence clearly indicates that the accessibility of the copper sites to a molecule as small as CO is quite poor. In Figure 4.1 are reported the DRIFTS spectra recorded according to the following sequence: i) MOF under vacuum (empty channels); ii) MOF under flowing CO; iii) MOF under 3 bars of pure CO; iv) MOF after 30 min outgassing with helium.
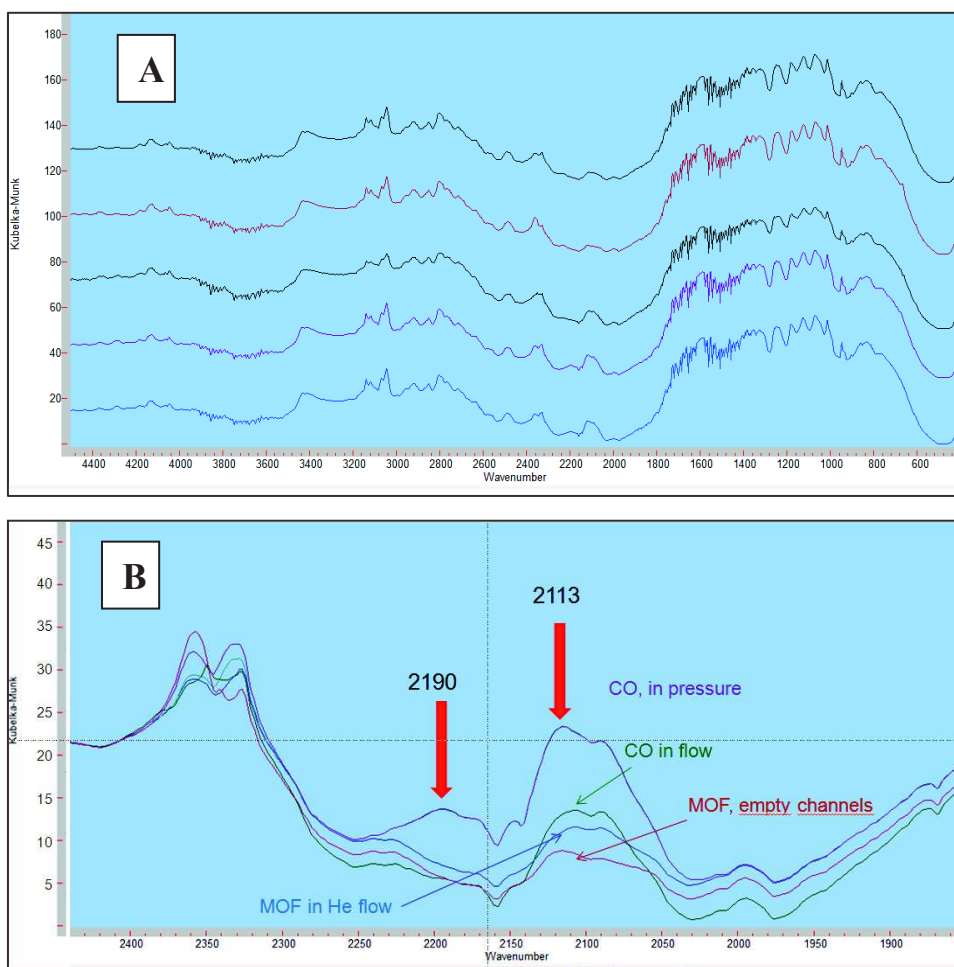


**Figure 4.1.** DRIFTS spectra recorded on $Cu_3(BTP)_2$ using CO as probe molecule. A) overall spectra; B) spectra of the CO stretching region.

When passing from vacuum to CO flow the raise of a band at 2113 cm$^{-1}$ (and a shoulder at 2080 cm$^{-1}$) is observed. The position of such bands are typical for Cu(I) species, even if 2080 cm$^{-1}$ represent a borderline frequency between Cu(I) and Cu(0) sites. This is quite in contrast with the formal oxidation state of copper in this framework, which is expected to be Cu(II). Cu(II) sites are evidenced working at higher pressure as shown by the appearance of a band at 2190 cm$^{-1}$ that can be surely ascribed to the presence of Cu(II) adsorption sites. As expected, this type of coordination is not stable and is completely lost after a 30 min outgassing with He, while the other two bands are partially retained.

However, independently from the nature of the MOF copper sites, the most interesting result of this DRIFTS study is probably the evidence that the accessibility of the copper sites is quite poor.

# 5. Conclusions

The reported data support the conclusions that the selected Cu-based MOF [$Cu_3(BTP)_2$] is not suitable for heterogeneous catalysis applications, at least above 220 °C in air. Indeed, XRPD and TGA measurements clearly showed that the copper based metal organic framework does not exhibit sufficient thermal stability in oxidative atmosphere. Moreover, independently from the adopted temperature, DRIFTS measurements proved $Cu_3(BTP)_2$ does not even possess readily accessible coordination sites, as shown by the poor adsorption of CO.

Two other MOFs, Zn- and Ni-based, were selected at the beginning of the present study. Given the unsatisfactory results obtained with $Cu_3(BTP)_2$, no aims for proceeding with tests on the other two were found, because of the inaccessibility of their inorganic node.

Nevertheless, the rigid pores of the 3D crystalline structure make indirectly Cu-, Zn- and Ni-based MOFs still right candidates for catalysis applications, given the possibility to enclose metal nanoparticles with catalytic properties. In particular, further investigations on Zn- and Ni-based MOFs are necessary, as they have on average larger pore sizes and higher thermal stability than Cu-based MOF.

# 6. References

1       Tomic E.A. J. Appl. Polym. Sci. 1965, 9, 3745.

2       Batten S.R., Hoskins B.F., Robson, R. J. Am. Chem. Soc. 1995, 117, 5385.

3       Kitagawa S., Kawata S., Nozaka Y., Munakata M.J. Chem. Soc., Dalton Trans. 1993, 1399.

4       Gardner G.B., Venkataramani D., Moore J.S., Lee S. Nature 1994, 374, 792.

5       Riou D., Ferey G.J. Mater. Chem. 1998, 8, 2733.

6       Yaghi O.M., Li H.L. J. Am. Chem. Soc. 1995, 117, 10401.

7       Furukawa H., Cordova K.E., O'Keeffe M., Yaghi O.M. Science 2013, 341, 1230444.

8       Eddaoudi M., Kim J., Rosi N., Vodak D., Wachter J., O'Keeffe M., Yaghi O.M. Science 2002, 295, 469.

9       Cavka J.H., Jakobsen S., Olsbye U., Guillou N., Lamberti C., Bordiga S., Lillerud K.P. J. Am. Chem. Soc. 2008, 130, 13850.

10      Chester A.W., Clement P. & Han S. Faujasite zeolitic materials. US patent 6,136,291A (24 October 2000).

11      Seth M.C. Chem. Rev. 2012, 112, 970.

12      Baerlocher C., Meier W.H., Olson D.H. Atlas of zeolite framework types, 6th Edition, Elsevier, 2007. (http://www.iza-structure.org/databases/).

13      Farha O.K., et al., Metal-organic framework materials with ultrahigh surface areas: Is the sky the limit? J. Am. Chem. Soc. 2012, 134, 15016.

14      Furukawa H., Go Y.B., Ko N., Park Y.K. Uribe-Romo F.J., Kim J., O'Keeffe M., Yaghi O.M. Inorg. Chem. 2011, 50, 9147.

15      Li J.R., Sculley J., Zhou H.C. Chem. Rev., 2012, 112 (2), 869.

16      Sun C.Y., Qin C., Wang C.G., (...), Lan Y.Q., Wang E.B. Advanced Materials 23 (47), 5629.

17      Lee J., Farha O.K., Roberts J., Scheidt K A., Nguyen S.T., Hupp J.T. Chem. Soc. Rev., 2009, 38, 1450.

18      Ricco R., Malfatti L., Takahashi M., Hillad A.J., Falcaro P.J. Mater. Chem. A, 2013, 1, 13033.

19      Taylor J.M., Dawson K.W., Shimizu G.K.H. J. Am. Chem. Soc. 2013, 135, 1193.

20      Silva C.G., Corma A., Garcıa H.J. Mater. Chem., 2010, 20, 3141.

21      Stavila V., Talin A. A., Allendorf M.D. Chem. Soc. Rev., 2014, 43, 5994.

22     McKinlay A.C., Morris R.E., Horcajada P., Ferey G., Gref R., Couvreur P., Serre C. Angew. Chem. Int. Ed. 2010, 49, 6260.

23     Kitagawa S., Kondo M. Angew. Chem. Int. Ed. 1997, 36, 1725.

24     Rosi N.L., et al. Science, 2003, 300, 1127.

25     Suh M.P., Park H.J., Prasad T.K., Lim D.W. Chem. Rev. 2012, 112, 782.

26     Millward A.R., Yaghi O.M. J. Am. Chem. Soc. 2005, 127, 17998.

27     Green Car Congress, www.greencarcongress.com/2010/10/basf-develops-method-for-industrialscale-mof-synthesis-trials-underway-in-natural-gasvehicle- tanks.html.

28     Ferey G. Chem. Soc. Rev., 2008, 37, 191.

29     Cychosz K.A., Wong-Foy A.G., Matzger A.J. J. Am. Chem. Soc. 2008, 130, 6938.

30     Cychosz K.A., Wong-Foy A.G., Matzger A.J. J. Am. Chem. Soc. 2009, 131, 14538.

31     Britt D., Tranchemontagne D., Yaghi O.M. Proc. Natl. Acad. Sci. USA 2008, 105, 11623.

32     Pan L., Olson D.H., Ciemnolonski L.R., Heddy R., Li J. Angew. Chem. Int. Ed., 2006, 45, 616.

33     Horcajada P., Serre C., Vallet-Regi M., Sebban M., Taulelle F., Ferey G. Angew. Chem. Int. Ed. 2006, 45, 5974.

34     Meek S.T., Greathouse J. A., Allendorf M.D. Adv. Mater. 2011, 23, 249.

35     Hoskins B.F. and Robson R. J. Am. Chem. Soc., 1990, 112, 1546.

36     Fujita M., Kwon Y.J., Washizu S., Ogura K. J. Am. Chem. Soc. 1994, 116, 1151.

37     Liu Jiewei, Chen Lianfen, Cui Hao, Zhang Jianyong, Zhang Li, Su Cheng-Yong. Chem. Soc. Rev. 2014, 43, 6011.

38     Tabares L.C., Navarro J.A.R., Salas J.M. J. Am. Chem. Soc. 2001, 123, 383.

39     Luz I., León A., Boronat M., Llabrés i Xamena F.X., Corma A. Catal. Sci. Technol. 2013, 3, 371.

40     Seo J.S., Whang D., Lee H., Jun S.I., Oh J., Jeon Y.J., Kim K. Nature, 2000, 404, 982.

41     Hasegawa S., Horike S., Matsuda R., Furukawa S., Mochizuki K., Kinoshita Y., Kitagawa S. J. Am. Chem. Soc. 2007, 129, 2607.

42     Serra-Crespo P., Ramos-Fernandez E.V., Gascon J., Kapteijn F. Chem. Mater. 2011, 23, 2565.

43    Song F., Wang C., Falkowski J.M., Ma L., Lin W. J. Am. Chem. Soc. 2010, 132, 15390.

44    Zhu C., Yuan G., Chen X., Yang Z., Cui Y. J. Am. Chem. Soc. 2012, 134, 8058.

45    Shultz A.M., Farha O.K., Hupp J.T., Nguyen S.T. J. Am. Chem. Soc. 2009, 131, 4204.

46    Feng D., Chung W.C., Wei Z., Gu Z.Y., Jiang H.L., Chen Y.P., Darensbourg D.J., Zhou H.C. J. Am. Chem. Soc. 2013, 135, 17105.

47    Guo-Qiang K. Chemical communications 2011, 47(39), 11005 -11007.

48    Ma L., Wu C.-D., Wanderley M.M., Lin W. Angew. Chem. Int. Ed. 2010, 49, 8244.

49    Zhang X., Llabrés i Xamena F.X., Corma A. J. Catal. 2009, 265 (2), 155.

50    Tanabe K.K. and Cohen S.M. Angew. Chem. Int. Ed. 2009, 48, 7424.

51    Tanabe K.K. and Cohen S.M. Inorg. Chem. 2010, 49, 6766.

52    Hwang Y.K., Hong D.Y., Chang J.S., Jhung S.H., Seo Y.K., Kim J., Vimont A., Daturi M., Serre C., Ferey G. Angew. Chem. Int. Ed. 2008, 47, 4144.

53    Nguyen H.G.T., Weston M.H., Farha O.K., Hupp J.T., Nguyen S.T. CrystEngComm. 2012, 14, 4115.

54    Sabo M., Henschel A., Froede H., Klemm E., Kaskel S., J. Mater. Chem. 2007, 17, 3827.

55    Maksimchuk N.V., Timofeeva M.N., Melgunov M.S., Shmakov A.N., Chesalov Y.A., Dybtsev D.N., Fedin V.P., Kholdeeva O.A. J. Catal. 2008, 257, 315.

56    Gascon J., Corma A., Kapteijn F., Llabrés i Xamena F.X. ACS Catal. 2014, 4, 361.

57    PhD thesis of Valentina Colombo, Synthesis, characterization and applications of highly stable pyrazolate-based metal-organic frameworks.

58    Colombo V., Galli S., Choi H.J., Han G.D., Maspero A., Palmisano G., Masciocchi N., Long J.R. Chem. Sci. 2011, 2, 1311.

59    Galli S., Masciocchi N., Colombo V., Maspero A., Palmisano G., Lopez-Garzon F.J., Domingo-Garcia M., Fernandez-Morales I., Barea E., Navarro J.A.R. Chem. Mater. 2010, 22, 1664.

60    Maspero A., Galli A., Masciocchi N., Palmisano G. Chem. Lett. 2008, 37(9), 956.

61    Lambert R.M., Williams F.J., Cropley R.L., Palermo A. J. Mol. Catalys. A 2005, 228, 27.

62    Geenen P.V., Boss H.J., Pott G.T. J. Catal. 1987, 77(2), 499.

63      Vaughan O.P.H., Kyriakou G., Macleod N., Tikhov M., Lambert R.M. J. Catal. 2005, 236, 401.

64      Suo Z., Jin M., Lu J., Wei Z., Li C. J. Nat. Gas Chem. 2008, 17, 184.

65      Gascon J., Corma A., Kapteijn F., Llabrés i Xamena F.X. ACS Catal. 2014, 4, 361.

66      Dal Santo V., Dossi C., Fusi A., Psaro R., Mondelli C., Recchia S. Talanta 2005, 66, 674.

# Chapter 2

(*article*)

## Applications of a true scanning reactor to planar catalysts with variable surface composition

**Applications of a true scanning reactor to planar catalysts with variable surface composition**

Marcello Marelli*[a] Anna Nemenyi,[b] Vladimiro Dal Santo,[a] Rinaldo Psaro,[a] Luca Ostinelli,[b] Damiano Monticelli,[b] Carlo Dossi,[b] Sandro Recchia.[b]

[a] CNR–Istituto di Scienze e Tecnologie Molecolari, Via Golgi 19, 20133 Milan, Italy

[b] Dipartimento di Scienza e Alte Tecnologie, Università dell'Insubria, 22100 Como, Italy

* corresponding author: Dr. Marcello Marelli (Ph.D.) - CNR–Istituto di Scienze e Tecnologie Molecolari Via C.Golgi 19, 20133 Milano (ITALY)- phone: +390250995632; fax: +390250314405

email: m.marelli@istm.cnr.it

**HIGHLIGHTS**

- A true scanning reactor for planar catalyst was developed

- Catalytic surfaces with low turnover frequencies could be tested

- A minimum circular area of 6 mm in diameter could be sensed by the apparatus

- High flexibility for different catalytic tests as hydrogenations and oxidations

- Real application for metal surfaces and coated surfaces

**ABSTRACT**

The development of a scanning reactor for planar catalysts is here presented. With respect to other existing models, this reactor is able to scan catalysts even with low turnover frequencies, with a minimum sensed circular area of about 6 mm diameter. The downstream gas analysis is performed with a quaprupole mass spectrometer. The performances of the apparatus are presented showing the results obtained for two different reactions: the hydrogenation of butadiene over palladium films and the oxidation of CO over a gold/titania catalyst. With the final setup true scans in both X and Y directions (or even in a previously defined complex direction pattern) are possible within a scan speed ranging from 0.1 mm/min to 5.0 mm/min.

**KEYWORDS**

- High throughput experimentation;
- Heterogeneous catalysis;
- Scanning reactor;
- Catalyst libraries.

## 1. INTRODUCTION

Combinatorial chemistry is a well-known methodology which, starting from the last decade of last century, has shown a significant increase in its utilisation and impact across many industrial and academic fields. The constant search of chemists for fast, cheaper and advanced synthetic processes spreads from the pharmaceutical sector through fine

chemicals, plastic, oil products, material science and heterogeneous catalysis, [1-3]. In this last field the utilisation of a combinatorial approach (instead of an empirical trial-and-error strategy), through a pragmatic high throughput experimentation (HTE), allows to substantially decrease the requested workload to obtain the best (or at least an improved) catalyst. Of course, a careful combinatorial strategy planning is requested before starting with the experimental work. In addition, the continuous and massive development of advanced statistical tools (such as the design of experiment DoE and other multidimensional data treatments) allows now to combine complex data set from different sources, yielding thus a deeper understanding of the properties of new materials [4]. In this context the availability of suitable analytic tools is mandatory to feed this complex machinery with robust and reliable datasets [5]. We are able to obtain a successful workflow only when all these three parts - e.g. the strategy planning, the data collection and the data handling - complement together. HTE methodologies are largely used in heterogeneous catalysis and several reviews are available [6-11]. Different analytical strategies are proposed using parallel reactors [11-13] or scanning reactors. Generally the latter are applied on flat catalyst and only few examples are available for real continuous scanning systems. A good approach lies in the synthesis of discrete area of active samples, spatially isolated each other in small well and tested one-by-one by a movable head [14-15]. Real spatially resolved test are reported using capillary glass probes: the reaction take place under the probe that samples the product gases and drives them to a mass spectrometer downstream [16-19]. In particular, the last cited reference shows a quite interesting configuration that can be successfully used with high- activity surfaces. If

highly active catalysts are tested, constrains related to reactants gas feed concentrations and to the minimum sensed area are quite mild: therefore it is possible to reach spatial resolutions down to 250 μm with feeding gas concentrations up to 5% [19].

As we will show later, if medium to low activity surfaces are tested, the apparatus constrains become difficult to comply with the consequence that the feeding gas mixture must be diluted (down to hundreds of ppm) and the sensed area must be enlarged, in order to observe a sufficient reactivity. In this work, we present the development of a which faces these problems, i.e. which is able to test with high sensitivity planar catalysts possessing medium to low activities. The system here presented is able to spatially scan a planar catalyst and test its catalytic activity continuously, and represents a further step along the evolution line of our reactor for planar surfaces [20]. With respect to that system we completely re-design the reactor probe to improve the overall efficiency and solve most of the technical problems previously encountered. All these points will be deeply discussed in this paper. The re-designed apparatus is now able to truly scan the reactivity of planar catalysts over both the x and the y axis. Finally, a tentative modelling of the probe capability next to the MS data handling is proposed.


## 2. EXPERIMENTAL

### 2.1 Apparatus design and setup

The apparatus is composed by three parts (Fig.S01): the heated steel reactor probe, the heated aluminum sample holder (mounted on a motorized XYZ stage) and the sealed

PMMA box that encloses the previous two parts and ensures a controlled, slightly over pressurized, inert environment (Ar). Even in this third generation prototype the gas reactant mix is driven onto the active surface where the reaction takes place through the reactor probe: the inert gas cushion around it avoids the gas dispersion from the interaction volume defined by the probe and the underlying surface. In the meantime, the controlled leakage dilutes the product gas mix extracted by the OUTLET manifold and driven to the QMS analyzer. With respect to previous models, the new reactor probe is now bigger and made of two parts (the outer and the inner body -figure 1A). The two pieces are designed and assembled together in order to obtain on the bottom part a concentric system centered on the inlet nozzle and surrounded by an annular cavity (having on the top the outlet gas port). The internal part of the probe drives over the catalyst surface the feeding gas mixture which is heated by a heating cartridge inserted from the top. The 30x3mm internal mixing camera is filled of small glass beads (d=1mm) just above the 0,5 mm restriction of the final nozzle to improve the heating efficiency. The heating temperature is controlled by a thermocouple and a digital controller (Eurotherm 808). The gas product mix is sampled by the annular manifold which is connected to a quadrupolar mass spectrometer (HIDEN-HPR20) by a common jet-separator interface.

Relevant changes were applied on the sample holder system, which in our previous publication was not able to perform a true scan because neither the X nor the Y axis were motorized. In the apparatus here presented the XYZ stage is now motorized with three stepping motors controlled by a unique user-made hardware which, in turns, is driven by a LabVIEW-based software. On the X and Y axis the movement resolution is 0.0104

mm/step, on the Z axis is 0.00294 mm/step. The fine gap between the active-surface and the reactor-probe on the Z axis is measured by a dial test indicator (MITUTOYO lever type, 513 series, 0,50/0,01 mm) placed next to the probe. The Z reference system is tuned prior every test at the same temperature used for the test itself.
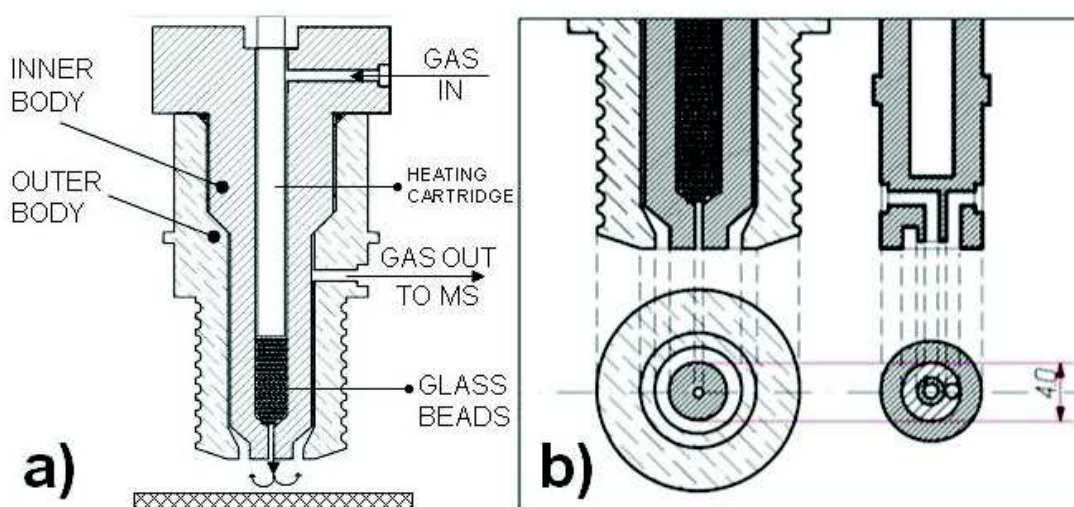


Figure 1. a) overall scheme of third generation reactor probe – b) detail of reactor probe third vs. second generation 2B (left and right respectively), side and bottom view.

### 2.2 Catalysts preparation

To test the performance of the scanning reactor we used two conceptually different active materials not homogeneously distributed over flat surfaces: i) a planar metal nanostrucured Pd film, and ii) a powder catalyst gently spread to coat a suitable sample holder.

The first specimen was a 20 nm thick palladium film deposited on a 10x30 mm silicon slide, obtained using a methodology reported elsewhere [21]. This system was already tested in a previous work of us with a different reactor design in the selective

hydrogenation of 1,3-butadiene, and is used here for comparative purposes [20]. To obtain active areas placed next to reference/inactive ones, Pd is ablated from the central part of the slide only, thus creating a 7x10mm inactive area (figure 2a): a laser ablation system (New Wave mod. UP266 – optimized conditions: $30mJ/cm^2$; spot size $50\mu m$) was used for this purpose.

The second specimen is a powder $Au/TiO_2$ (3% w/w Au loading) catalysts prepared by aqueous impregnation on commercially available $TiO_2$ (Titanium dioxyde Nanoactive): After calcination in air for 1h at 500 °C the support was impregnated with an aqueous solution containing the required amount of $HAuCl_4$ and stirred for 2h. The catalyst precursor was dried in air at 80°C overnight, and then reduced in flowing pure $H_2$ at 500°C for 1h. The $Au/TiO_2$ catalyst was previously tested in batch conditions at 80-100°C in the oxidation of CO to $CO_2$ as model reaction. The powder was dispersed in acetone in order to obtain a slurry and rub accurately on a proper drip tray (11x15x0.5 mm) dug on an aluminum slide. After a slow dry overnight, a compact powder film was obtained on the sample holder, and the whole surface had the same flat quota (figure 2b).
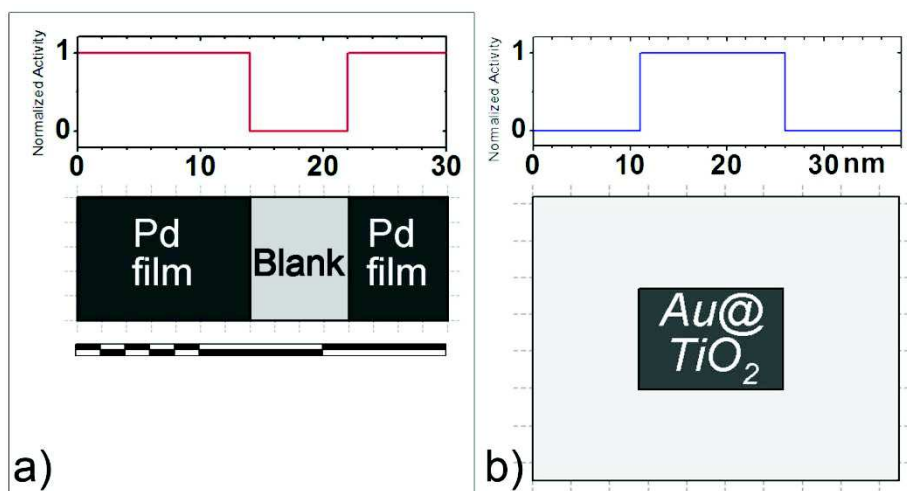
Figure 2 - Catalyst predicted activity and relative scheme of a) Pd film on Si Slide and b) Au@TiO$_2$ powder on a partially coated aluminum slide.

## 3. RESULTS AND DISCUSSION

### 3.1 New reactor probe design achievements

The core of the Scanning Catalytic Reactor for planar surfaces (SCR-PS) is the reaction chamber defined by the reactor probe and by the planar catalyst surface as shown in figure 1A. As above mentioned, a true scan is possible only if the reactor head never touches the catalyst surface, not forgetting that reactants and product should be confined in some way in a well-defined volume. According to the conceptual basis of the controlled leakage

system, this is achieved through a correct design of the probe head, through a fine balance of the head vs surface distance and of the inlet vs outlet gas flows. In particular, the annular surface of the outer body of the probe (which is very close to the catalyst surface) and the adjusted outlet gas flow, ensures a good local insulation of the reaction chamber. From another point of view the combination of this annular surface and the settings of gas flows allow a fine control of the leakage to or from the inert outer environment (the "gas-cushion" sealing system).

From a comparison between figure 1 and the figures reported in our previous work it can be immediately seen that the probe head was completely re-designed (Fig.S2). This novel design was necessary to solve some problems encountered with the first prototype that we will now discuss. The first problem we addressed in prototype n.2A was the thermal homogeneity along the gas line, from the reactor probe to the catalyst surface. In that prototype we used, as probe heating system, a wire heater rolled up around the probe and around the inlet steel gas tube. This system was rather good to heat the probe but the inlet gas was overheated. Considering that the pre-heating of the feeding gas at the probe temperature and its stability has an essential importance on the performance of the reactor, we decided to move to prototype n.2B. In this second generation prototype we used a heating cartridge inserted in the upper part of the probe, just above the gas flow (figure 1b). This solution was however not satisfactory because the reduced contact time between the gas flow and the hot probe was not sufficient to pre-heat reactants correctly. On the third generation prototype here presented we moved the heating cartridge inside the gas flow providing an extensive and direct contact surface between reactants and the heating

cartridge. Therefore, the gas is pre-heated inside the inner probe body. Moreover an internal mixing camera filled with small glass beads was created above the nozzle. Exploiting their large surface/volume ratio it is possible to ensure a very efficient and homogeneous thermal distribution between the probe and the gas. With this solution reactants are perfectly thermalized at the probe temperature.

The second solved problem refers to the need of increasing the catalytic conversion through a better contact between reactants and the catalytic surface. For prototypes n.2A/B we used the same reaction chamber geometry which is not optimized in terms of reactant/catalyst contact. This is really the key point as the active surface of a planar catalysts is very low in comparison to powdered catalysts. Taking into account that reagent flows as low as 0.5 mL/min can be used, prototypes n.2A/B allow part of the reagents to go directly to the outlet port without touching the catalytic surface. The optimized geometry of prototype n.3 solves this problem as the gases from the small 0.5 mm diameter central hole are forced to pass over the catalytic surface before being aspirated by the outlet port. As can be seen in figure 1, this is possible because the gases from the central nozzle are maintained in close contact with the catalysts surface for a diameter of 4 mm: to reach this result it was necessary to lower the quota of the inner part at the same level of the outer one. As it will be described later the true area sensed by the SCR-PS is 28 mm$^2$ ca.: this means that true diameter sensed by the SCR-PS is 6 mm ca.. This interaction area is larger enough to test the activity of the different catalytic systems.

The last problem we encountered with prototypes n.2A/B concerns the evidence that the results of scan tests varied as a function of the scan direction. This was ascribed to the not

uniform aspiration pattern. Conversely, the new symmetric design ensures homogeneous sampling both in static mode and during the scan movement in every direction. Accordingly the latest arrangement with the lined-up IN-nozzle/annular-OUT, allows a true 2D scan, free of artifacts due to the scanning directions. As we will show later this modifications on the reactor probe improved the performance of the scanning reactor not only in terms of absolute sensitivity but also in terms of scanning capabilities.

## 3.2 Evaluation of the controlled leakage performance

The performances of the controlled gas leakage system was evaluated in isokinetic conditions, i.e. using an inlet Ar flow (1,5 mL/min) equal to the outlet flow. The outer gas was air at atmospheric pressure and room temperature. To evaluate the dilution degree of the inlet gas (Ar), the outlet gas mixture was monitored by a QMS analyzer on mass channels 20 amu ($Ar^{++}$), and 28 amu ($N_2^+$): the nitrogen signal of air, together with the decrease of the Ar signal, are used to quantify the mixing between the outer an inner gases. We proceeded as follows: 1) firstly we recorded the signals with the inlet Ar closed (these signals are representative of 100% leakage); 2) then we recorded the signals of Ar bypassing the reactor probe (these signals are representative of the 0% leakage); 3) the probe was approached to 12 µm from the substrate and, after turning online the reactor probe, the inlet/outlet flows were balanced; 4) the gas leakage trend was then followed varying the probe/catalyst gap stepwise from 12 to 210 µm. The results of this test are reported in figure 3.

With a probe/catalyst gap equal to 12 μm we recorded a 14% mixing level of the outer gas in the inner one. This mixing level progressively increases as the distance from the surface increases too, reaching about one half (46%) at the maximum gap.

As expected, the controlled leakage system guarantees the best insulation at smaller distances, where it is possible to recover nearly 90% of the gas. Even at low gaps the system shows a good stability but small changes on Z axis causes significant signal fluctuations: this behavior is already known, and can be used to control the distance gap using a feedback logic [19]. With respect to our previous prototypes, the general improvements applied to the probe design caused a significant enhancement in terms of gas recovery percentage which, in turns, enhances the overall sensitivity. The operational conditions for this test were close to the ones used in catalytic tests, where the probe was placed at 50μm distance from the catalyst surface and the gas concentration is diluted about 30%. As a final consideration, it should be reminded that the performances of the controlled leakage system can also be varied passing from isokinetic to non-isokinetic conditions: as an example if contaminations from the outer environment should be avoided, the inlet gas flow can be substantially increased (maintaining the outlet flow constant) in order to decrease back diffusion of contaminants.
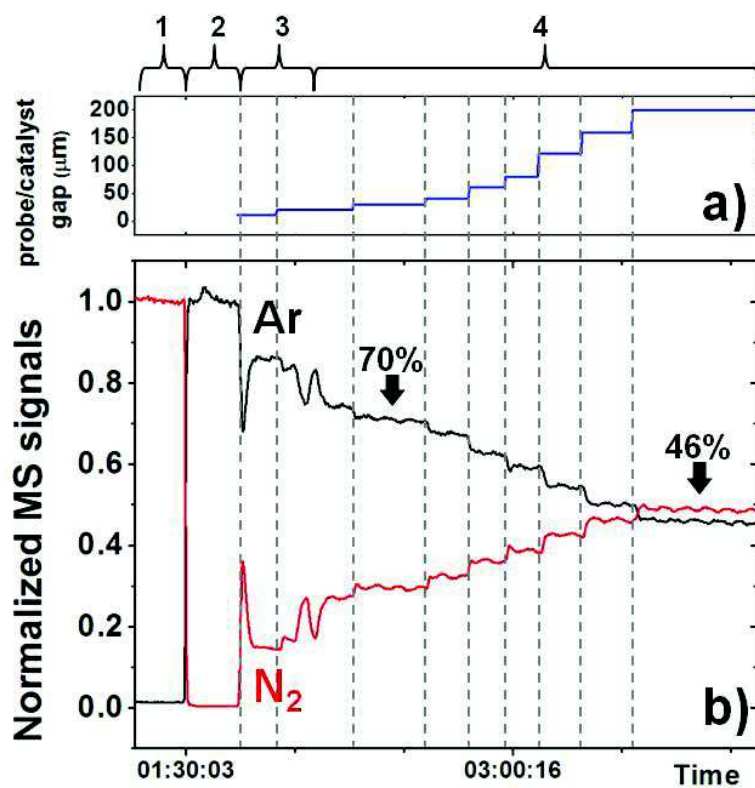
Figure 3. **a)** Probe/catalysts gap vs time at the following stepwise values: 12, 21, 30, 42, 62, 80, 122, 160, 201 μm and **b**) related normalized Ar and $N_2$ MS signals vs time along: 1) 100% N2 signal – 2) 100% Ar signal – 3) probe position settle and MS online connection – 4) fine probe movement on Z axis (21-201μm)

**3.3 Catalytic tests**

To prove that the new instrumental design is capable to resolve the spatial catalytic activity of a planar catalyst under scan conditions we choose two well-known reactions: the hydrogenation of 1,3-butadiene on Pd film [20, 22-23] and the oxidation of CO to $CO_2$ on Au NPs supported on $TiO_2$ powder [24]. Along the paper purpose, the catalyst role is to test the reactor and not vice versa. We test powder catalyst, properly prepared, in order to check the reactor capability on more complex surfaces, miming a powder-coated surface, more attractive as industrial application with respect to metallic thin films.

*3.3.1 Hydrogenation of 1,3-butadiene on Pd film*

The reaction mixture was composed by 1,3-butadiene 416 ppmv, hydrogen 833 ppmv, argon 833 ppmv in helium carrier gas. The reaction was monitored by mass spectrometry on channels: 53 amu (1,3-butadiene), 58 amu (butane), 2 amu (hydrogen) 56 amu (butene), 20 amu (argon) and 4 amu (helium). Preliminary experiments were done using a combination of a Pd film slide and a Si blank reference placed side by side, but this configuration never achive a perfect alignment on the z –axis. The system is sensitive to the distance between the surface and the reactor head and this unalignment generates noisy MS signals. Accordingly, we decided, to use a single modified slide as described in the experimental section. After placing the sample on the sample holder the PPMA box was hermetically closed and the internal environment was outgassed with Ar at a high flow rate (1 L/min). The planar Pd film catalyst was in-situ pretreated with $H_2$ (5 mL/min) at 100°C slowly sweeping the surface at 0.6 mm/min over the whole investigated path. The catalytic

tests were performed at 100°C, positioning the probe at 50 μm from the surface. The input/output flow rates were set at 1 mL/min and 1.5 mL/min respectively. The surface was scanned several times at different speed: MS signals for 1,3 butadiene (reactant) and Butene (product) are reported in figure 4. The signal trends highlight qualitatively a good sensitivity over the surface and a net increasing of catalytic conversion recorded on the edges of the active areas, regardless of the scan speed.
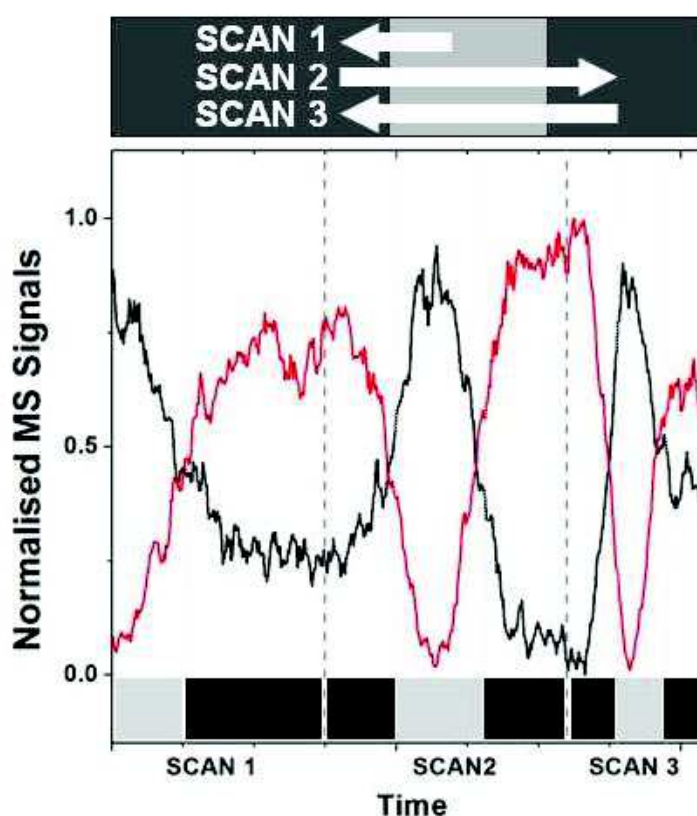


Figure 4. Normalized MS signal for 1,3 butadiene (reactant, 53amu, black) and butane (product, 56 amu, red) as a function of time for three different scan directions and speeds (dark grey = active area; light gray = not active area). SCAN 1: 0.2 mm/min; SCAN 2: 0.4 mm/min; SCAN 3: 0.8 mm/min.

*3.3.2 CO oxidation on Au/TiO$_2$*

The oxidation reaction was performed in a similar manner as described above for the hydrogenation. CO 500 ppmv and O$_2$ 5%, Ar 1000 ppmv in helium were used as reactants, internal standard and carrier gas, respectively. The reaction was followed by monitoring the mass channels of 28 amu (CO), 32 amu (O$_2$), 44 amu (CO$_2$), 20 amu (Ar) and 4 amu (He). Helium was used to correct instrumental drifts. The Au/TiO$_2$ catalyst is active without any in-situ pretreatment. This kind of test was unsuccessfully performed using the second generation reactor head (not published), probably due to the lower sensitivity of that prototype. The reaction profile, recorded by MS on mass channel 44 is shown in figure 5. The signal increased rapidly when the probe moves from the blank site A (aluminum) to the catalytically active Au/TiO$_2$ site B. The first run was performed at 80°C at a relatively high scan speed 1 mm/min (from 5 mm to 20 mm): at this temperature a net increase (+41% ca.) in the CO$_2$ signal is detected. The temperature was then increased to 100°C in a stationary position. In this way we observe another increase (+6% ca.) of the MS signal: in this way we proved the ability of the apparatus to detect changes in activity due to temperature changes. From this point, we performed the back scan (from 20 mm to 5 mm) at a slower scan speed (0.5mm/min). Also in this case, the system was able to detect the decrease of the activity recovering the values detected at the beginning of the initial scan (inactive surface).
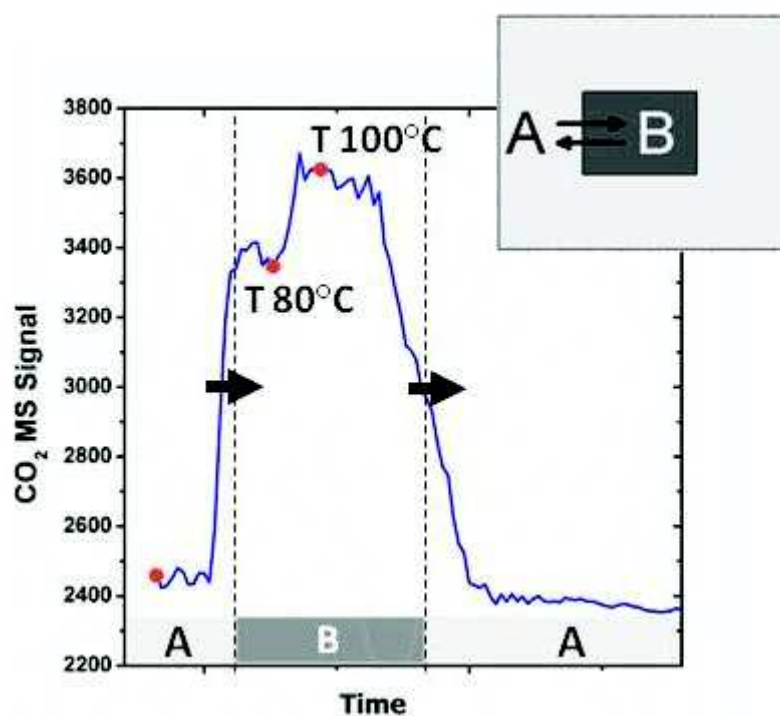
Figure 5. $CO_2$ (44 amu) MS signal vs. time along the oxidation catalytic scan tests over Au/$TiO_2$.

## 3.4 Scan model and data handling

The data recorded by the MS system were modeled in order to correctly evaluate the area sensed by the probe: we have in fact to consider that, as our reactor works in controlled leakage conditions, no physical constrains are used to define the sensed area. This information may be extracted from the previously shown activity plots through a sequence of several simple steps (Fig.S3).

Let's start with a preliminary consideration: if the sensed area is infinitely small, we would have recorded a staircase reactivity profile, as the catalytic surface steeply changes from

active to blank/inactive along the X axis (fig.2). As the reactor probe has instead finite dimensions the shape of the reactivity profile cannot be a staircase. To model it we propose a simple but reasonable model (Fig.S4): we assume that the sensed area is circular and that the normalized activity is 1 or 0 when all the sensed area is on the active or blank surface, respectively. For all the intermediate situations, i.e. when the probe is passing from the active to the blank surface, the activity is calculated as the ratio between the sensed area which is actually on the active part and the total sensed area. The parameter that we would like to fit is the diameter of the sensed area: the real probe model describes the steps of the staircase profile as a quasi-sigmoid function where higher slopes correspond to a small probe diameter and all the probe sets intersect on the edge at 0.5 value.

Four different set of probe diameters are shown in figure 6b: i) 0.5 mm which is the size of the inlet gas; ii) 4 mm which is the diameter of the bottom part of the inner body; iii) 6 mm, which is the size of the gas expansion chamber under the probe closed by the leakage system; iv) 8 mm which represents the extended area under the probe including also part of the external body.

Here we presented the model referred to the scan at speed 0.8 mm/min: the sampling rate is 0.2 mm/point due to the fixed MS sampling time (4 pts/min). The raw data shown in figure 6a are collected across the edge (which is located at x=22mm), on the range 17mm-29mm, from the blank surface to the active one. From these raw data, a sigmoid shape on signals of both reactant and product is clearly visible. On both profiles a mathematical fitting with a sigmoid Boltzmann Function is tentatively applied and reported in figure 6a, too. In order to compare the data with the scan model, the Boltzmann sigmoid functions are normalized

in the range [0-1]. In figure 06b the data of products are compared to the set of model probe diameters.
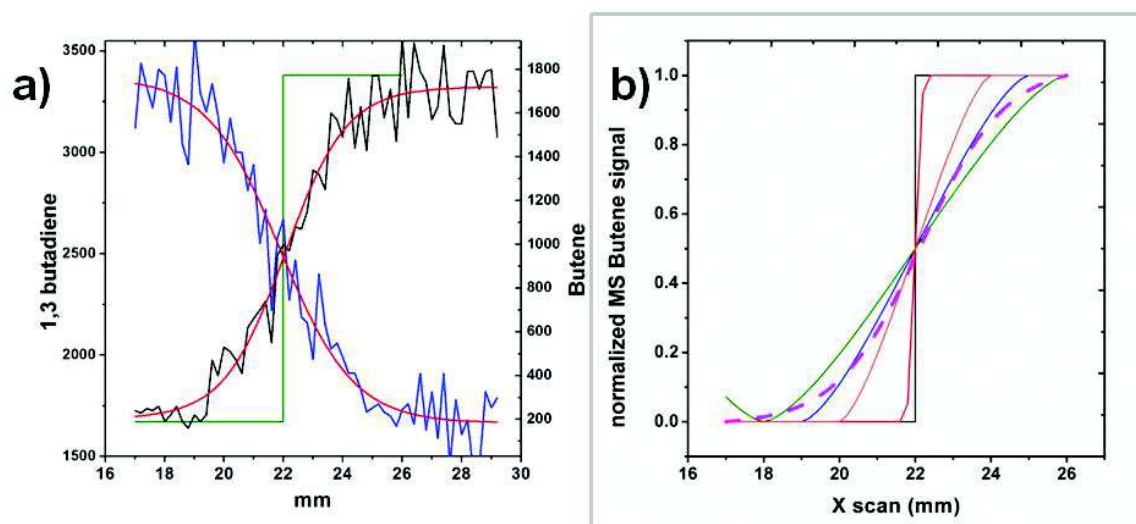


Figure 6. a) Raw MS signals for 1,3 Butadiene (blue) and Butene (black) on scan range [17-29 mm]; in red the Boltzmann sigmoid fitted on data and in green the theoretical staircase step; b) Scan Model calculated for probe diameter quasi-punctiform (black), 0.5mm (red), 4mm (orange), 6mm (blue) and 8 mm (green) for Butene. On dashed magenta profile the Boltzmann sigmoid calculated on real data.

The scan model for a probe diameter of 6 mm fits well with the test data around the central part of the sigmoid: the slope of the two curves is rather similar (1.13 vs. 1.00) and strongly different from the others. We could then suggest that the true area sensed by our reactor probe is close to 6 mm in diameter around the central inlet gas nozzle.

Finally, it is interesting to note that we have also checked that a change in the scan speed affects the slope of the sigmoidal curve in the time domain only (as could be obviously expected), while this does not happen if the data are reported in the spatial domain: this means that the response time of the whole apparatus is sufficiently fast to follow correctly the activity of the underlying catalyst without introducing unwanted instrumental artifacts.

## 4. CONCLUSIONS

We have shown in this paper that the developed apparatus is able to sense the reactivity of different types of surfaces and in different reaction conditions. The sensed area was optimized in order to observe the reactivity of catalysts with low turnover frequencies (of course, if catalysts with higher turnover frequencies are studied a reduction of the sensed area trough a scale down of the reactor probe is possible). Finally, the modular design of the apparatus allows a simple replacement of the head probe. With properly designed heads, other applications such as photocatalytic tests and/or surface modifications can be foreseen.

**REFERENCES**

[1] D. Farrusseng, Surf. Sci. Rep. 63 (2008) 487.

[2] W.F. Maier, K.St_we, S.Sieg  Angew. Chem. Int. Ed.46 (2007) 6016 – 6067.

[3] P. P. Pescarmona, P. A. Jacobs Catalysis Today 137 (2008) 52–60

[4] S. A. Schunk, N. Böhmer, C. Futter, A. Kuschel, E. Prasetyo, T. Roussière in: J.J Spivey, Y.  Han, K. M. Dooley (Eds) Catalysis, Volume 25, Royal Society of Chemistry , 2013, pp.172-215.

[5] R. Potyrailo, I.Takeuchi Meas. Sci. Technol. 16 (2005) 1–4.

[6] R. Potyrailo, K.Rajan, K.Stoewe, I. Takeuchi, B. Chisholm, H.Lam ACS Comb. Sci. 13 (2011) 579–633.

[7] B.Jandeleit, D.J. Schaefer, T.S. Powers, H.W. Turner, W. H. Weinberg Angew. Chem. Int. Ed. 38 (1999) 2494-2532.

[8] P.Cong, R.D. Doolen, Q. Fan, D. M. G. , S. Guan, E. W. McFarland, D. M. Poojary, K. Self, H. W. Turner, W. H. Weinberg,  Angew. Chem. Int. Ed.4 (1999) 38.

[9] Jefferson D. Revell, Helma Wennemers, in: Thomas Schrader (Eds), Creative Chemical Sensor SystemsEditors: - Part II: Creative Detection Techniques - Identification of Catalysts in Combinatorial Libraries , Springer-Verlag,  2007,  p. 251.

[10] A. Holzwarth, P. Denton, H. Zanthoff1, C. Mirodatos  Catalysis Today 67 (2001) 309–318.

[11] S. Senkan  Angew. Chem. Int. Ed. 40 (2001) 312 – 329.

[12] K. Gao, L. Yuan, L. Wang J. Comb. Chem. 8 ( 2006) 247-251.

[13] Jiang P. Yi, Zhi G. Fan, Zheng W. Jiang, Wen S. Li, and Xiao P. Zhou J. Comb. Chem. 9 (2007) 1053–1059.

[14] K. Eckharda, O. Schlu¨terb, V. Hagenb, B. Wehnerb, T. Erichsena, W. Schuhmanna, M. Muhlerb Applied Catalysis A: General  281 (2005) 115–120.

[15] M. Orschel, J. Klein, H. Schmidt, W.F. Maier Angew. Chem. Int. Ed. 18 (1999) 38.

[16] M. Roos, J. Bansmann, D. Zhang, O. Deutschmann, R. J. Behm1 the Journal of Chemical Physics 133 (2010) 094504.

[17] M. Roos, S. Kielbassa, C. Schirling, T. Häring, J. Bansmann, and R. J. Behm Review of Scientific Instruments 78 (2007) 084104.

[18] E. D. Rus, H. Wang, A. E. Legard, N. L. Ritzert, R. B. Van Dover, H. D. Abruña Review of Scientific Instruments 84 (2013) 024101.

[19] Nan Li, Jens Assmann, Wolfgang Schuhmann, Martin Muhler Anal. Chem. 79 (2007) 5674-5681.

[20] M. Marelli, L. Ostinelli, V. Dal Santo, P. Milani, R. Psaro, S. Recchia Catalysis Today 147 (2009) S170–S175.

[21] E. Suljovrujic´, M. Mic´ ic´, S. Demic, V.I. Srdanov, Appl. Phys. Lett. 88 (2006) 121902.

[22] L. Piccolo, A. Valcarcel, M. Bausach, C. Thomazeau, D. Uzio, G. Berhault, PCCP 10 (2008) 5504.

[23] . V. Dal Santo, A. Gallo, A. Naldoni, L. Sordelli, Inorg. Chim. Acta 380 (2012) 216-222.

[24] K. Christmann, S. Schwede, S. Schubert, W. Kudernatsch, ChemPhysChem 11 (2010) 1344-1363.

SUPPLEMENTARY MATERIAL

**Applications of a true scanning reactor to planar catalysts with variable surface composition**

Marcello Marelli*[a] Anna Nemenyi,[b] Vladimiro Dal Santo,[a] Rinaldo Psaro,[a] Luca Ostinelli,[b] Damiano Monticelli,[b] Carlo Dossi,[b] Sandro Recchia.[b]

[a] CNR–Istituto di Scienze e Tecnologie Molecolari, Via Golgi 19, 20133 Milan, Italy
[b] Dipartimento di Scienza e Alte Tecnologie, Università dell'Insubria, 22100 Como, Italy

* corresponding author: Dr. Marcello Marelli (Ph.D.) - CNR–Istituto di Scienze e Tecnologie Molecolari Via C.Golgi 19, 20133 Milano (ITALY)- phone: +390250995632; fax: +390250314405
email: m.marelli@istm.cnr.it

Fig.S1-Overall apparatus picture of the three parts: the PMMA box, the reactor probe and the motorized XYZ sample holder.
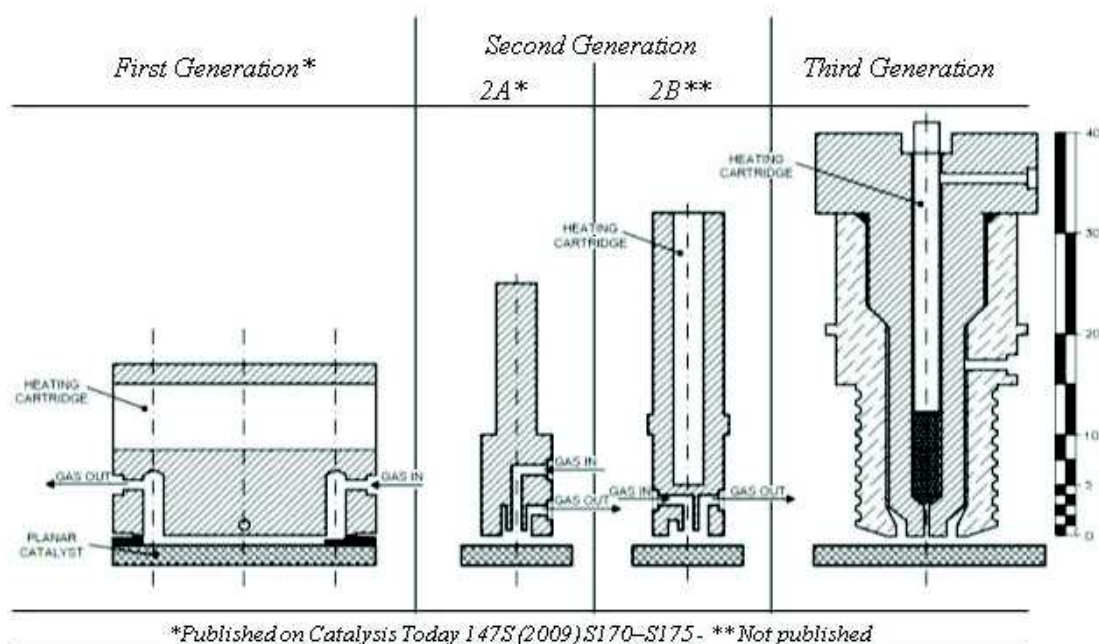
Fig.S2 – Scanning reactor evolution line from first to third generation prototype.

First Generation prototype use a sealing system and allow a step-by-step discrete scanning only. Starting from the second generation we adopt a controlled leakage system in order to allow a continuous true scan. The increase of the overall size of third generation prototype doesn't affect the size of the bottom region with respect the previous generation.
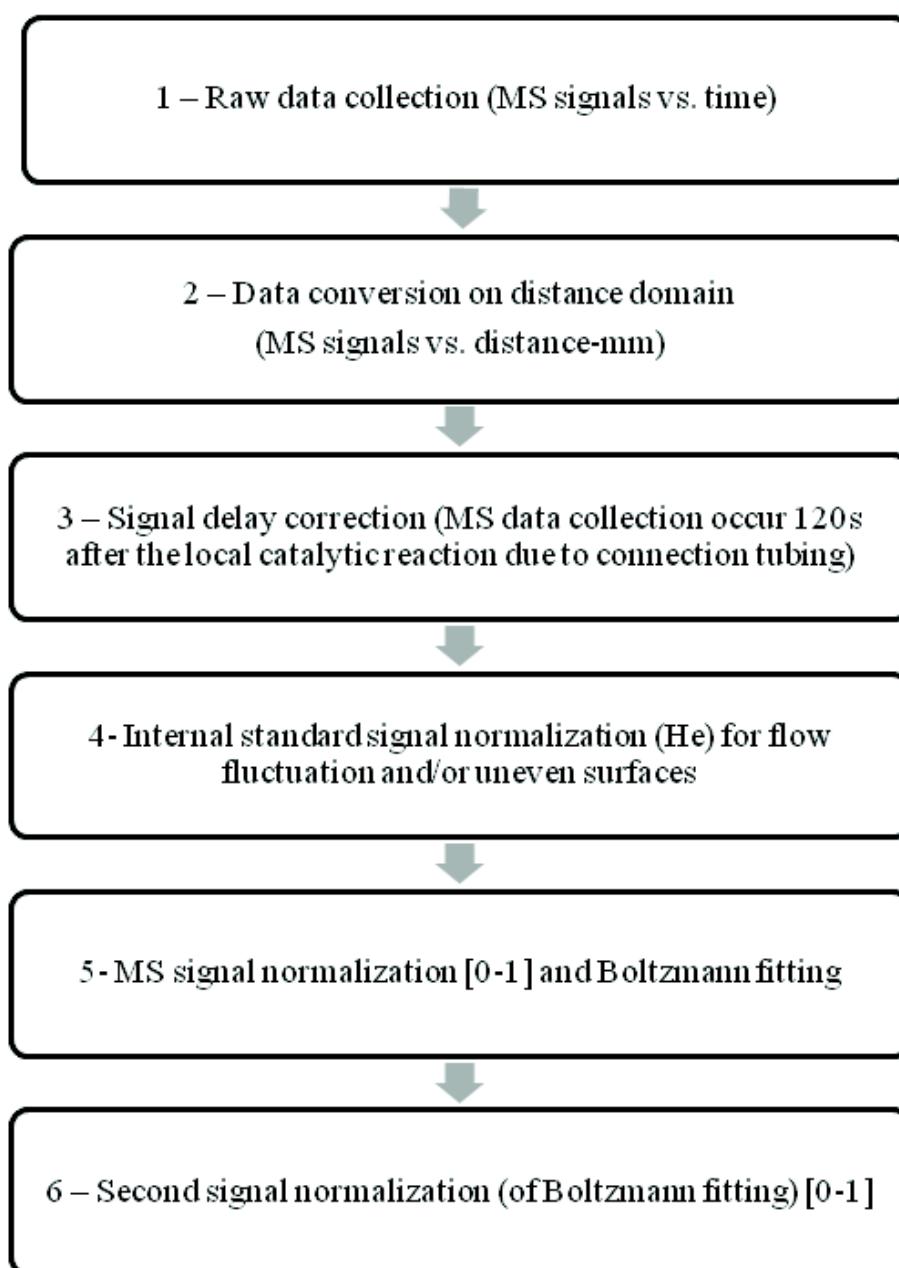
Fig.S3 – Workflow of the data handling in order to compare real data with the scan model.

All the mathematical manipulations were applied sequentially and the output data set of each step is the input for the next one.

| | | 6 mm | | 2 mm | |
|---|---|---|---|---|---|
| | x | active area % | signal | active area % | signal |
| a | 18.5 | 0% | 0 | 0% | 0 |
| b | 19.5 | 4% | 0.04 | 0% | 0 |
| c | 21.2 | 33% | 0.33 | 5% | 0.05 |
| d | 22 | 50% | 0.50 | 50% | 0.5 |
| e | 23 | 71% | 0.71 | 100% | 1 |
| f | 25 | 100% | 1.00 | 100% | 1 |
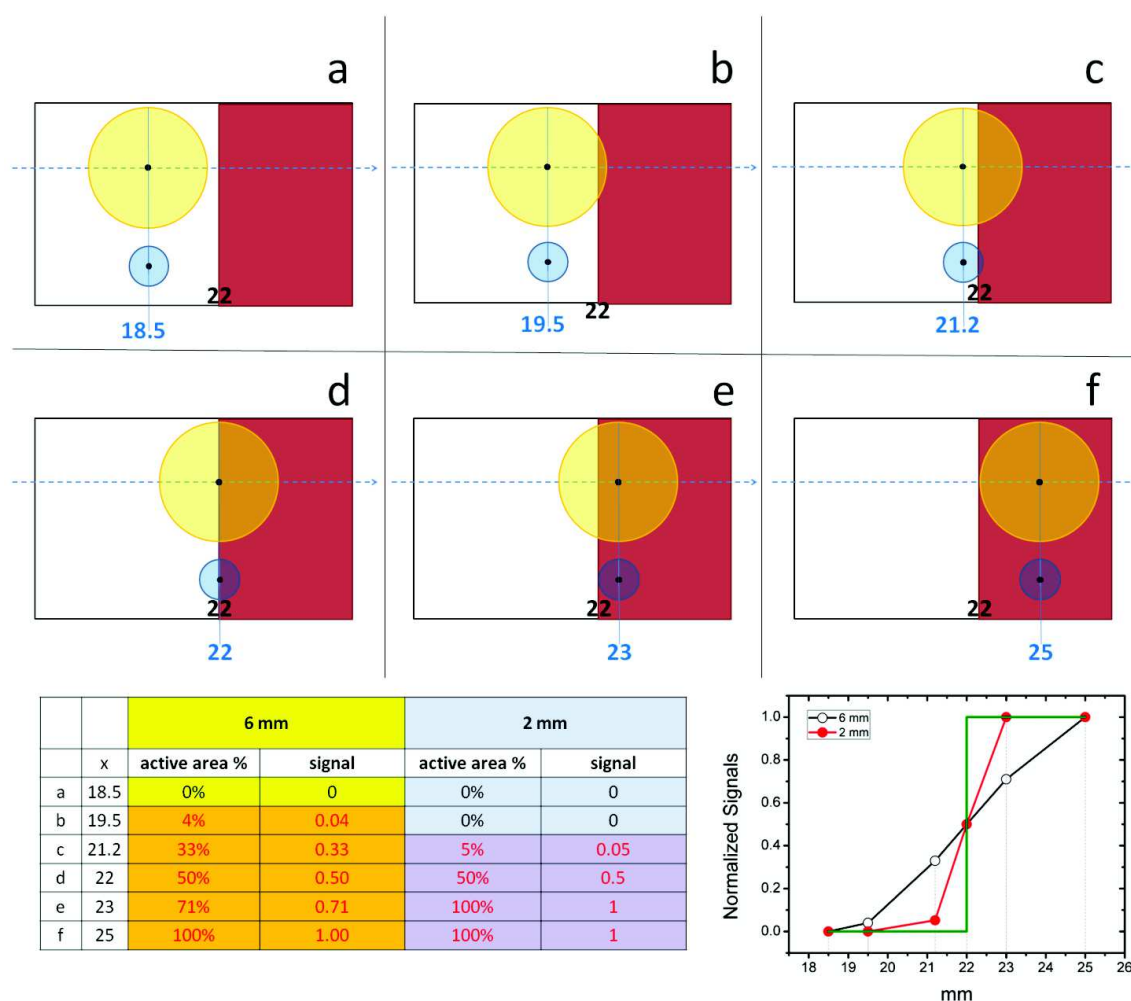
Fig.S4 – Schematic representation of the simple scan model along the scan – top view – with the table of area% to signal correlation and the summary graphs.

The model scan use a simple correlation between the active area below the probe and the normalized signal related with the catalytic activity. When the active area is 0% (Fig.S4a) the signal is zero. At the opposite, when the area is 100% the signal is 1 (Fig.S4f). On the edge between the active and the blank region, the area is 50% and the signal 0.5 (Fig.S4d). On the intermediate positions every fraction of area correspond to a proper signal (Fig.S4b/c/e). Along with the change of diameter's probe, the way of sensing the surface activity change radically: small diameters better describe the change of activity and the

calculated curves have high slopes. Increasing the number of simulated positions the calculated curves smooth to a quasi-sigmoid shape. For the scan model presented in the paper we used a step of 0.2 mm/signal thus 46 points in accord with the scan speed 0,8 mm/min, the MS sampling rate 4 points/mm over  the scan range 17-26 mm.

# Chapter 3

## Planar systems for applications in catalysis and photocatalysis

# 1. Introduction

## 1.1 Introduction to photoelectrochemistry

Energy is the major driving force for the word economy including industry, transport and everyday life (education, health, finance, government, social services, etc. [1]). Non-renewable fossil fuels - oil, natural gas and coal - are currently considered the main source of energy due to their availability, high calorific value, stability, low cost and, furthermore, because they can be easily stored and transported. For many years, the side effects of 150 years of fossil fuel consumption, such as pollution (nitrogen oxides, carbon monoxide, and incompletely burned hydrocarbons) and $CO_2$ production have been disregarded. Starting from the early 1960s, several scientific research programs pointed out the increasing trend in the atmospheric concentrations of $CO_2$, the main greenhouse gas responsible for climate change [2]. It was only in 1979 that a report of the U.S. National Academy of Sciences, after reviewing more sophisticated computer models of the atmosphere, concluded that, if $CO_2$ in the atmosphere continued to increase, "there is no reason to doubt that climate change will result and no reason to believe that these changes will be negligible" (National Research Council 1979, viii). In addition to these scientific findings, the oil crisis in 1973 and the decreasing reserves of fossil fuels raised community awareness on the issue of renewable and more environmentally friendly energy supplies such as wind, hydro, solar, geothermal, and biomass energies (Figure 1.1). In particular, solar supply is considered the major renewable source, and is expected to prevail over the fossil fuels in the future scenarios. Sunlight is an inexpensive, non-polluting, abundant and endlessly renewable source of clean energy. The amount of annual solar energy striking the Earth is approximately ten thousand times the total energy consumed on this planet [3], so converting solar energy into an easily usable form has attracted considerable interest in the last several decades. One of the many research fields that shows promise for solar energy conversion is photoelectrochemistry. Solar energy could potentially be used to provide (i) direct electrical power output (the device called electrochemical photovoltaic cell or regenerative cell) and (ii) chemical products

through a chemical change in the electrode or electrolyte. One of the more attractive chemical reactions is the decomposition of water to form $H_2$ and $O_2$ (photoelectrolysis or water splitting) and this is nothing more than the conversion of photon energy to chemically stored energy in the form of hydrogen.
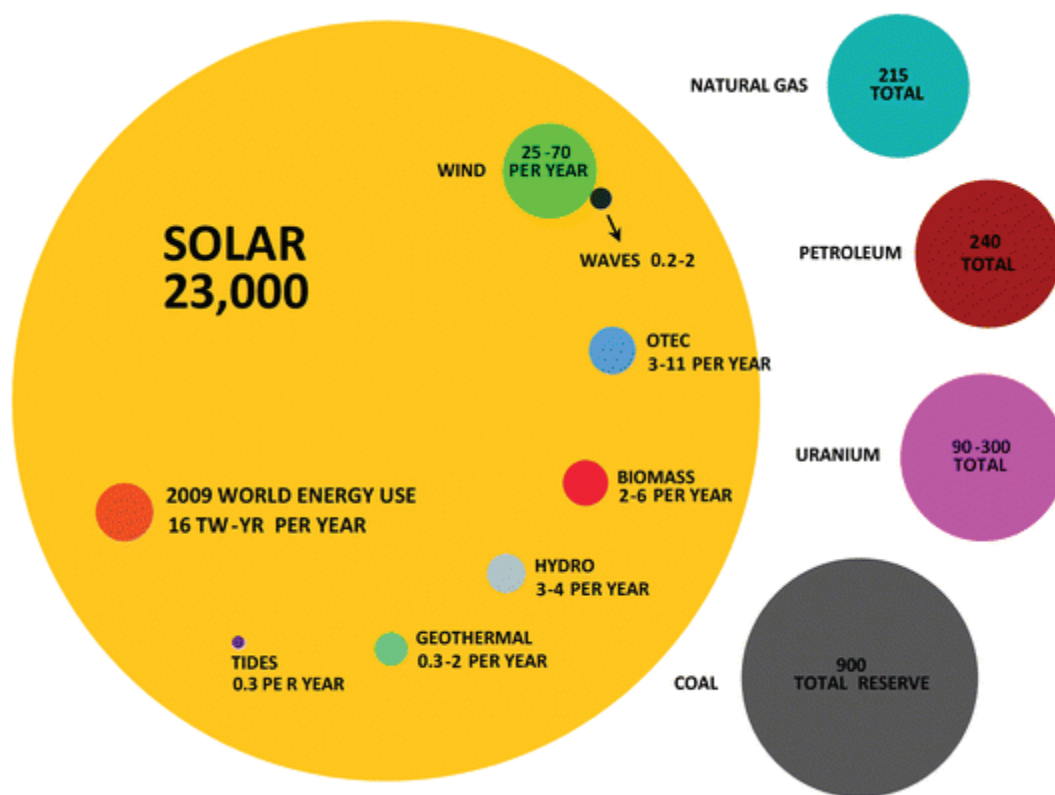


**Figure 1.1.** Comparing finite and renewable planetary energy reserves (Terawatt-years). Total recoverable reserves are shown for the finite resources. Yearly potential is shown for the renewable [4].

## 1.2 Historical background of semiconductor water splitting

The discovery of photoelectrochemical phenomenon is due to a french scientist, Edmund Becquerel [5], who demonstrated in 1839 that a voltage and an electric current are produced when a silver chloride electrode, immersed in an electrolytic solution and connected to a counter electrode, is illuminated. He found that certain materials would produce small amounts of electric current when exposed to light. The origin of this phenomenon was understood only in 1954 thanks to the pioneering work of Brattain & Garrett [6, 7] who launched the modern era of photoelectrochemistry. These pioneering workers showed how chemical reactions, occurring at the surface of germanium semiconductor electrodes, could be influenced by controlling the semiconducting properties of the germanium electrode, as well as by exposing the electrode to light. It became apparent that the Becquerel effect resulted from the presence of a semiconductor at the solid-electrolyte interface and, in particular, to the establishment of a semiconductor-electrolyte junction at the interface.

The works on the photoelectrochemistry of germanium prior to 1970 was of a rather fundamental nature, and was followed by further studies on other semiconductor electrodes such as Si, CdS, ZnS, CdSe, ZnSe, ZnTe, GaAs, GaP, ZnO, SrTiO$_3$, and TiO$_2$. In general, these fundamental studies established the basic characteristics of the semiconductor-electrolyte junction. Of particular importance has been the work of Gerischer [8] who characterized the "kinetics and energetics of electron transfer across semiconductor-electrolyte junctions and the nature of the space charge layer in the semiconductor adjacent to the semiconductor-electrolyte interface" [9].

It was Honda and co-workers [10] in 1972 who first pointed out the potential application of photoelectrochemical systems for solar energy conversion and storage. In their work the n-type TiO$_2$ electrode was irradiated by UV illumination and as result, oxygen evolution (water oxidation) occurred at the semiconductor photoelectrode. Concomitant reduction led to hydrogen evolution at the platinum black electrode (Figure 1.2).
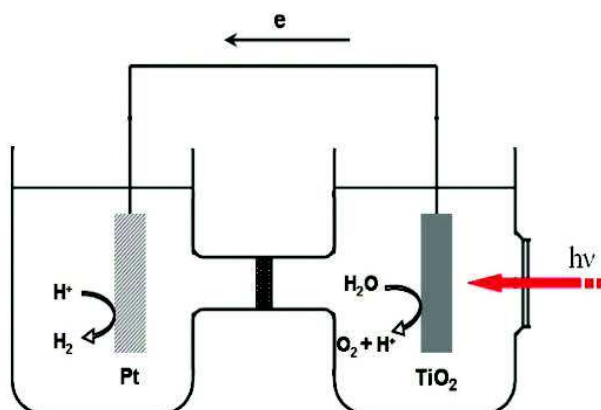
**Figure 1.2.** Schematic representation of a photoelectrochemical cell.

Since the discovery of hydrogen evolution through the photoelectrochemical splitting of water, the use of solar energy coupled with the technology of semiconductor-based photocatalytic water splitting for producing hydrogen has been considered as one of the most important approaches to solving the world energy crisis. Hence, considerable efforts directed towards the development of the necessary semiconductor materials. Over the past 40 years, a wide range of photocatalysts have been developed for splitting water into a stoichiometric mixture of $H_2$ and $O_2$ (2:1 by molar ratio) in the ultraviolet (UV) light region. Xiaobo et al. provided a huge list of papers dealing with this topic [11, Table UV-Light-Active Photocatalysts for Water Splitting to Hydrogen and/or Oxygen], classifying these UV-active photocatalysts in four groups based on their electronic configuration properties:

I. $d^0$ metal ($Ti^{4+}$, $Zr^{4+}$, $Nb^{5+}$, $Ta^{5+}$, $W^{6+}$, $Mo^{6+}$) oxide photocatalysts
II. $d^{10}$ metal ($In^{3+}$, $Ga^{3+}$, $Ge^{4+}$, $Sn^{4+}$, $Sb^{5+}$) oxide photocatalysts
III. $f^0$ metal ($Ce^{4+}$) oxide photocatalysts
IV. small group of nonoxide photocatalysts

However, these oxide photocatalysts are active only under UV irradiation. With respect to the solar spectrum, only a small fraction (ca. 5%) of the incoming solar energy lies in the ultraviolet region, whereas the visible light in the solar spectrum is far more abundant (ca. 43%) [12]. It is necessary to harvest visible light for effective solar-to-hydrogen conversion because UV light accounts for only a small portion of solar energy.
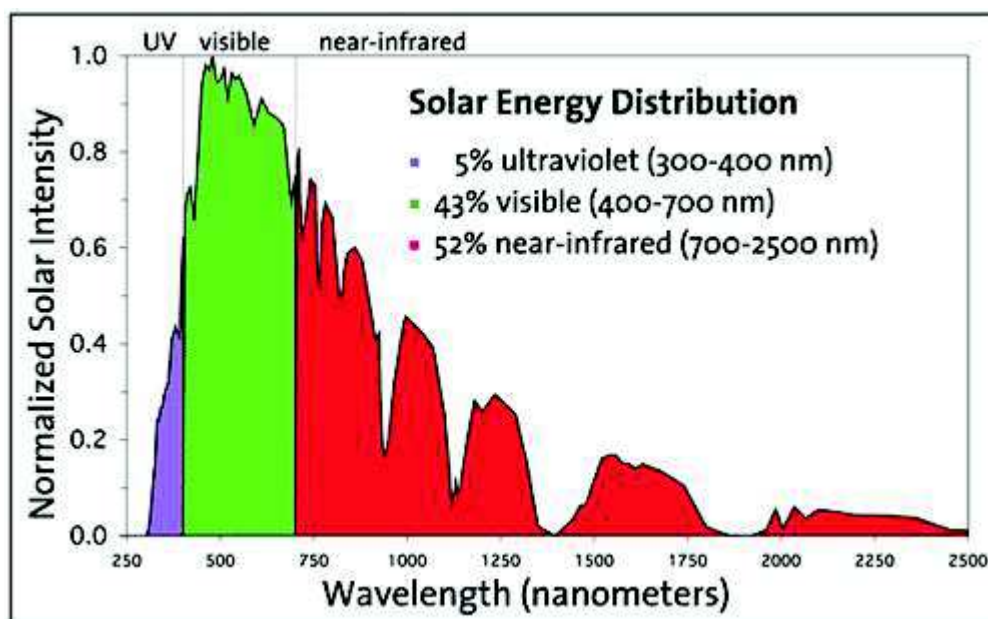


**Figure 1.3.** The spectrum of solar radiation [12].

It is essential, therefore, as an alternative to UV-active photocatalysts to develop visible-light-driven photocatalysts that are stable and highly efficient for the practical, large-scale production of hydrogen using solar energy. Over the recent years, continuing breakthroughs have been made in the development of novel visible-light-driven photocatalysts, leading to the enhancement of photocatalytic activity for water splitting and inspiring great enthusiasm. Therefore, research of effective photoelectrodes for water splitting using new materials for both anodic–cathodic processes should focus on the goal of realizing an efficient photoelectrochemical cell that can simultaneously drive both the hydrogen generation and water oxidation reaction under visible light radiation.

## 1.3 Basic principles of water splitting

When a semiconductor photoelectrode absorbs photons - with energies higher than its band gap energy - from sunlight (UV and/or Vis), the electrons of the valence band of the photocatalyst are excited into the conduction band, while the holes remain in the valence band. This whole process is called the "generation of electron ($e^-$) – hole ($h^+$) pairs". The second step, after photoexcitation, consists of the separation and migration of the charges to the surface of photocatalyst. Here, the photogenerated electrons act as reducing agent to produce $H_2$ and holes can drive the oxidation reaction of water to $O_2$. A schematic representation of the photocatalytic water splitting is depicted in Figure 1.4.
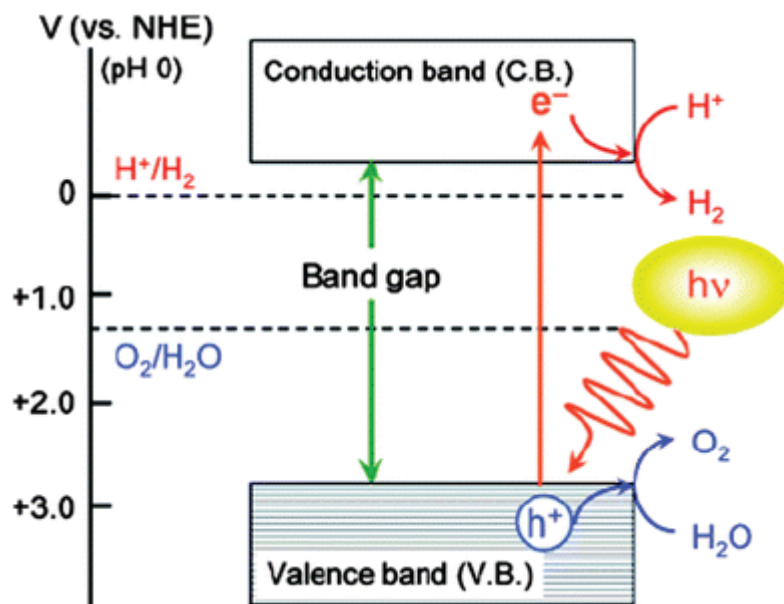


**Figure 1.4.** Basic principles of semiconductor-based water splitting for hydrogen generation.

Thermodynamically, from the viewpoint of Gibbs free energy change, water splitting in $H_2$ and $O_2$ is an uphill reaction with a large positive change in $\Delta G$ = 237.2 kJ/mol, which corresponds to a electrolysis cell voltage ($\Delta E_0$) of 1.23 V per electron transferred.

$$H_2O \rightarrow \frac{1}{2}O_2 + H_2; \quad \Delta G = +237 kJ/mol$$
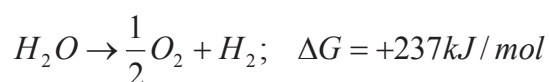
Therefore, to achieve water splitting the theoretical band gap energy ($E_g$) of the photocatalyst should be >1.23 eV that corresponds to light of about 1000 nm:

$$E_g(eV) = \frac{1240}{\lambda(nm)} \quad , \quad \text{where } \lambda \text{ is the absorbance wavelength.}$$

However, the band gap of a visible-light-driven photocatalyst should be narrower than 3.0 eV ($\lambda$ >400 nm). Another thermodynamic requirement for water splitting is the band level requirement: the potentials of the conduction and valence bands. As reported on Figure 1.4, the bottom level of the conduction band must be located at a more negative potential than the redox potential of $H^+/H_2$ (0 V vs. NHE), whereas the top level of the valence band be more positive than the redox potential of $O_2/H_2O$ (1.23 V).

## 1.4 Photoelectrochemical water splitting processes

The processes in the photocatalytic generation of hydrogen are illustrated in Figure 1.5 and can be reassumed in six steps:

1. light absorption of the semiconductor photocatalyst
2. generation and separation of excited charges
3. bulk recombination of electrons and holes
4. migration of the charges
5. surface recombination of electrons and holes
6. surface redox chemical reactions
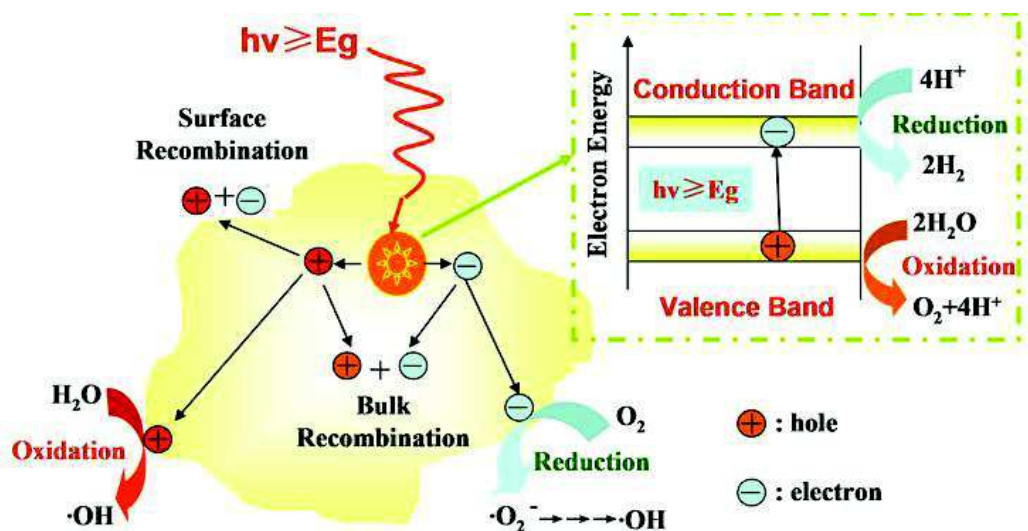
**Figure 1.5.** Processes in photocatalytic water splitting [13].

For successful $H_2$ and $O_2$ evolution the charge separation in photocatalyst and the redox reactions on their surface must proceed within the lifetimes of photoexcited carriers and step 3 and step 5 should be avoided in order to raise the efficiency of photoelectrochemical conversion of solar energy.

Taking into consideration of the above mentioned mechanism and processes, there are some key aspects for developing efficient photocatalysts for the visible-light-driven water splitting reaction. The semiconductor photocatalyst should first have narrow band gap (1.23 eV < $E_g$ < 3.0 eV) to absorb as much light as possible, and should possess the correct band structure. After excited charges are created in the photocatalyst, electrons and holes should be separated efficiently, limiting in this way the charge recombination which is a competitive processes inside the semiconductor [14]. Both surface and bulk recombination are classified as a deactivation process. After the charge separation process, the photoinduced charge carriers must migrate to the semiconductor surface for hydrogen and/or oxygen evolution at the respective photocatalytic active sites [15].

In addition to these aspects - that are considered fundamentally important to improve efficient visible-light-driven photocatalysts - semiconductor stability in an aqueous

84

environment and cost need to be considered to meet the requirements of practical applications.

High and intensive efforts are being made for seeking the best photo-active materials in recent years but as reported in the paper of Wilkinson (2012) "unfortunately, no single material has yet been found that satisfies all of these requirements, although combinatorial methods have been utilized to quickly search for and optimize materials" [16]. So, research on photocatalyst materials are still important in order to contribute to global energy revolution.

## 1.5 Latest strategies

As discussed in the previous section, many semiconductor materials can be used in photoelectrochemical cells [11, 17, 18], although each of them needs increase of the light absorbance and/or improvement of the charge-carrier transportation. In this regard, nano-materials and their designs offer new opportunities to develop efficient photo-active materials for solar water splitting. Figure 1.6 shows the different approaches to the improvement of photoactivity for water splitting using nanotechnology.
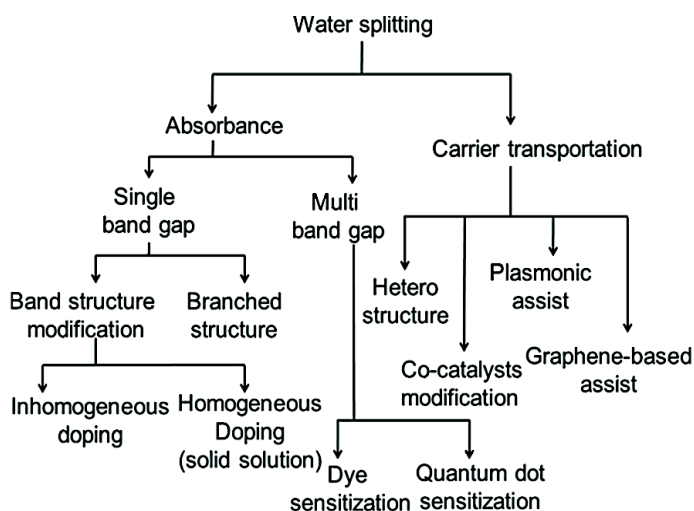


**Figure 1.6.** Schematic of the various strategies for improving the activity of semiconductor electrodes [16].

Metal oxide semiconductors are today the most promising candidates for production solar production of hydrogen by water photoelectrolysis. Accordingly, more recent works [19 and references therein] has focused on developing highly structured oxides for efficient water splitting. The most investigated are:

- Titanium dioxide
- Titanates ($SrTiO_3$, $PbTiO_3$, $BaTi_4O_9$, $M_2Ti_6O_{13}$, M = Na, K, Rb)
- Zirconium oxide
- Tantalum oxide and tantalates
- Niobium oxide and niobates
- Hematite ($\alpha$-$Fe_2O_3$)
- Tungsten oxide

Recently, the last two compounds have gained particular interest for photoelectrochemical water splitting, for the following reasons:

i) on the basis of the aformentioned criteria (previous section), a semiconductor with a bandgap of 2.0 eV is ideal for solar water splitting and this energetic consideration that makes $\alpha$-$Fe_2O_3$ an optimal candidate for solar water splitting (the reported bandgap is 2.0–2.2 eV, allowing visible light absorption up to 550–600 nm) [20]. Hematite is promising for this application due to its significant light absorption and abundance on Earth. Moreover, hematite is nontoxic and stable in aqueous solutions. In contrast, poor transport properties and short minority-carrier lifetimes resulting in minority carrier transport distances [21, 22], restrain the utilization of this material. Such important drawbacks have been intensively addressed in recent investigations. Several recent studies were focused on improving the efficiency of hematite as a photoanode according to the strategies shown in Figure 1.6. Important enhancements were achieved by the Gratzel group by doping or by synthesizing nanostructured hematite films [23] as well as by deposition of an iridium oxide co-catalyst on the surface of $Fe_2O_3$ substrates [24, 25]. Other researchers observed improved oxygen-evolution activity at potentials less than the thermodynamic oxygen evolution potential with cobalt oxide catalyst coupled hematite [26].

ii) Tungsten oxide ($WO_3$) has gained recent interest for photoelectrochemical water splitting [27] because does not suffer from the same unfavorable electronic properties as hematite: in crystalline form it has reasonably long minority carrier lifetimes, isotropic electronic properties and good electron transport properties. A challenge for $WO_3$ remains the indirect band gap, which is about 2.7 eV, and this factor limits the absorption to the blue region of the solar spectrum [18, 20].

In addition to the composite films composition, fabrication methods can significantly influence the photocatalyst properties at the same extent. Generally, it is important to establish good electric contact between semiconductor particles/layers and a conductive substrate [28]. Constant developments in the field of nanomaterials pointed out the advantages of nanostructures for the enhancement of water splitting efficiency [29, 30, 31].

Metal oxide semiconductor materials can be deposited by a wide variety of techniques, and most films can be formed by more than one method. The particular choice of the deposition technique for a given application is determined by the properties of the films desired, the cost or production rate available from the process, temperature limitations of the substrates, uniformity or consistency of the process and its compatibility with preceding and subsequent processing steps [32]. In some cases, thin films deposited in one form are converted to a different form or material in a subsequent processing step, as in the case of crystalline $WO_3$ formation. The widely used deposition procedures are listed in the following table:

| Physical Vapor Deposition (PVD) | Chemical Vapor Deposition (CVD) | Others |
|---|---|---|
| • Evaporation<br>    **Thermal evaporation**<br>    **E-beam evaporation**<br>• Sputtering<br>    **DC sputtering**<br>    **DC Magnetron sputtering**<br>    **RF sputtering**<br>• Reactive PVD | • **Low-Pressure CVD**<br>(LPCVD)<br>• **Plasma-Enhanced CVD**<br>(PECVD)<br>• **Atmosphere-Pressure CVD**<br>(APCVD)<br>• **Metal-Organic CVD**<br>(MOCVD)<br>• **Atomic Layer Deposition**<br>(ALD) | • **Oxidation**<br><br>• **Spin Coating**<br><br>• **Plating**<br><br>• **Sol-gel method** |

**Table1.1:** Commonly used thin film deposition techniques.

Among these procedures, metal-organic chemical vapor deposition has a number of key advantages in depositing metal oxide films for semiconductor applications. These advantages include (i) the strong adhesion of the coating to the support, (ii) the high purity of the film, (iii) high deposition rates, (iv) high film uniformity, (v) precise control of the thickness and (vi) and excellent conformal step coverage on support (ability to coat a surface with complex morphology with a layer of uniform thickness) [32, 33].

Other relevant considerations in choosing a method include its technical complexity, the apparatus and its starting material. As regards the CVD techniques, the general requirements of an ideal precursor can be summarized as follows:

- Purity and reactivity: the precursor should be of high purity and decompose cleanly on pyrolysis without decomposition byproducts.

- Volatility: the precursor should have a good volatility and thermal stability during its evaporation and transportation in the gas phase.

- Stability: the precursor should be stable and have a low degree of toxicity for easy to handle and storage.

- Cost: the precursor should be available in consistent quality and quantity at low cost [33].

## 1.6 Aims of this work

Considering the above discussed aspects, photoelectrode based on single-component photo-active materials cannot carry out the required performance in terms of either photocurrent or conversion efficiency to meet the demands of daily life. There are several limitations on their performance which include low absorbance in the visible region, poor charge-carrier transportation, poor collection of photogenerated electrons, and limited chemical stability in an electrolyte under illumination. Recent efforts in the development of systems for photoelectrochemical water splitting demonstrate the need for further investigations.

In this study, tungsten oxide films have been investigated as photoelectrochemical materials. Firstly, a new device was developed for high resolution and steering CVD deposition of tungsten oxide on different substrates. Starting from the Scanning Planar Catalytic Reactor developed in the Analytic Chemistry Unit of this Department, whose increasing efficiency was demonstrated from prototype n°1 to n°2 [34] and n°3 for continuous screening of catalytic activities [see Chapter 2], our idea was to transform this instrument in a CVD reactor by bringing few changes into the system. It's worth to note that this device works either as Scanning Planar Catalytic Reactor or CVD reactor depending on few changes of the probe. The features of this instrument were tested by performing $WO_3$ film depositions. Secondly, composite films were characterized using XRD, UV-Vis and SEM/EDX techniques. Model based on proper spherical harmonics function aimed at understanding the behavior of CVD process and how the substrates affect orientation of crystalline $WO_3$ films.

Last, photoelectrochemical properties of $WO_3$ films on appropriate supports were tested in order to contribute to the recent intense research of visible-light effective photoelectrodes for water splitting using new composite materials.

# 2. The CVD reactor

## 2.1 The CVD reactor project

In recent years the research of our group was focused on developing new devices for testing the catalytic activity of planar catalysts, as described in the introduction section. Following the implementation of some prototypes [34], a new quite sophisticate reactor system was assembled [see Chapter 2]. The CVD apparatus concept grew out of the last prototype (n°3) in-flow scanning reactor exploiting the already developed rarefied motorized and software controlled sample holder, incoming and outgoing gas flow control and gas sampling and analyzing system (quadrupole mass spectrometer), as depicted in Figure 2.1. Improvements were developed only for the inner component of the reactor probe (1a), and are described in more details in the next paragraph.
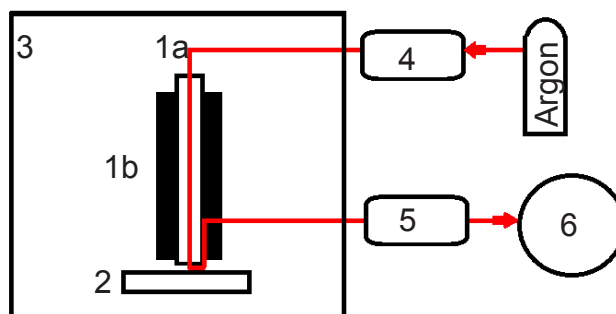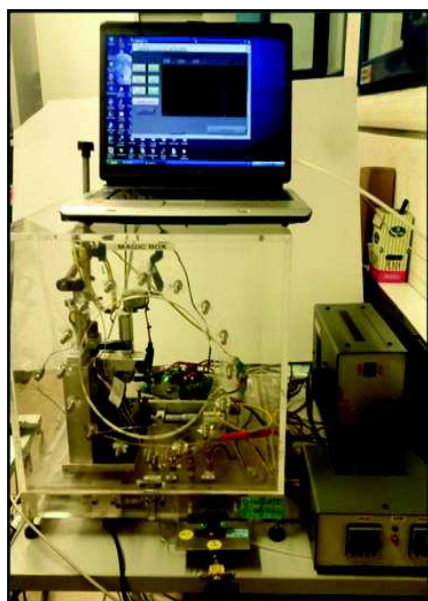


**Figure 2.1.** Picture (left) and schematic description (right) of the CVD reactor: (1a and 1b) two-piece steel reactor probe, (2) heated aluminum sample holder, (3) sealed PMMA box, (4) gas mass flow controller (IN) and (5) flow meter system (OUT), (6) downstream MS detection apparatus.

In the new arrangement of CVD reactor, a glass cartridge (precursor holder) is inserted in the central inner cavity of the deposition probe, which consists of a 50 mm long and 6 mm diameter tube, bottom closed by a porous frit (see Figure 2.2). The temperature can be set to the sublimation temperature of the precursor by a wire heater rolled up around the outer steel body and a needle thermocouple placed at the bottom of the cartridge. We gained two important advantages from this improvement: first of all, the external heating guarantees a decreasing temperature gradient from the outer cylinder wall to the cartridge which is crucial for preventing unwanted condensation. Secondly, in this way it is possible to ensure a fine heating control, given that the thermocouple is in contact with the volatile precursor. The carrier gas (argon) flows from the top of the probe and drives the sublimated precursor below on the heated target, where is thermally decomposed at higher temperatures.
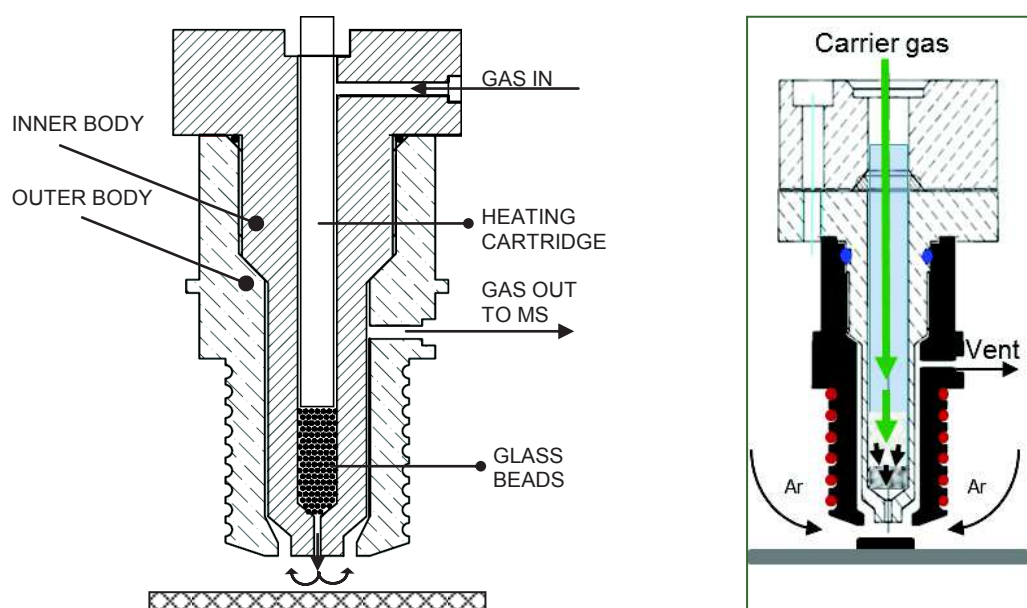


**Figure 2.2.** Overall scheme of third generation reactor probe (left) and overall scheme of CVD reactor probe (right).

The controlled leakage system, that forms an insulating mask beneath the probe, force the precursor to impact on a restricted and tunable region. Therefore the CVD occurs on a selected area only, tuned by the probe/substrate distance and/or by the outlet flow-rate of the leakage system. The by-products of the reaction - including the decomposed precursor and the possible unreacted precursor itself - are driven away by the leakage system and sampled by a quadrupolar mass spectrometer to monitor the CVD process.

The deposition probe is fixed over a movable sample holder mounted on motorized stage. The scanning system is driven by a user made software in 3D (XYZ) directions to tune the probe-target distance and to set the deposition pattern requested. In Figure 2.3 is reported the interface window of the software by which is possible to set the initial point (ACTUAL), the final point (MOVE TO) and the speed (X speed, Y speed, Z speed) of movements in all three directions permitting to easily set, for example a zig zag track (Figure 2.4) and to produce exactly the same deposition result.
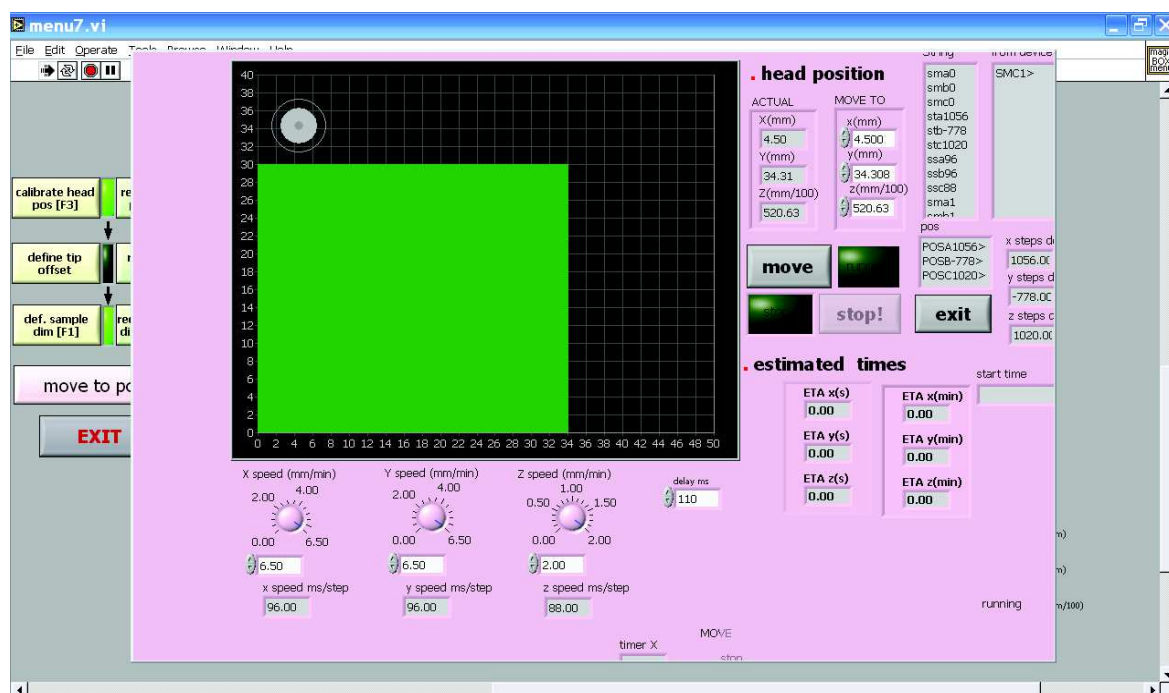


**Figure 2.3.** Interface window of the user-made software based on LabVIEW platform.
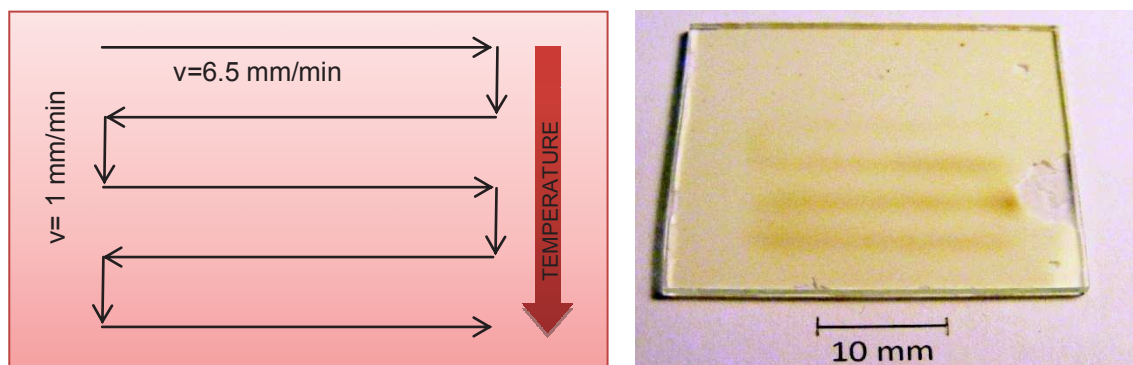
**Figure 2.4.** Scheme of the programmed track (left) and the obtained deposition pattern of $WO_3$ on TLC plate (right).

## 2.2 Experimental details of $WO_3$ deposition

Deposition of the tungsten oxide film was performed using commercially available $W(CO)_6$ (Aldrich) as precursor and argon as carrier gas. The deposition was carried out both in air as well as in inert (argon) atmosphere. The inlet and outlet flow were set by the mass flow controller to 0.8 ml/min and 3.5 ml/min respectively. The distance between the probe and the support ranged from 0.1 mm to 0.8 mm. Several different supports were tested as target, such as silica gel-glass TLC commercial plates (without fluorescent indicator), microscope slide glass, silicon wafers, FTO (fluorine doped tin oxide, $F:SnO_2$), FTO/hematite and ITO/hematite (tin doped indium oxide) substrates. The TLC plates were used without any pre-treatment whereas the other targets were cleaned by washing them in ultrasonic bath with distilled water, ethanol and acetone, 10 minutes each cycle. Deposition experiments were conducted by heating the horizontal sample holder to the required temperature in the range of 220-250 °C. The supports were pre-heated in situ before the deposition probe to ensure the decomposition of the precursor. The probe was heated to the sublimation temperature of $W(CO)_6$ at 70-75 °C and the substrate was moved according to an established pattern controlled by the computer-driven stepping motors. During the preliminary depositions we monitored the mass channel 28 amu (carbon monoxide), inasmuch as carbonyl ligand is the unique decomposition product. At

the end of the deposition the argon line was closed and the targets were allowed to cool down to 100 °C. Details pertaining differences of the deposition parameters among the five mentioned supports will be provided in the related sections.

## 2.3 Investigation on the CVD reactor performance

Chemical vapor deposition techniques are widely employed for the deposition of thin films because they offer the potential for good film uniformity and composition control, large area growth and excellent step coverage [35]. The choice of key process parameters such as substrate morphology, and temperature, deposition time, precursor flow and co-reactant gas flow can affect a wide variety of property of films including the transparency, electrical properties, growth rate, texture and morphology [36,37].

To test the efficiency and the performance of the CVD reactor a well-known, simply but attractive process, the $WO_3$ deposition from $W(CO)_6$ on various surfaces was studied. Silica gel-glass TLC commercial plate (without fluorescent indicator) was chosen as porous support since it is a very economic and easily attainable material. In order to investigate in more details flat surfaces, two different samples, microscopy glass plates and monocrystalline silicon wafers were used as supports for the deposition experiments. Originally this experimental work was conducted in order to explore the versatility of the new CVD reactor but also revealed crucial to ascertain flaws of the initial project. Result of this investigations will be described in this paragraph.

## 2.3.1 Effect of surface on the deposition result

Consistently with literature reports, chemical vapor deposition has the ability to grow films on surfaces of complex topography as well as on smooth, flat surfaces. The CVD process - being a typical bottom-up approach – begins with individual molecules that are able to penetrate in depth of a porous structure such as silica gel-glass TLC plates. The decomposition takes place inside the pores resulting in a quite narrow deposition pattern (see Figure 2.5 and Figure 2.7). The spatial gap between the substrate and the probe ($\Delta z$) has an important influence on the width of the $WO_3$ coating; the controlled leakage system is able to force the precursor to impact on a restricted area (deposition spot diameter < 0.5 mm) at smaller distances ($\Delta z$ = order of magnitude of tens of micrometer), on larger area at larger distance.

On the contrary, the deposition result is rather different on flat substrates because the active surface for decomposition is definitely lower and no penetration is possible. The obtained tungsten oxide layer with uniform thickness covers homogeneously a large (~3 mm width) area (Figure. 2.5) and this result was not influenced in a significant manner by the probe - support distance.
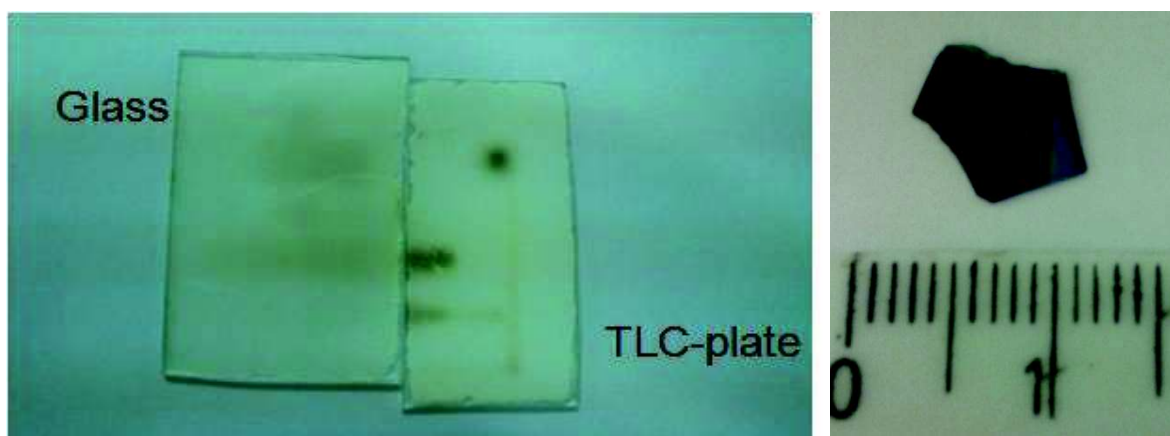


**Figure 2.5.** Pictures of $WO_3$ deposition on silica gel-glass TLC commercial plate, on simply glass pieces (left) and on monocrystalline silicon wafer (right).

Aiming to highlight how the surface features influence the deposition patterns, scanning electron microscopic studies were performed. Observing Figure 2.6 and Figure 2.7, it may be noticed that this home-made CVD reactor has the ability to deposit $WO_3$ films of uniform thickness on flat surfaces as well as on samples with complex morphology.
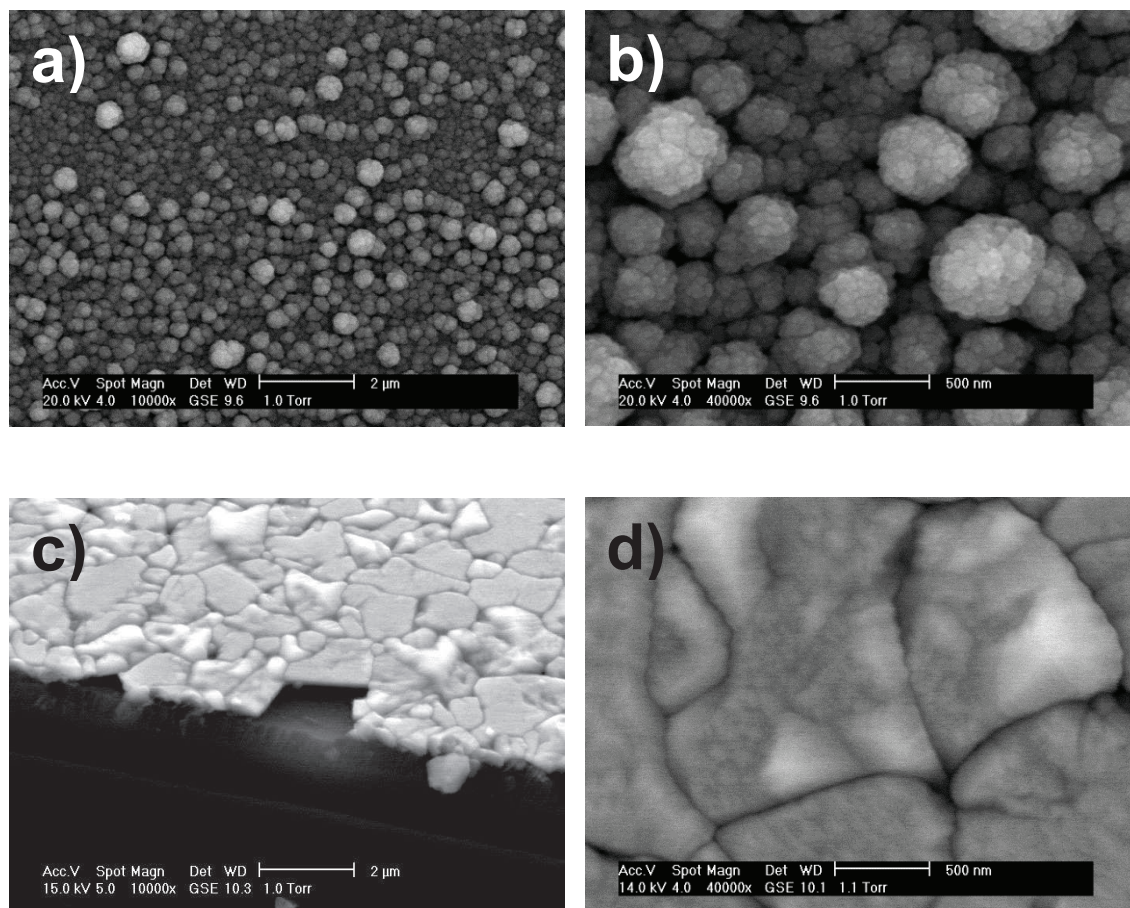


**Figure 2.6.** SEM micrographs at different magnifications of $WO_3$ film on Si wafer supports; a) amorphous $WO_3$, top view at 10 kX magnification, b) amorphous $WO_3$, top view at 40 kX magnification, c) crystalline $WO_3$, cross section (45°) image at 10 kX magnification, d) crystalline $WO_3$, top view at 40 kX magnification.
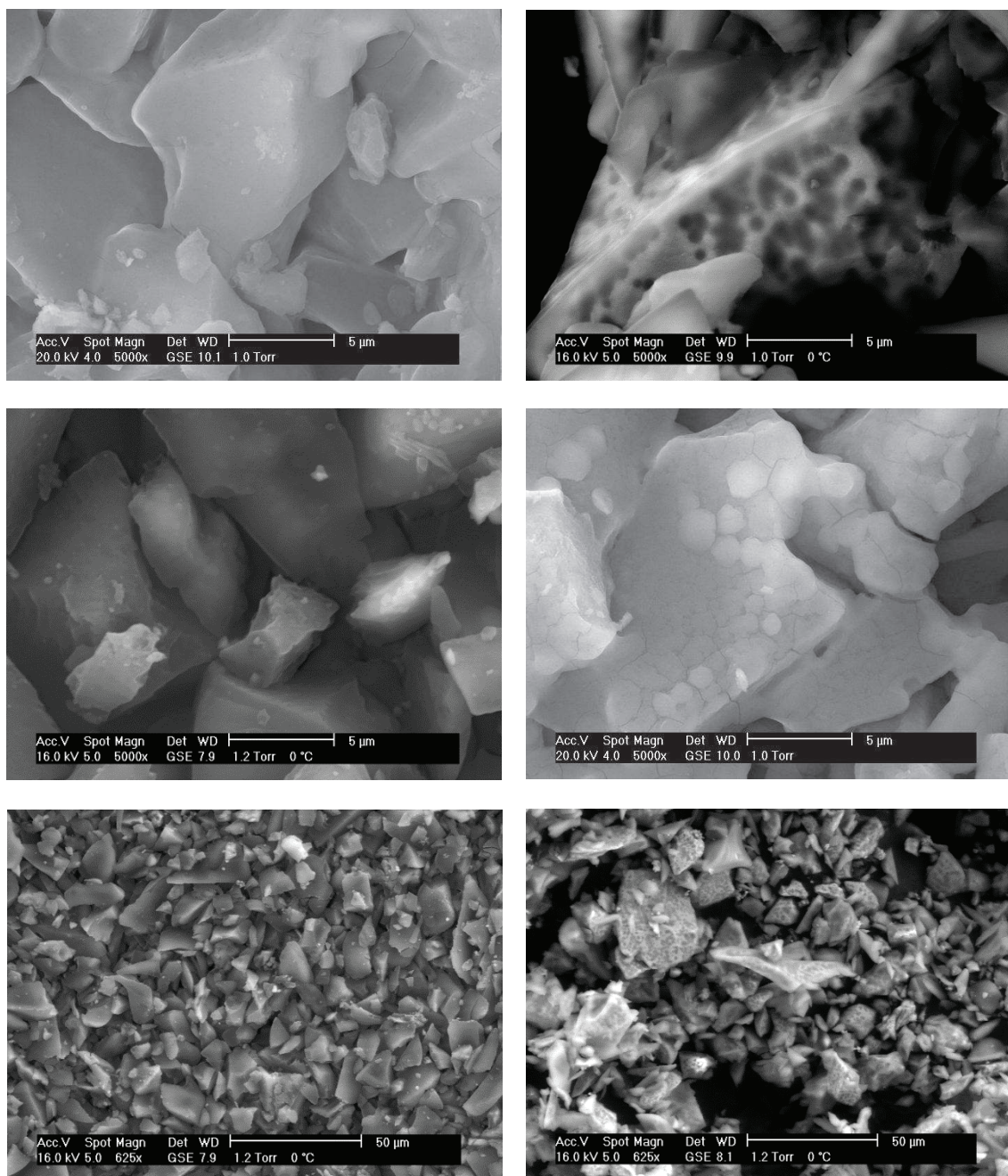
**Figure 2.7.** SEM micrographs at different magnifications of a typical silica gel-glass TLC commercial plate before (left) and after (right) $WO_3$ deposition.

## 2.3.2 Effect of surface on the decomposition temperature

The choice of experimental parameters, substrate temperature in particular, may affect the growth rate, texture and morphology of the coatings. MOCVD requires a minimum deposition temperature that depends not only on the precursor but also on experimental conditions. As regards the above illustrated samples, the $WO_3$ films were obtained with substrate temperatures at 220°C on TLC and only at 250 °C on glass substrates. This result highlights that the decomposition temperature of the $W(CO)_6$ precursor is surface dependent and is a little higher on flat than on porous surfaces. As an example, decomposition temperature may play a major role, especially when the support is not flat and shows a high roughness and surface area. The pictures reported below, clearly shows that on hematite a deposition of a flat film of tungsten oxide is obtained if the decomposition temperature is quite high: only working at lower temperature it is possible to gain a perfect coverage of the starting grains.
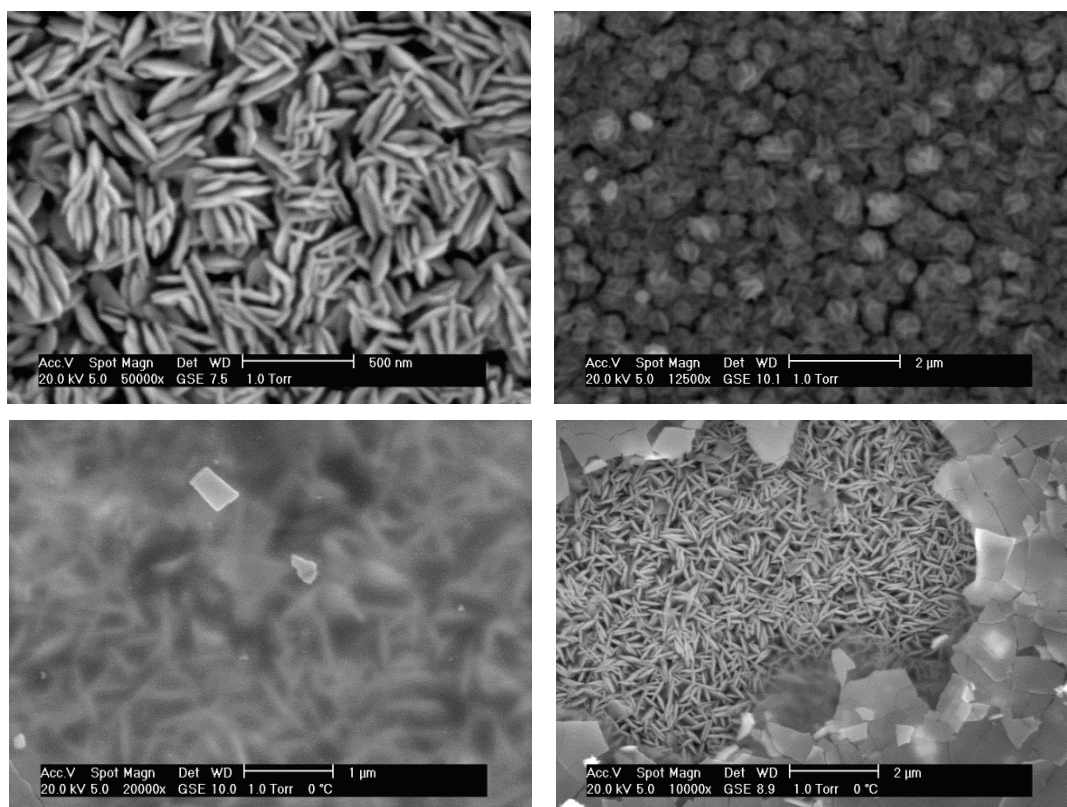


**Figure 2.8.** SEM micrographs of tungsten oxide films on nanostructured α-$Fe_2O_3$ supports at different temperatures: (a), (b) 220 °C; (d), (e) 250 °C.

### 2.3.3 Problems and solutions for non homogeneous deposition

The new CVD reactor, as previously mentioned, was developed starting from a precedent scanning reactor project. Consequently, the set up was calibrated for different performance from those investigated in the present study. In fact, during the preliminary deposition experiments, it emerged that the original heating arrangement was able to guarantee homogeneous heating only at low temperatures, about 100 °C. As regards CVD process, higher temperature range (extended to 200-300 °C) is required for fully decomposing the precursors and the heating has to be homogeneous on all the holder surface in order to obtain a compact and regular deposition. To ensure a uniform distribution of heat on the whole support holder, it was necessary to re-design the heating system. The single heating cartridge of 150 watt (inserted in the middle of the aluminum sample holder) was substituted with four smaller ones (50 watt) (see Figure 2.9) in equally spaced manner. The maximum temperature difference was verified with the help of an external thermocouple and it resulted less than 3-4 °C on all the surface. This change entailed also an increase of the sample holder dimension, that permits to use larger supports (30 x 40 mm) for depositions. Figure 2.10 shows the technical design of the two holder prototypes (side view) and the measured temperature distribution on the surface (top view).



**Figure 2.9.** A picture of the new holder design.
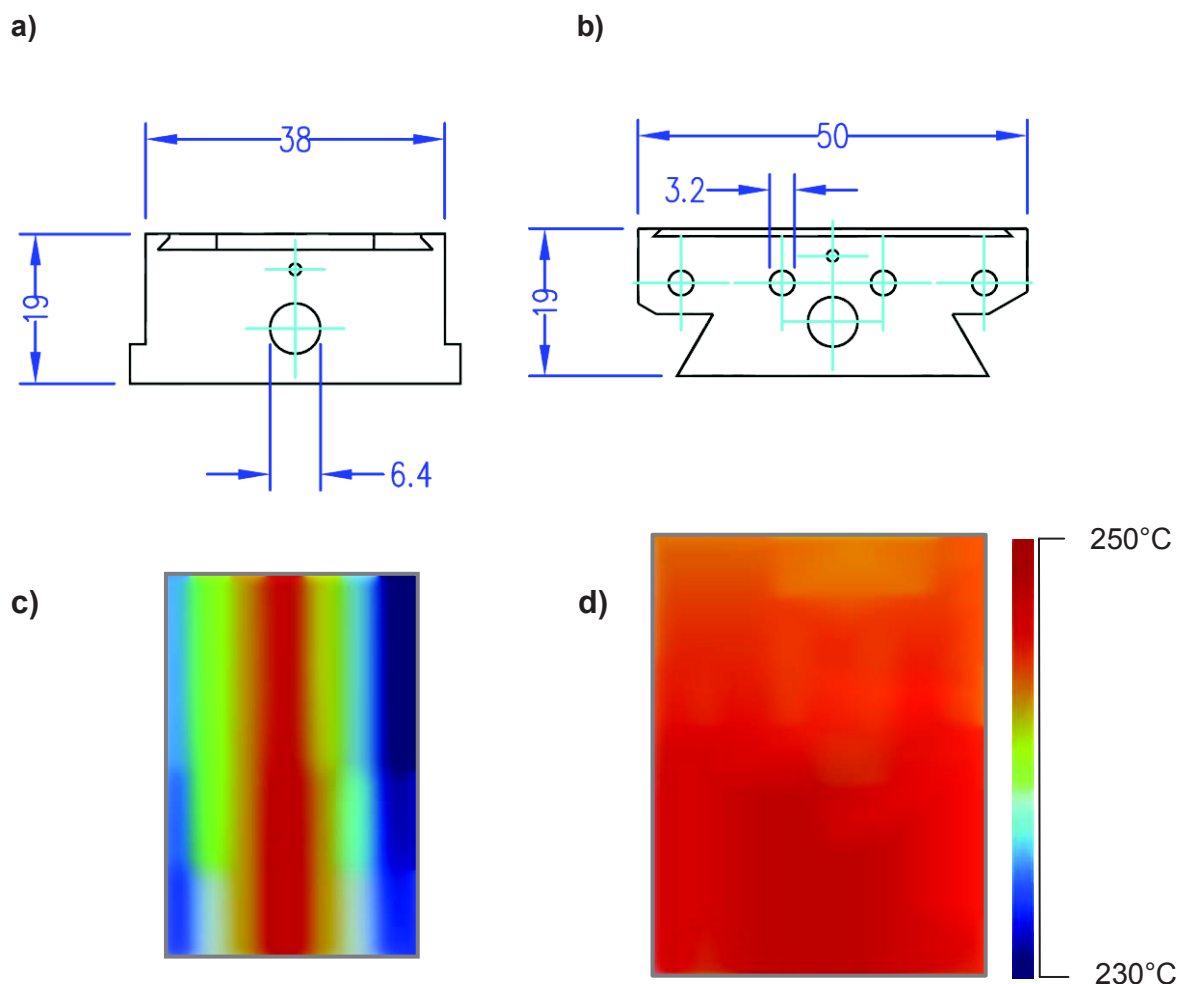
**Figure 2.10.** Side-view technical drawing illustrating the details of the sample holder; a) previous and b) modified model (top). Qualitative illustration of the temperature distribution on the holder surface at 250 °C; c) previous and d) modified model (bottom).

At last, from the results of a number of preliminary experiments, optimal deposition parameters were determined. A critical factor with this chemical vapor deposition technique is in scaling-up for production of real samples for practical applications. This involves not only achieving coating coverage on larger supports but also ensuring uniformity of composition and physical properties on all surfaces. In order to reach this goal, $WO_3$ layers were made by depositing some parallel lines (or scans) on the surface spaced with a certain distance. In the case of simple glass, silicon wafer and conductive

glass samples, this distance is about 3 mm. Smaller distance, obviously results in grid like deposition because of the overlapping deposition lines (Figure 2.11). The other experimental parameter to be optimized was the movement velocity of the holder. Preliminary tests showed that small differences of the sample - probe distance (non perfectly flat support), along with those in temperature throughout the holder may affect the homogeneity of the deposition. For attenuating such drawbacks, we observed that the higher the movement velocity the better the resulting deposition. Thus, instead of one and slow (1.0 mm/min) deposition line, more but fast (6.5 mm/min) *scans* were performed on the support.



**Figure 2.11.** Picture of grid like deposition of $WO_3$ on simple glass sample (left) and homogeneous deposition of $WO_3$ deposition on ITO/hematite support (right).

# 3. Characterization of as-synthesized and annealed WO$_3$ films

## 3.1 Introduction

Bulk tungsten trioxide is a light yellow crystalline powder with a monoclinic structure at room temperature, whereas WO$_3$ nanoparticles exhibit different chemical and physical properties (structural, optical and electrical behaviors) depending on the choice of substrate, deposition techniques and conditions.

According to the literature, amorphous tungsten oxide has often been observed for depositions at low temperatures (< 300 °C), so that for transforming it in crystalline phase, further thermal treatments are necessary. Depending on annealing parameters, tungsten oxide may have different crystalline forms that are shown in Table 3.1 [38, 39].

| Phase structure | | Space group |
|---|---|---|
| monoclinic | $\varepsilon$-WO$_3$ | $Pc$ |
| orthorhombic | $\beta$-WO$_3$ | $Pnma$ |
| triclinic | $\delta$-WO$_3$ | $P$-1 |
| monoclinic | $\gamma$-WO$_3$ | $P2_1/n$ |
| tetragonal | $\alpha$- WO$_3$ | $P_4/ncc$, $P_4/nmm$ |

**Table 3.1** Possible phase structures of WO$_3$ nanoparticles.

Thin tungsten trioxide films can also have many different colors due to oxygen vacancies [40]. A perfect stoichiometric crystalline WO$_3$ thin film is slightly yellowish whereas in a sub-stoichiometric WO$_{3-x}$ film with oxygen vacancies the color can shift to red, purple and then blue and color can also vary with grain size and growth direction of the particles.

According to the above mentioned traits, CVD tungsten oxide films obtained in this work were investigated for better understanding their composition, morphology and crystalline structure. Depending on the analytical method applied, different materials were used as substrates.

## 3.2 Experimental

### 3.2.1 UV-Vis

The UV-Vis absorption measurements of the samples were performed on a Thermo Scientific Evolution 600 spectrometer. The background scan was performed using a blank piece of quartz glass, thus, the UV-Vis spectra obtained show the absorbance of the semiconductor film deposits.

*Sample preparation*

Deposition of the tungsten oxide films was performed on commercial quartz glass supports (Colaver, 20 mm x 20 mm) using $W(CO)_6$ (Aldrich) as precursor and argon as carrier gas. The deposition was carried out both in air and in inert (argon) atmosphere. The inlet and outlet flow were set by the mass flow controller to 0.8 ml/min and 3.5 ml/min respectively. The distance between the probe and the support was 0.3 mm. The targets were cleaned by washing them in ultrasonic bath with distilled water, ethanol and acetone, 10 minutes each cycle. Deposition experiments were conducted at a substrate temperature equal to 250 °C. The probe was heated to 75 °C and the substrate was moved 15 times backwards and forwards along a single straight line. The movement velocity was set to 6.5 mm/min. At the end of the deposition the argon line was closed and the targets were allowed to cool down to 100 °C. After deposition, annealing procedures were performed by heating the coated glass in a laboratory furnace at 500 °C for 3 h.

## 3.2.2 XRD

The crystalline structure was analyzed by X-ray power diffraction (XRPD) on

(i)     Bruker AXS D8 Advance diffractometer, equipped with a linear position-sensitive Lynxeye detector, primary beam Soller slits, and Ni-filtered Cu-Kα radiation ($\lambda$ = 1.5418 Å). Diffraction data were collected with overnight scans, 20-60° 2θ range at room temperature. The generator was set at 40 kV and 40 mA.

(ii)    Rigaku Miniflex using Cu-Kα radiation, 30 kV, 10 mA with a scanning speed of 0.3 deg/min, RT.

*Sample preparation*

Deposition of the tungsten oxide film was performed on commercial quartz glass supports (Colaver, 20 mm x 20 mm), monocrystalline Si wafers and on FTO conductive glasses using $W(CO)_6$ (Aldrich) as precursor and argon as carrier gas. The deposition was carried out both in air. The inlet and outlet flow were set to 0.8 ml/min and 3.5 ml/min respectively. The distance between the probe and the support was 0.3 mm. The targets were cleaned by washing them in ultrasonic bath with distilled water, ethanol and acetone, 10 minutes each cycle. Deposition experiments were conducted at a substrate temperature equal to 250 °C and the probe was heated to 75 °C. In the first set of experiments the substrate was fixed and deposition time was increased from 10 to 80 min (Table 3.2).

| Sample name | Substrate | Deposition time (min) |
|---|---|---|
| W@Q 10 | Amorphous quartz glass | 10 |
| W@Q 20 | Amorphous quartz glass | 20 |
| W@Q 40 | Amorphous quartz glass | 40 |
| W@Q 80 | Amorphous quartz glass | 80 |

**Table 3.2.** List of spot–like $WO_3$ samples.

The second set of samples was obtained by moving the support - with the velocity of 6.5 mm/min - backwards and forwards, covering the whole substrate surface according to a "specified route" (details are reported in Figure 3.1 and Table 3.3). At the end of the deposition the argon line was closed and the targets were allowed to cool down to 100 °C. After deposition annealing procedures were performed by heating the coated glass in a laboratory furnace at 500 °C for 3 h.
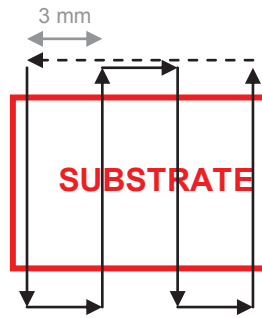


**Figure 3.1.** Scheme of deposition route.

| Sample name | Substrate | N° of deposition cycles (passes) |
|:---:|:---:|:---:|
| W@Si 10 SCAN | Si wafer | 10 |
| W@Si 30 SCAN | Si wafer | 30 |
| W@FTO 4 SCAN (3 replicates) | FTO | 4 |
| W@FTO 10 SCAN (4 replicates) | FTO | 10 |
| W@FTO 30 SCAN (3 replicates) | FTO | 30 |

**Table 3.3.** List of homogeneous $WO_3$ coatings.

### 3.2.3 SEM/EDX

Morphology, composition and thickness of as prepared and annealed $WO_3$ coatings were characterized through a XL30 environmental scanning electron microscopy (ESEM-FEG Philips) integrated with energy-dispersive X-ray (EDX) detector under high vacuum and/or low pressure condition using an accelerating voltage of 20 kV.

*Sample preparation*

The SEM/EDX analysis were performed on the same samples used for the XRD, UV-Vis and photocurrent experiments, the latter reported successively in paragraph 4.

## 3.3 Absorption spectroscopy studies of $WO_3$ films

Optical properties can be characterized by starting with a visual inspection. As shown in Figure 3.2, the as-deposited sample in inert atmosphere has dark grey-blue color, whereas the annealed sample shows the typical light yellow color of crystalline $WO_3$ films. Similarly, for $WO_3$ films prepared in the presence of oxygen we can observe a significant change of color (from dark yellowish brown to light yellow). These observations suggest that, according to literature, phase transformation may be induced by heat treatment.
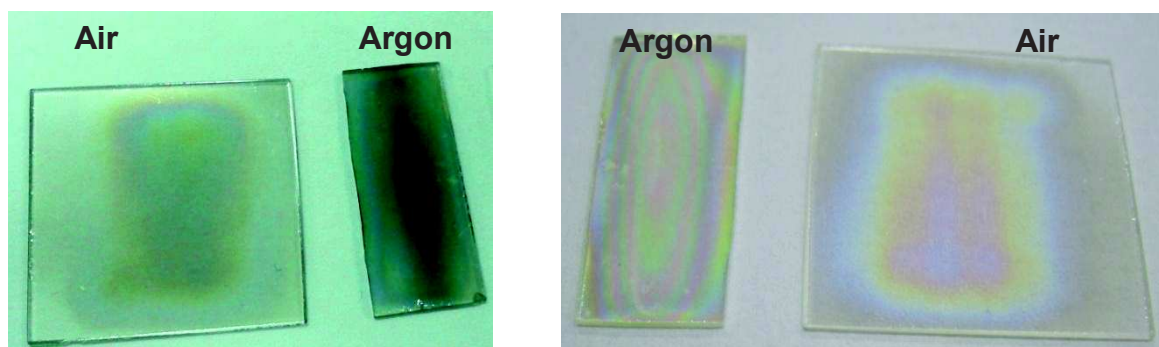


**Figure 3.2.** Pictures of the as-deposited (left) and annealed $WO_3$ film on quartz glass support (right). Within each picture, samples differ depending on deposition atmosphere.

Additional information on composition were obtained by UV-Vis absorption measurements. The obtained spectra were compared to each other and also to

bibliographic references. Results showed the occurrence of $WO_3$ films independently of the deposition ambient and also of post-annealing temperature. As shown in Figure 3.3, the obtained spectra fit with reference one. As reported in various studies, $WO_3$ have the maximum absorbance peak between 200 and 350 nm which is in agreement with the finding in this study. The significant background absorption throughout the 550 to 350 nm range, probably due to some scattering of light at $WO_3$ particles.
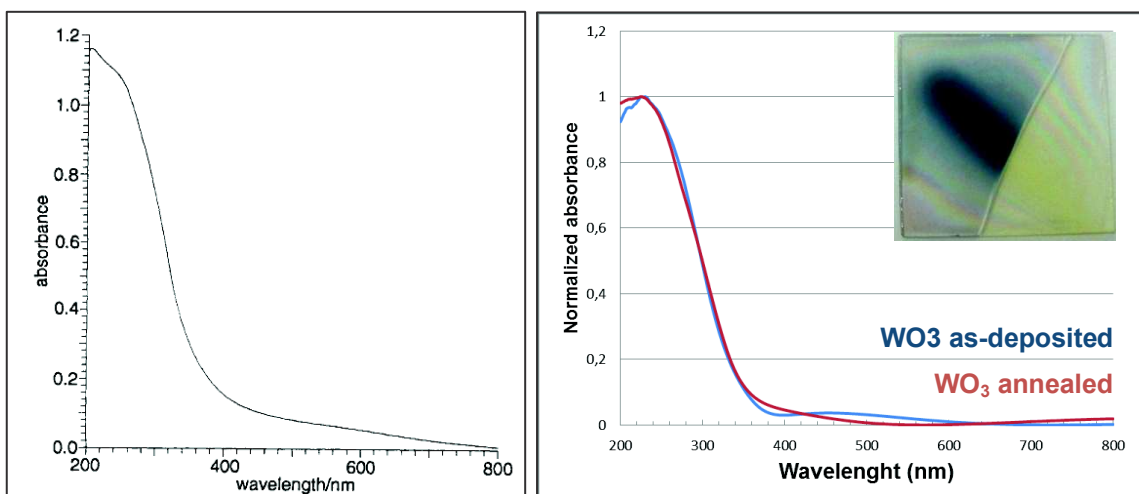


**Figure 3.3.** UV-Vis reference spectrum of a $WO_3$ film annealed at 500 °C for 1h [41] (left) and spectra of the as-deposited and annealed $WO_3$ films (red: as-deposited; blue: annealed). The inset shows a picture of the two contiguous samples. Lines refer to the solely inert-atmosphere depositions for illustrative purpose only.

In conclusion, even in inert atmosphere condition tungsten oxide occurs because of the trace presence of oxygen in the argon flow transporting the $W(CO)_6$ precursor. The significant change of coating color is probably due to the phase transformations of $WO_3$ from amorphous to crystalline. To test this hypothesis, XRD studies were performed.

## 3.4 XRD studies of WO$_3$ Films

One of the most important techniques used to characterize the structure of crystalline films is X-ray powder diffraction (XRPD). It can be used to identify crystalline phases, preferred orientation of the crystalline domains and to determine grain sizes.

First, thin WO$_3$ film depositions on quartz glass supports were useful to perform preliminary investigations in order to check the phase composition of as-deposited and annealed films. Figure 3.4 shows the XRD spectra indicating that as-deposited WO$_3$ film is amorphous and exhibits a broad hump and no sharp peaks in its X-ray diffraction spectra. According to the literature, crystallization occurs only after thermal treatment at high temperatures: evidence for crystalline phase formation was obtained for the annealed sample. On one hand, the collected XRD data was not of sufficient resolution to identify the crystallographic phase; on the other hand the broad diffraction background on the XRD pattern in general can be attributed to the amorphous substrate material as well as to residual amorphous oxide in the sample.
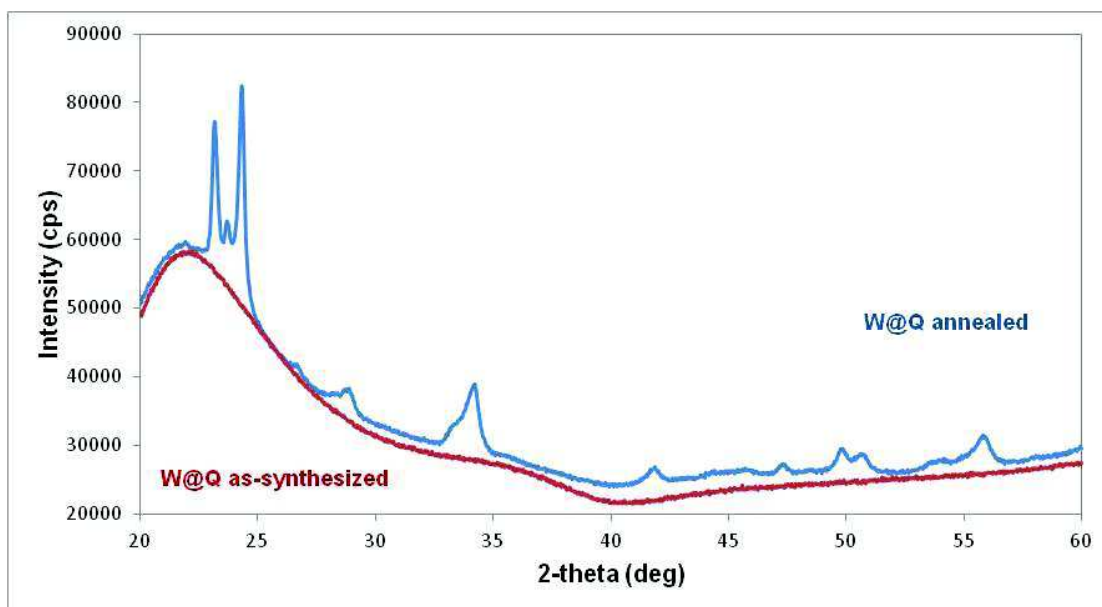


**Figure 3.4.** XRD spectra of the as-deposited (red) and annealed WO$_3$ films (blue) on amorphous quartz glass substrates.

To address these issues, two different experiments were performed. First, samples grown on monocrystalline Si wafer substrates were studied. The XRD spectrum is illustrated on Figure 3.5; the fine diffraction lines and the lack of background clearly show that $WO_3$ phase is very well crystallized.
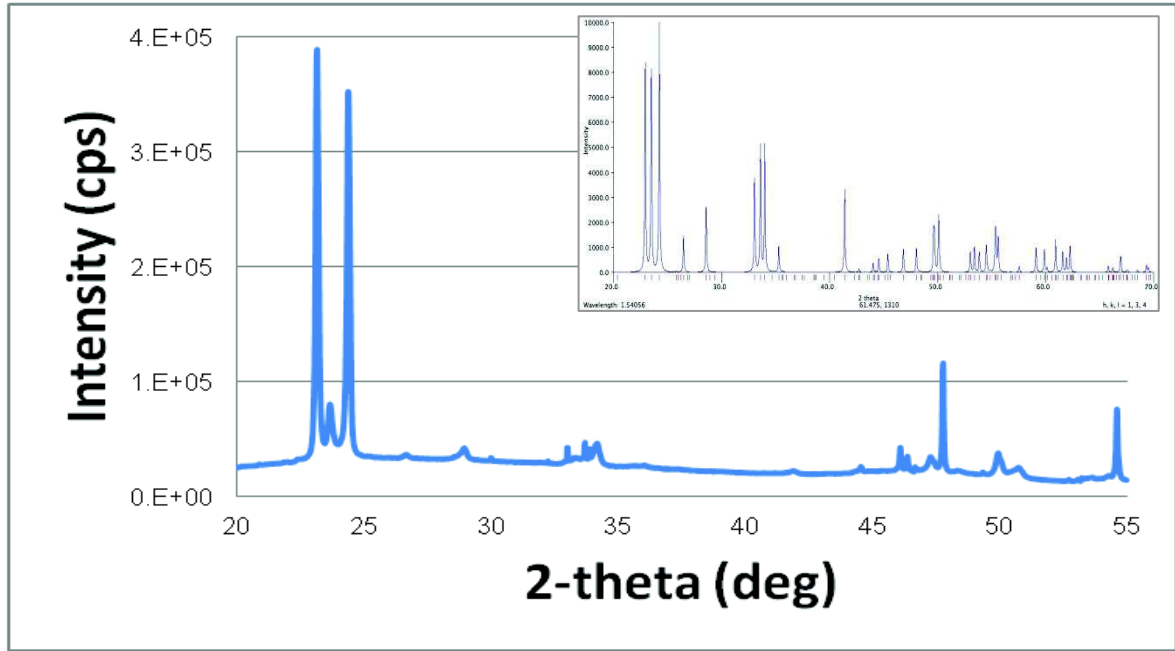


**Figure 3.5.** XRD spectrum of an annealed $WO_3$ thin film sample deposited on Si wafer. The inset shows the simulated XRD pattern for orthorhombic $WO_3$.

The XRD pattern shows three well-resolved diffraction peaks which can be assigned to the (002), (020), and (200) reflections and all peaks can be indexed to the orthorhombic $WO_3$ (JCPDS No. 20-1324). This result was confirmed by additional XRD analysis of $WO_3$ thin films coated on quartz glass substrate with different thicknesses (Figure 3.6).
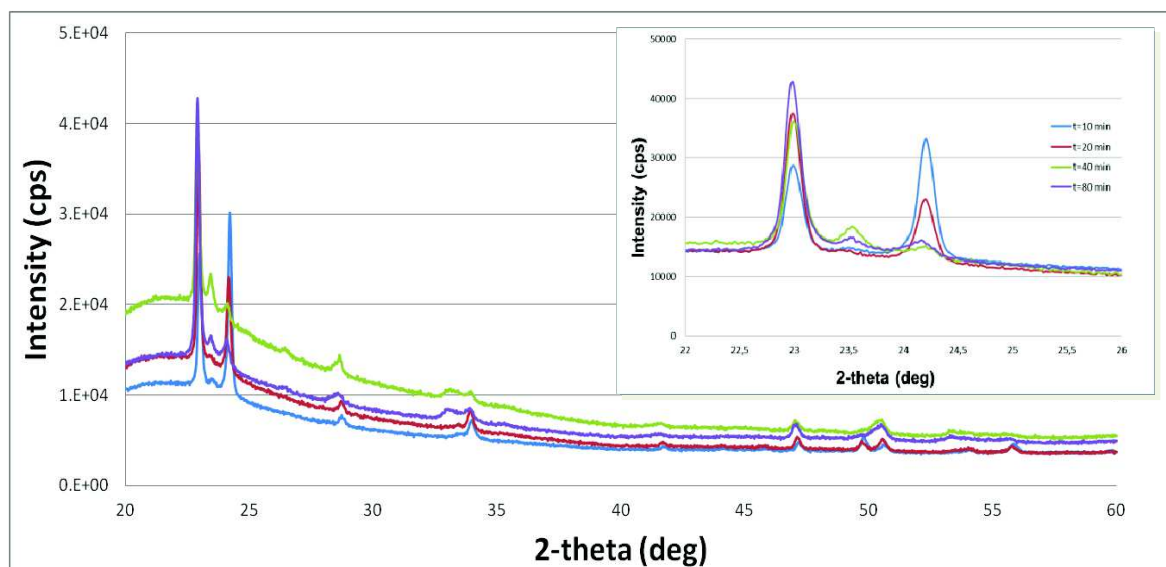
**Figure 3.6.** XRD spectra of annealed WO$_3$ films coated on quartz glass substrate with different thicknesses. The inset shows a magnification of the XRD pattern in the region of 2θ = 22−26°.

It is interesting to notice that although the position of characteristic peaks are consistent with the orthorhombic crystal structure, the relative intensities of XRD peaks - compared to the simulated spectra - are fairly different and change with the film thickness. This behavior may suggests a possible preferred orientation of tungsten oxide films. Texture analysis is a widely used tool for characterizing the orientation relationship between the film and substrate. More detailed studies on this issue are discussed in the next paragraph.

### 3.4.1. Spherical harmonics for texture analysis

Texture is an important feature for the characterization of films inasmuch as the properties of crystalline materials may depend on the individual properties of the single crystals as well as on parameters characterizing the polycrystalline state [42, 43]. X-ray diffraction is the most powerful tool for this analysis because the texture of the sample affects the integrated intensities of the reflections (hkl) [44]. Traditional methods of texture analysis produce coefficients indicating the degree of orientation of the polycrystalline material

based on the analysis of the diffraction peaks. However, the diffraction pattern can be used to calculate a crystallite orientation distribution function (ODF), which is the quantitative description of the preferred orientations of crystallites in a polycrystalline sample or film and can be represented by generalized spherical harmonics [45].

Basic parameters such as film thickness and the substrate on which films are deposited can strongly influence the texture. Indeed, a series of $WO_3$ samples were prepared on FTO and Si wafer supports with different thicknesses (see sample preparation). For each sample, XRD data were recorded with overnight scans and the patterns were indexed to the orthorhombic $WO_3$ structure; Figure 3.7 and 3.9 show the spectra between $2\theta$ = 22-26°, the range where the most intense $WO_3$ peaks result ((002), (020), (200) reflections).

The average crystallite size of $WO_3$ was determined by Scherrer's equation using the full width at half maximum (FWHM) of the three main X-ray diffraction lines [46] and the results are summarized in Figure 3.8 and 3.10. Interestingly the average grain size of the film is similar for all samples- annealed in same conditions (500 °C, 3h) – and is about 50-100 nm, independently from the film thickness or support morphology.
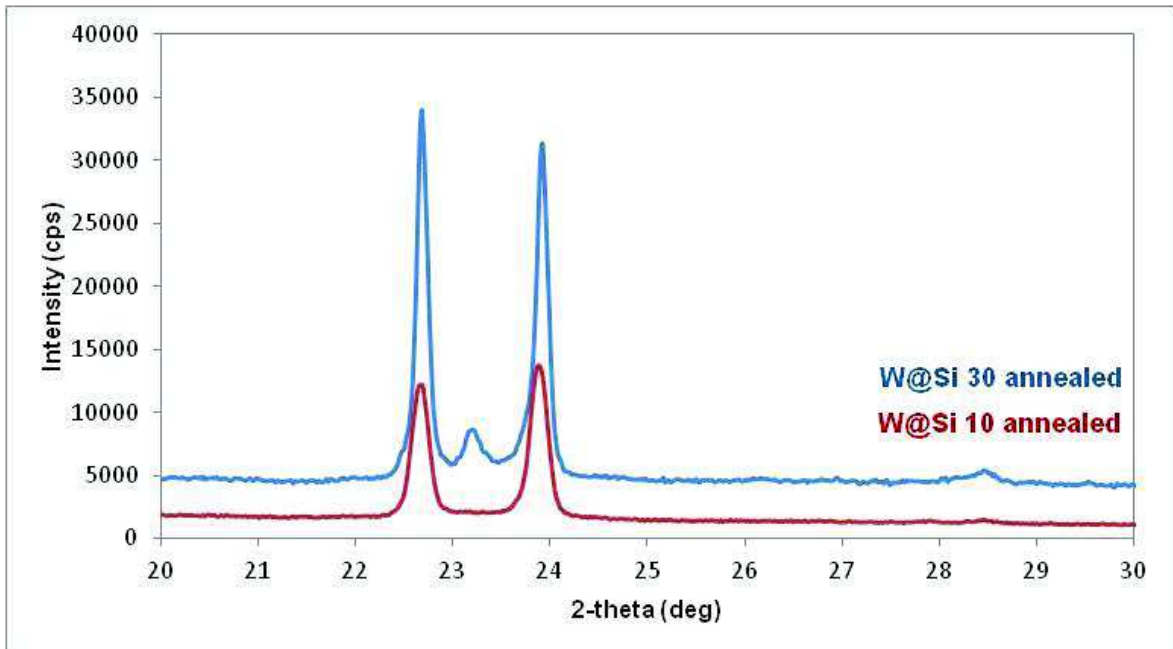


**Figure 3.7.** XRD spectra of annealed $WO_3$ films coated on Si wafer substrate with different thicknesses (red: 10 scan, blue: 30 scan).

**Average sizes and textures (spherical harmonics)**

| SCAN | Average size (nm) | X | Y | Z |
|------|-------------------|------|------|------|
| 10 | 103.7 | 1.51 | 0.67 | 1.58 |
| 30 | 70.88 | 1.03 | 0.39 | 0.89 |
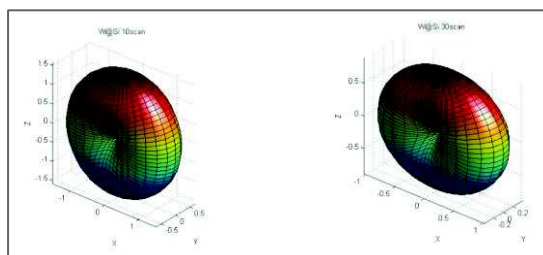


**Figure 3.8.** Summary of the calculated average crystallinite sizes and xyz coefficients (top) and spherical harmonics (bottom) of $WO_3$ films coated on Si wafer substrate.

On the contrary, marked differences in peak intensities were observed: ideally, the scattering intensity from each set of lattice planes should be equivalent for the crystalline powder $WO_3$ (Figure 3.5) however a significant decrease in relative intensity for the (020) reflection is evident and this suggest a preferred orientation of the film.
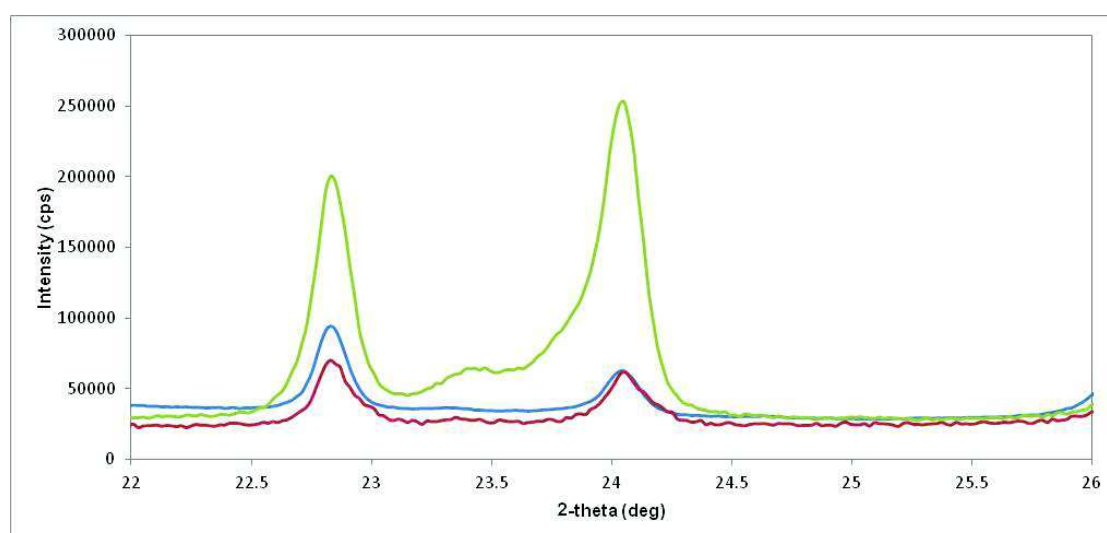


**Figure 3.9.** XRD spectra of annealed $WO_3$ films coated on FTO substrate with different thicknesses (blue: 4 scan, red 10 scan, green: 30 scan).

In order to better understand a possible relationship between the film texture and the substrate, quantitative analysis were performed by the spherical harmonics description of the preferred orientation of crystallites. The graphic representation and the xyz coefficients are shown in Figure 3.8 for the $WO_3$ film on Si wafer and in Figure 3.10 for the FTO substrate.

**Average sizes and textures (spherical harmonics)**

| SCAN | | Average size (nm) | X | Y | Z |
|---|---|---|---|---|---|
| | A | 66.20 | 0.785 | 1.12 | 1.68 |
| 4 | B | 69.44 | 0.99 | 0.68 | 1.72 |
| | C | 57.12 | 1.05 | 0.834 | 1.17 |
| | A | 82.83 | 1.83 | 0.74 | 1.54 |
| 10 | B | 75.31 | 1.57 | 0.637 | 1.51 |
| | C | 81.28 | 1.11 | 0.707 | 1.73 |
| | D | 82.81 | 1.32 | 0.766 | 1.93 |
| | A | 66.56 | 1.99 | 0.843 | 1.33 |
| 30 | D | 77.80 | 1.42 | 0.834 | 1.97 |
| | E | 87.97 | 1.48 | 0.736 | 1.70 |
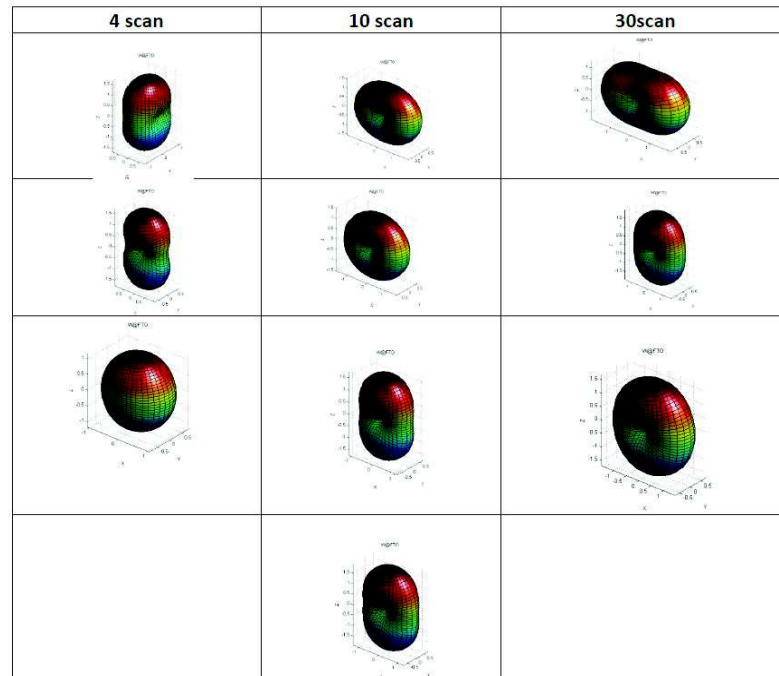


**Figure 3.10.** Summary of the calculated average crystallinite sizes and xyz coefficients (top) and spherical harmonics (bottom) of $WO_3$ films coated on FTO substrate.

It can be clearly seen that on unstructured Si wafer the preferred orientation of the film is along the x and z axes ((200) and (002) planes respectively) and do not change with the film thickness. Similarly, on the randomly oriented FTO substrates the growth rate in the y direction is less important than in (002) and (200) directions but the relative intensities of these latters do not follow any trend with the thickness and are not even consistent between repeated deposition experiments. This result suggests that the CVD deposited and post-annealed tungsten oxide film shows some preferred orientation of $WO_3$ films on different substrates, however, on structured surface the film growth follows the surface roughness.

## 3.5 SEM/EDX

Scanning electron microscopy (SEM) analysis was performed to provide micro and nanoscale information on morphology and thickness of the chemical vapor deposited tungsten oxide films on different substrates. Energy-dispersive X-ray spectroscopy (EDX or EDS) - in conjunction with electron microscopy - was used to provide information concerning the composition of near-surface regions of the material. Figure 3.11 and 3.12 show some typical cross sectional SEM images (45° and 90°) of the amorphous and crystalline $WO_3$ films on silicon wafer and microscope glass support. It is worth noting that the film thickness may widely range from about 20 nm (2 cycles) to 300-400 nm (20-30 cycles) depending on the number of deposition cycles or deposition time. Films appear dense and uniform.
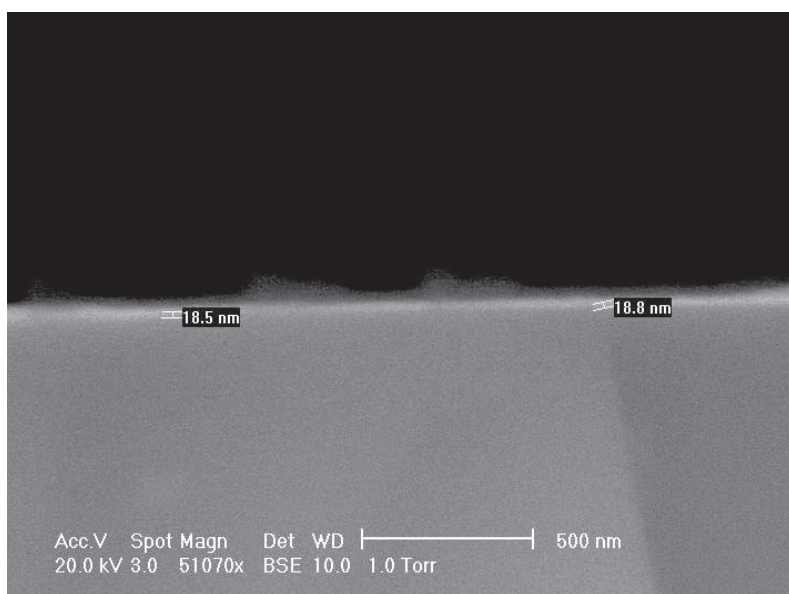


**Figure 3.11.** Cross-sectional SEM image (90°) for the amorphous $WO_3$ film on microscope glass (2 deposition cycle).
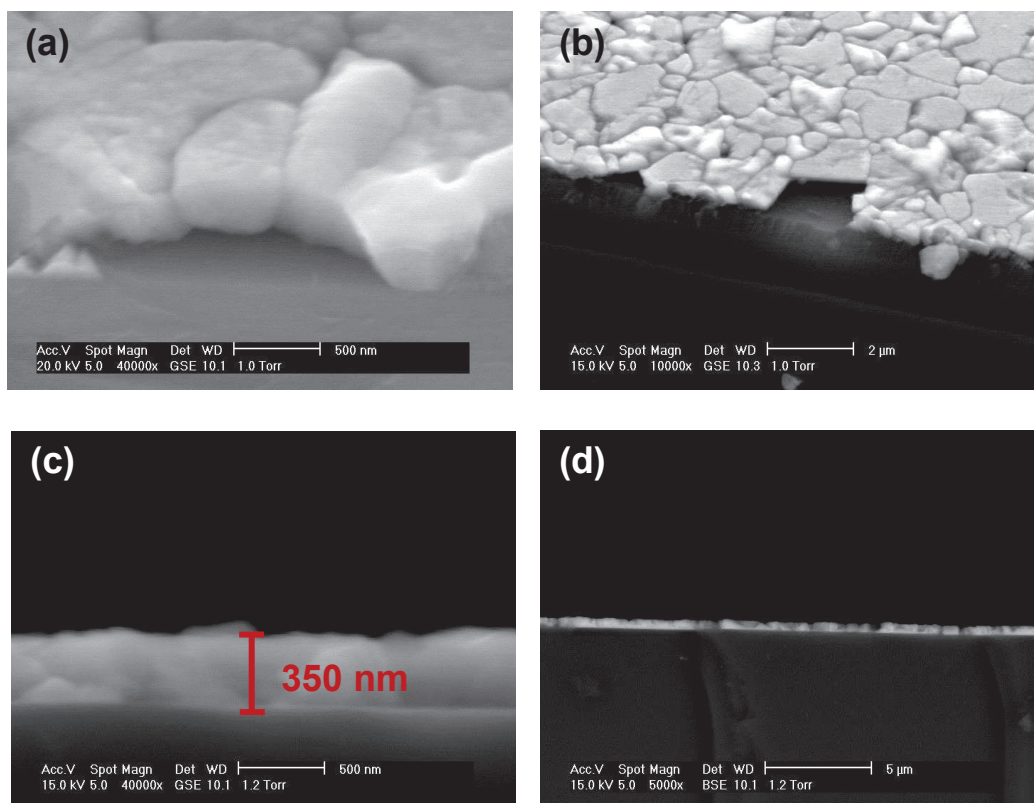
**Figure 3.12.** Cross-sectional SEM images of (a) and (b) crystalline WO₃ film on Si wafer (spot like deposition for 40 minutes, 45 °); (c) and (d) crystalline WO₃ film on Si wafer (spot like deposition for 40 minutes, 90 °).

WO₃ depositions on FTO supports were studied in order to comprehend the influence of substrate topography on the morphology of deposited films. It was observed that on structured surfaces - such as FTO conductive glass - the morphology of thin films is strongly dependent on the film thickness (i.e. the duration / n° of cycles of deposition). As shown in Figure 3.13 while the thinnest film exhibits a morphology closely related to that of the FTO substrate, thickest films consist of agglomerates few hundred nanometers scaled. Consistently with literature reports, this results confirms also the ability of chemical vapor deposition to grow uniform films on surfaces with complex topography. In any case, highest magnification images always suggest the presence of a least a polycrystalline phase.
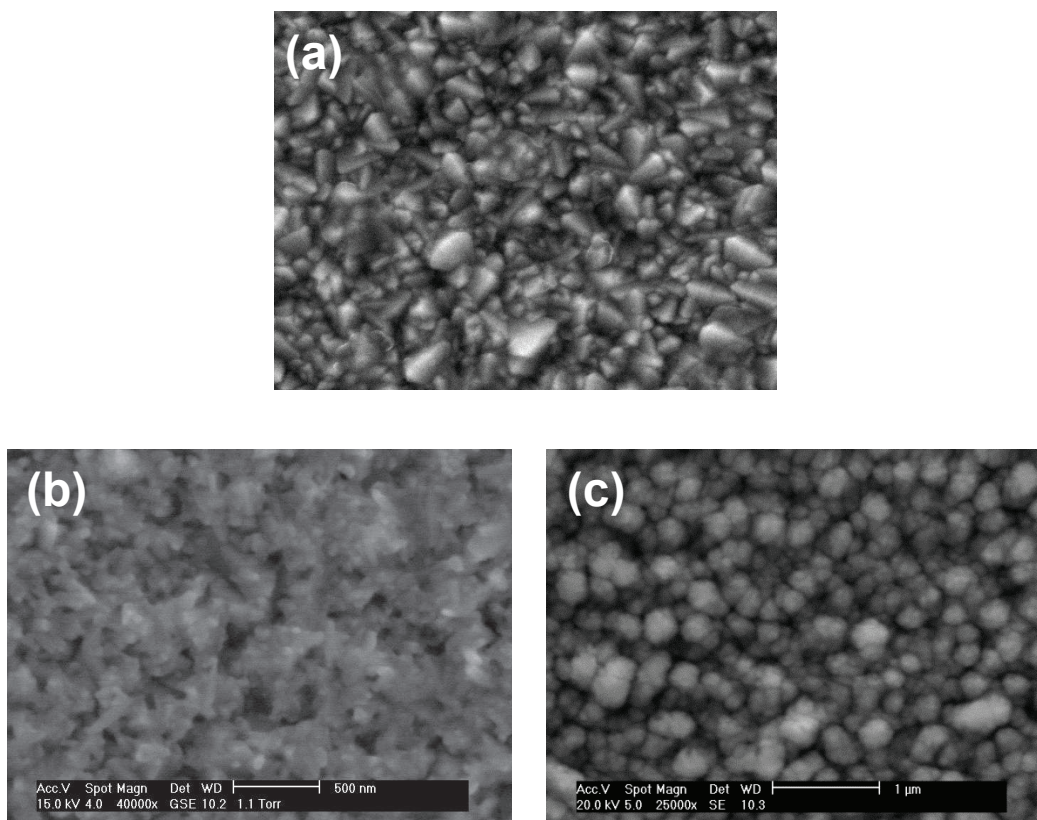
**Figure 3.13.** Top view SEM images of (a) pure-FTO glass, (b) thin film of $WO_3$ on FTO substrate, (b) thick film of $WO_3$ on FTO substrate.

To study the composition of the chemical vapor deposited films, EDX measurement were taken on the as-synthesized and annealed samples. Spot-like depositions on Si wafer substrates were performed in air as well as in inert (argon) atmosphere and semi-quantitative O/W atomic ratio were determined. Commercial crystalline $WO_3$ powder was analyzed a reference material. The detected atomic ratio varied between 2.1 and 5.1 for the reference material, whereas 3.5-6.0 for the analyzed $WO_3$ films. This result confirms that the film obtained by CVD was tungsten oxide in both experimental conditions. The overestimated value can be due to terminal oxygen atoms present on the surface of thin films.

Cross sectional SEM images and related EDX profile were acquired also on composite ITO/hematite/WO$_3$ films. Figure 3.14 shows the top view SEM image of this sample and the EDX spectrum. The amorphous WO$_3$ film has typical three-dimensional agglomerate structure, closely similar to those observed also for film depositions on FTO and Si wafer substrates. The EDX spectrum confirms the presence of different layers, as revealed by the characteristic peaks of Si (glass support), In (ITO), Fe (hematite) and W (WO$_3$).

The cross sectional SEM image and EDX maps evidence the multilayer structure of the composite film (Figure 3.15).
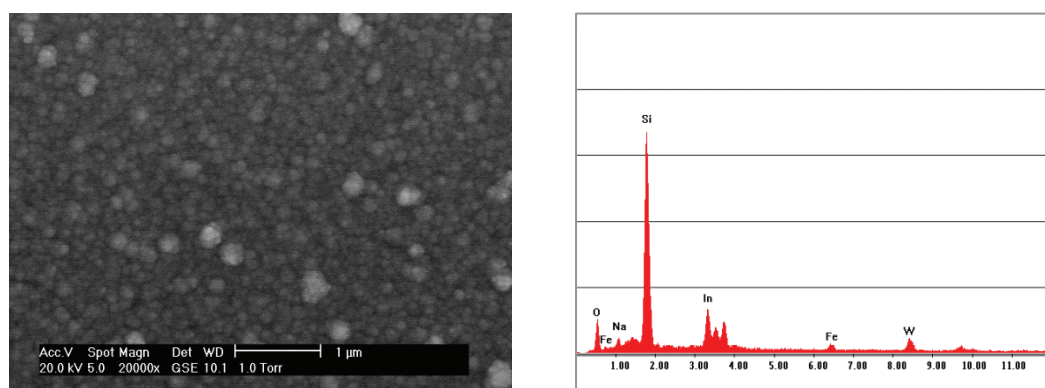


**Figure 3.14.** Top view SEM image of CVD tungsten oxide film on ITO/hematite support (left) and the relative EDX spectrum (right).
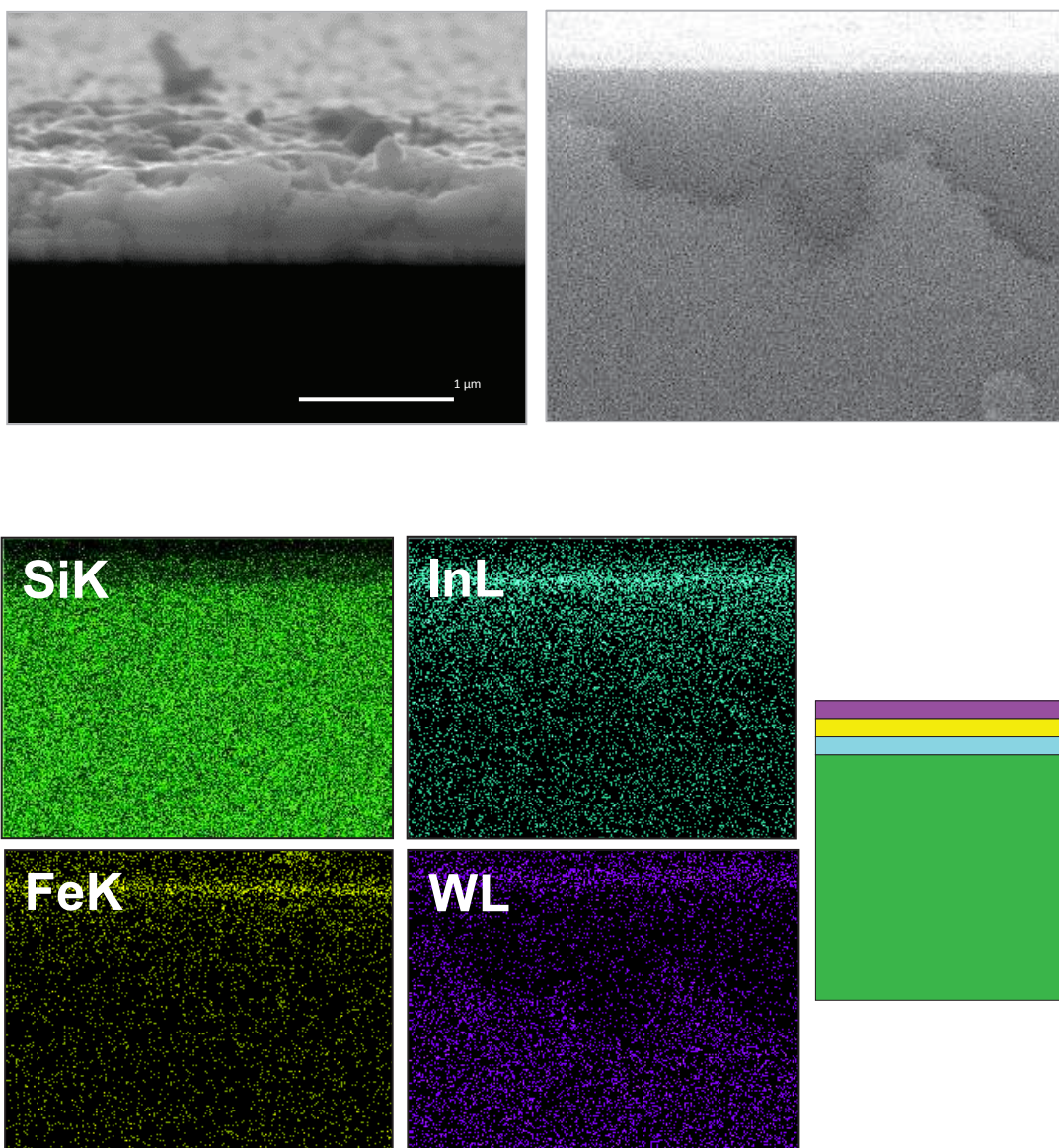
**Figure 3.15.** Cross sectional SEM images of CVD tungsten oxide film on ITO/hematite support (top), the relative EDX maps (bottom, left) and a schematic depiction of the multilayer structure (bottom, right).

# 4. Photocurrent measurements

## 4.1 Introduction

Photocurrent experiments were conducted in order to explore the ability of tungsten oxide and hematite/tungsten oxide composite semiconductor films to undergo photoelectrochemical water splitting processes.

Materials for electrodes often require a high level of optimization in terms of composition and morphology. In particular in photoelectrochemistry the thickness and composition of semiconductor films is important, and so the main aims of this chapter are to (i) investigate the effect of $WO_3$ film thickness on the photoelectrochemical performance and to (ii) demonstrate the improvement of voltammetric current responses of nanostructured hematite /$WO_3$ multilayer semiconductor with respect to the pure hematite electrode.

## 4.2 Experimental

### 4.2.1 Photoelectrode preparation

1. FTO/$WO_3$

Sample preparation is described in paragraph 3.2.

In brief, tungsten oxide films are deposited onto fluorine-doped tin oxide (FTO) subtrates. Varying the number of deposition cycles (scans) it is possible to produce films with different thickness and to systematically study the photoactivity of $WO_3$ as a function of thickness. A small part of the FTO support was covered by microscope cover slide in order to retain a conducting contact.

2. $ITO/Fe_2O_3/WO_3$

Substrates ($ITO/Fe_2O_3$) were provided from Chalmers University (Sweden): iron-oxide films of 25 and 110 nm were deposited on ITO coated glass pieces (15mm x 15 mm, ≤15 Ω/sq, PGO GmbH) by electron-beam evaporation and subsequently oxidized in a tube furnace at 350 1C in a mixed $N_2/O_2$ atmosphere [47].

Deposition of the tungsten oxide film was performed using $W(CO)_6$ as precursor and argon as carrier gas. The deposition was carried out in air and the inlet and outlet flow were set to 0.8 ml/min and 3.5 ml/min respectively. The distance between the probe and the support was set to 0.3 mm. Deposition experiments were conducted at 250 °C support temperature and the probe was heated to 75 °C. A rectangular part of the ITO support was covered by microscope cover slide in order to retain a conducting contact The substrate was moved by the computer-driven stepping motors according to the best experimental conditions described in paragraph 2 ($\Delta x$ and $\Delta y$ = 3 mm, v = 6 mm/min, 4 cycle of deposition). At the end of the deposition the argon line was closed and the targets were allowed to cool down to 100 °C. The samples were tested prior to thermal treatment because ITO is not stable above 400 °C [48]. Thickness was estimated to be 20 nm by cross-sectional SEM measurement on model samples synthesized in the same conditions (no direct measurements were performed). A picture of a sample is shown in Figure 4.1.
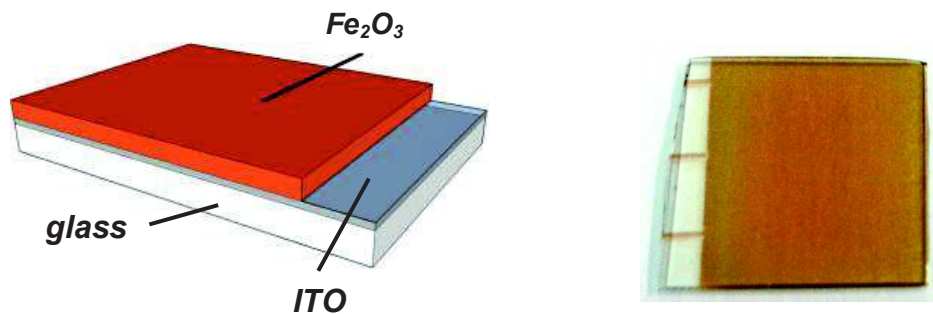


**Figure 4.1.** Schematic illustrations of the glass/ITO substrate (left), and picture of the $WO_3$ deposition (right).

3.  $FTO/Fe_2O_3/WO_3$

$FTO/Fe_2O_3$ support was prepared at CNR-ISTM, Milan, Italy. Briefly, the $\alpha$-$Fe_2O_3$ photoanodes were grown on conductive FTO coated glass slides (Aldrich) of 13 × 13 mm. The substrates were cleaned by sonication in deionized Milli-Q-Water, ethanol and acetone (10 min for each step). The $\alpha$-$Fe_2O_3$ platelets were synthesized by using PE-CVD (for more details see [49]).

Deposition of the tung3sten oxide film was performed similarly to that previously described for the $ITO/Fe_2O_3/WO_3$ samples. After deposition, thermal treatment was performed in a laboratory furnace (in air) at 500 °C for 3 h in order to obtain crystalline $WO_3$ film.


## 4.2.2 Photoelectrochemical measurements

Photocurrent measurements of $ITO/Fe_2O_3/WO_3$ samples were performed at the Chalmers University of Technology, Goteborg, Sweden, in a standard three-electrode configuration: fabricated samples as working electrode, a Pt wire as counter electrode, and Ag/AgCl electrode as reference electrode. A 0.5 M $K_2SO_4$ solution (pH=6.9) was used as electrolyte. The sample was illuminated from the front side in all the experiments. A solar simulator (SKU SS150, Sciencetech. Inc.) was used as a light source for photocurrent-potential measurements.


Photocurrent measurements of $FTO/WO_3$ and $FTO/Fe_2O_3/WO_3$ samples were performed at CNR-ISTM, Milan, Italy, to estimate the solar photocurrent of the photoanodes in a three-electrode configuration with 0.5 M $Na_2SO_4$ as electrolyte using Pt coil as counter electrode and saturated calomel reference electrode (SCE) as reference electrode. The cyclic voltammetry and chronoamperometric measurements were carried out using a potentiostat (AUTOLAB model PGSTAT101) and the samples were illuminated with simulated sunlight from a 300 W xenon lamp having a power of 1 sun (1000 $W/m^2$).

The cyclic voltammetry measurements were performed at a scan rate of 10 mV/s and the scanned voltage was between −0.2 and +1.1 V, the chronoamperometric curves were recorded at 1.23 V for 120 s.
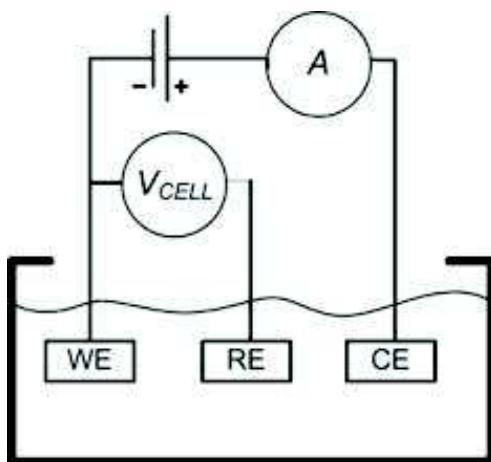
**Figure 4.2.** Scheme of a three electrode cell (CE = counter electrode, WE = working electrode and RE = reference electrode) (left) and the picture of the instrumentation setup (potentiostat and xenon lamp) used in the electrochemical experiments (right).



**Figure 4.3.** A picture of the working electrode.

## 4.3 Results and discussion

### 4.3.1 FTO/WO$_3$ samples with different WO$_3$ thickness

Cyclic voltammetry offers a simple but powerful tool to explore reactivity of semiconductor materials as a function of the applied potential. WO$_3$ is a semiconductor material with n-

type characteristics [50] and thin, crystalline $WO_3$ films have been demonstrated to be oxygen evolving photoanode where the locally generated holes cause oxidation of water [51]. Nonetheless, research on nanostructured tungsten trioxide is relatively new and the morphology and thickness varies from author to author. Therefore, it is important to investigate the influence of our tungsten oxide film thickness on photoelectrochemical behavior in order to find the best performing material for composite electrode preparation.

Typical voltammetric responses and chronoamperometric curves for CVD-$WO_3$ films on FTO are shown in Figure 4.4.
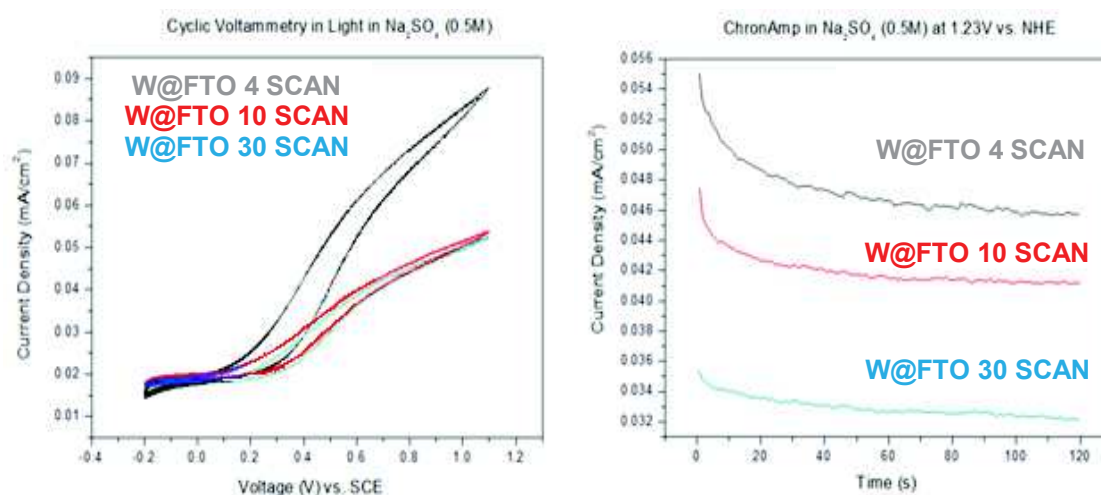


**Figure 4.4.** Illuminated cyclic voltammograms (left) and chronoamperometric curves (right) of $WO_3$ electrodes of different thickness (fixed potential : 1.23 V).

It can be observed that photocurrent density increased with decreasing thickness of crystalline $WO_3$ film. This effect can be attributed to the competing mechanisms of photogeneration and recombination of electron-hole pairs: since thicker films may have unstable growth, this suggest a significant enhancement of the defects enhancing the recombination process [52]. According to this result, in latter experiments composite (hematite/$WO_3$) photoanodes were prepared depositing thin (4 scan) $WO_3$ layers on nanostructured hematite supports.

## 4.3.2 ITO/ $Fe_2O_3$/$WO_3$ samples

Both samples with 110 nm and 25 nm $Fe_2O_3$ thin below the tungsten oxide show similar response in dark and under illumination (Figure 4.5), i.e. not a high photoresponse, unless for very highly anodic potentials (higher than 2 V vs. RHE). It is well known from literature that amorphous films are basically unable to develop a regular depletion region which is effective at separating charge carriers; this clearly suggests that the amorphous, as-synthesized $WO_3$ film alone does not show photoelectrochemical response. Not surprisingly, the composite material did not provide positive results at the same extent.
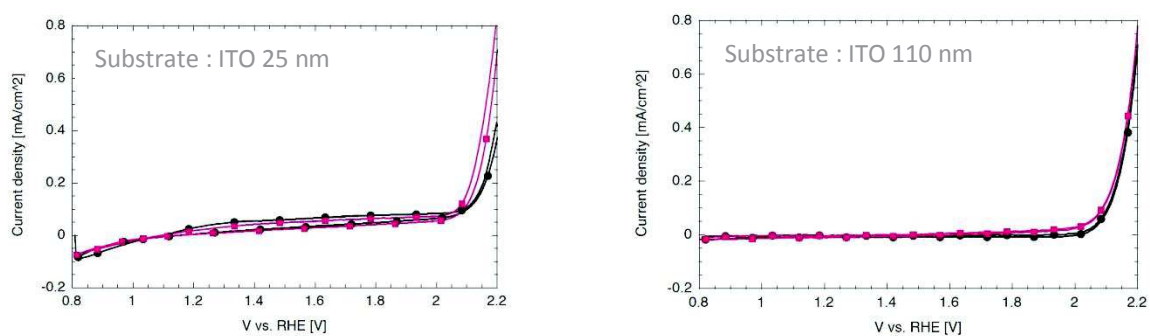


**Figure 4.5.** Dark (black line) and illuminated (red line) current-voltage curves of ITO/$Fe_2O_3$/ $WO_3$ samples (left: 20 nm ITO layer; right: 110 nm ITO layer).

## 4.3.2 FTO/ $Fe_2O_3$/$WO_3$ samples

The different features of the cyclic voltammetry curves of the $WO_3$ and $Fe_2O_3$/$WO_3$ samples (Figure 4.6) suggest two important points. The presence of crystalline $WO_3$ shifts the onset potential of the photocurrent by ~0.4 V to the cathodic (negative) direction and also the photocurrent density was increased. The cronoamperometric measurement clearly shows that we obtained a significant increment of the current density from 30 a 52.5 µA/cm$^2$ which in terms of enhancement implies a +75% of increase. It is worthy to note also that both photoelectrodes are stable in the electrolyte solution since the photocurrents are constant in time (120 s).
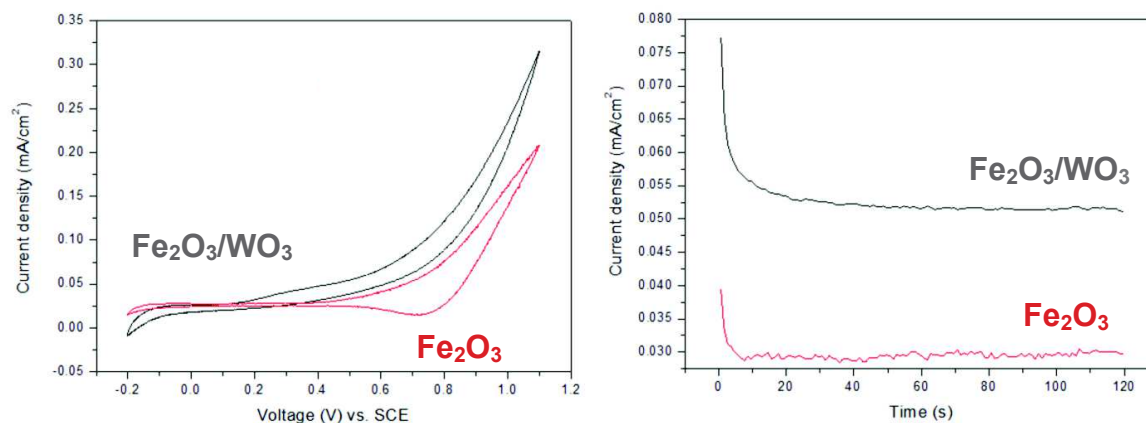
**Figure 4.6.** Illuminated cyclic voltammograms (left) and chronoamperometric curves (right) of $Fe_2O_3$ (red) and $Fe_2O_3/WO_3$ (black) electrodes (fixed potential : 1.23 V).

Given that the limit for the theoretical current density for (AM 1.5) photoelectrochemical oxygen evolution at pure nanostructured $Fe_2O_3$ has been reported as 12 mA/cm$^2$ [53] and the reproducible literature values are currently at ca. 3 mA/cm$^2$ [54], our results seem to be little relevant in terms of current density. Nonetheless, these findings highlight that for photoelectrochemical applications composite materials can be more efficient than single compounds under the same experimental conditions. Further investigations for improving the experimental setup (pH, electrolyte solution, nanostructure type and shape, film thickness…etc.) are necessary.

# 5. Conclusions

Metal organic chemical vapor deposition technique has been applied for the fabrication of thin photoelectrochemically active $WO_3$ films on FTO and FTO/hematite substrates. Firstly, a new CVD reactor device was developed for high resolution and steering CVD deposition of tungsten oxide on different substrates. Experimental parameters have been improved for achieving uniform-thickness deposition on flat surfaces as well as on samples with complex morphology. It is worth noting that the film thickness may widely range from about 20 nm to 300-400 nm depending on the number of deposition cycles or deposition time. Secondly, structural, optical and morphological properties of composite films were characterized using XRD, UV-Vis and SEM/EDX techniques. As-deposited samples revealed an amorphous tungsten oxide structure in both air and argon atmosphere. After thermal treatment at 500°C, the amorphous phase turned into polycrystalline with orthorhombic crystal structure.

Finally, photoelectrochemical properties of $WO_3$ films on FTO, ITO/hematite, and FTO/hematite supports were studied. It was observed that only crystalline $WO_3$ films have a positive effect in terms of photocurrent. Considering that high temperature treatments are necessary to transform amorphous into crystalline $WO_3$, the utilization of the ITO substrate is completely ruled out. For FTO substrates, it was observed that differences of $WO_3$ thickness significantly affected the morphology of films as well as the photoelectrochemical behavior as the thinner the film, the higher resulted the current density. Based on this result, thin $WO_3$ films on FTO/hematite support were deposited in order to investigate new composite photoelectrodes for water splitting. The result obtained for this system clearly shows that tungsten oxide has a positive effect on the photocurrent properties of hematite. This evidence may be probably attributed to the decrease of surface recombination processes on hematite, due to the presence of thin $WO_3$ coating.

# 6. References

1       Chouhan N. and Liu Ru-Shi. Electrochemical Technologies for Energy Storage and Conversion, 2011, 1, ISBN: 978-3-527-32869-7

2       Bodansky D. The History of the Global Climate Change Regime, 2001

3       Grimes C.A., Varghese O.K., Ranjan S. Light, Water, Hydrogen: The Solar Generation of Hydrogen by Water Photoelectrolysis, Springer Science Business Media, LLC, New York, 1988.

4       Ameri T., Li N., Brabec C.J. Energy Environ. Sci. 2013, 6, 2390

5       Fahrenbruch A.L., Bube R.H. Fundamentals of Solar Cells: Photovoltaic Solar Energy Conversion, Academic Press Inc, San Diego,USA, 1983.

6       Garrett C.G.B., Brattain, W.H. Physical Review 1954 95 (4), 1092

7       Garrett C.G.B., Brattain, W.H. Physical Review 1955 99 (2), 376

8       Gerischer H.Z. Physik. Chem. NF. 1960, 26, 223; 1960, 60, 335; 1961, 325, 27, 48.

9       Nozik A.J. Ann. Rev. Phys. Chem. 1978, 29, 189-222

10      Fujishima A., Honda K. Nature 1972, 238, 37

11      Chen X., Shen S., Guo L., Mao S.S. Chem. Rev. 2010, 110, 6503–6570

12      Biernat K., Malinowski A., Gnat M. Chapter 5 In: Fang Z. ed. Biofuels - Economy, Environment and Sustainability. 2013 - intechopen.com ISBN 978-953-51-0950-1

13      http://wqjin-group.com/

14      Linsebigler A.L., Lu G., Yates J.T. Chem. Rev. 1995, 95, 735.

15      Kaneko M., Okura I. Photocatalysis: Science and technology; Springer-Verlag: New York, 2002.

16      Chen H.M., Chen C.K., Liu Ru-Shi, Zhang L., Zhang J., Wilkinson D.P. Chem. Soc. Rev. 2012, 41, 5654–5671

17      Kudo A. and Miseki Y. Chem. Soc. Rev. 2009, 38, 253–278.

18      Walter M.G., Warren E.L., McKone J.R., Boettcher S.W., Mi Q., Santori E.A., Lewis N.S. Chem. Rev. 2010, 110, 6446

19      Aroutiounian V.M., Arakelyan V.M., Shahnazaryan G.E. Solar Energy. 2005, 78 (5), 581

20      Alexander B.D., Kulesza P.J., Rutkowska I., Solarska R. Augustynski J. J. Mater. Chem. 2008, 18, 2298.

21      Klahr B.M., Hamann T.W. J. Phys. Chem. C. 2011, 115, 8393.

22    Sivula K., Le Formal F., Gratzel M. ChemSusChem 2011, 4, 432

23    Kay A., Cesar I., Gratzel M. J. Am. Chem. Soc. 2006, 128, 15714

24    Hisatomi T., Le Formal F., Cornuz M., Brillet J., Te´ treault N., Sivula K. Grätzel M. Energy Environ. Sci. 2011, 4, 2512-2515

25    Tilley S.D., Cornuz M., Sivula K. Grätzel M. Angew. Chem., Int. Ed., 2010, 122, 6549-6552.

26    Zhong D.K. and Gamelin D.R. J. Am. Chem. Soc., 2010, 132, 4202-4207.

27    Deb S.K. Solar Energy Materials and Solar Cells. 2008, 92(2), 245

28    Hisatomi T, Kubota J., Domen K. Chem. Soc. Rev., 2014, 43, 7520-7535

29    Wheeler D.A., Wang G., Ling Y., Li Y., Zhang J.Z. Energy Environ. Sci. 2012, 5, 6682.

30    Osterloh F.E. Chem. Mater. 2008, 20, 35.

31    Rajeshwar K., de Tacconi N.R., Chenthamarakshan C.R. Chem. Mater. 2001, 13, 2765-2782.

32    Sequeda F.O. Thin Film Deposition Techniques in Microelectronics. 1986, 38(2), 55.

33    The Chemistry of Metal CVD. Eds: Kodas T., Hampden-Smith M. VCH, Weinheim, 1994.

34    Marelli M., Ostinelli L., Dal Santo V., Milani P., Psaro R., Recchia S. Catalysis Today 2009,14, S170-S175.

35    Jones A.C. Chem. Soc. Rev. 1997, 26, 101.

36    Ivanova A.R., Nuesca G., Chen X., Goldberg C., Kaloyeros A.E., Arkles B., Sullivan J.J. J. Electrochem. Soc.1999, 146 (6), 2139.

37    Spear K.E., Dirkx R.R. Pure & Appl. Chem. 1990, 62, 89.

38    Vemuri R.S., Kamala Bharathi K., Gullapalli S.K., Ramana C.V. ACS Applied Materials and Interfaces. 2010, 2(9), 2623.

39    Abdullaha S.F., Radiman S., Abdul Hamid M.A., Ibrahim N.B. Jurnal Fizik Malaysia 2007, 28(1 & 2), 7.

40    Granqvist C.G. Handbook of Inorganic Electrochromic Materials. Elsevier, Netherlands, 1995.

41    Armelao L., Bertoncello R., Granozzi G., Depaoli G., Tondello E., Battaglin G. J Mater. Chem. 1994, 4(3), 407.

42    Sitepu H., Prask H. J., Vaudin M.D. JCPDS-International Centre for Diffraction Data 2001, Advances in X-ray Analysis, 44, 241.

43    Wang Y. N., Huang J. C Materials Chemistry and Physics 2003, 81, 11.

44    Lutterotti L., Gialanella S. Acta Mater. 1998, 46(1), 101.

45    Schaeben H., Van den Boogaart K. G. Tectonophysics 2003, 370 ,253.

46    Cullity, B. D. Elements of X-Ray Diffraction; Addison-Wesley:

      Reading, MA, 1967.

47    Iandolo B., Zach M. Aust. J. Chem. 2012, 65, 633.

48    Maoshui Lv, Xianwu Xiu , Zhiyong Pang, Ying Dai, Lina Ye , Chuanfu Cheng, Shenghao Han. Thin Solid Films. 2008, 516(8),2017.

49    Marelli M., Naldoni A., Minguzzi A., Allieta M., Virgili T., Scavia G., Recchia S., Psaro R., Dal Santo V. ACS Appl. Mater. Interfaces. 2014, 6, 11997.

50    Sivakumar R., Raj A.M.E., Subramanian B., Jayachandran M., Trivedi D.C., Sanjeeviraja C. Materials Research Bulletin. 2004, 39, 1479.

51    Enesca A., Duta A., Schoonman J. Thin Solid Films. 2007, 515, 6371.

52    Kwong W.L., Qiu H., Nakaruk A., Koshy P., Sorrell C.C. Energy Procedia. 2013, 34, 617.

53    Brillet, J.; Grätzel, M.; Sivula, K., Nano Letters. 2010, 10(10), 4155.

54    Tilley S.D., Cornuz M., Sivula K., Grätzel M. Angewandte Chemie International Edition. 2010, 49, 6405.

# Chapter 4

(*article*)

## Anodic Stripping Tin Titration: A Method for the Voltammetric Determination of Platinum at Trace Levels